Validation of efficient numerical models for out-of-plane bending of unreinforced masonry walls

J. van Dam

Master of Science Thesis

Delft University of Technology

Validation of efficient numerical models for out-of-plane bending of unreinforced masonry walls

MASTER OF SCIENCE THESIS

For the degree of Master of Science in Structural Engineering at Delft University of Technology

J. van Dam

June 3, 2015

Faculty of Civil Engineering and Geosciences (CEG) · Delft University of Technology

Preface

In the Netherlands gas exploration of the NAM induces earthquakes which causes damaged to buildings in Groningen. This master's thesis is about the numerical calculation of the resistance of unreinforced masonry walls loaded in out-of-plane bending.

This report consists of the following parts:

1. Thesis report This part discusses the main research goal, analysis methods, results, conclusions and recommendations. It is written in a scientific paper format to keep the report concise and improve readability.

2. Literature review The second part consists of background information about earthquakes, masonry behaviour, experimental research, time-integration methods and methods for structural analysis of URM walls. For these methods a comparison is made and the two most suitable methods for out-of-plane bending are used for modelling the URM walls.

3. Modelling report The last part discusses the models used for calculation of capacity of URM walls. It gives a detailed overview of used geometry, elements, material models, loads, convergence criteria and results and draws conclusions from this. Also some extra background information is provided wherever side steps are taken to investigate some phenomenon.

All parts have there own page numbers and tables of contents.

JOS VAN DAM

THESIS REPORT

DELFT UNIVERSITY OF TECHNOLOGY

Revisions

Rev.	date	status	remark
0	11-4-2015	concept	Presented at fourth committee meeting
1	12-5-2015	concept	Rewritten after fourth committee meeting
2	19-5-2015	for review	Adjusted after comments from Max Hendriks
3	2-6-2015	final	Adjusted after comments from green light: meeting - *Summary:* Less strict statements, rewritten NPR part - *Sec. 1 Introduction:* More focus on the numerical models, better specification of the research goal. - *Sec. 5 Validation of FE models:* Added information on sensitivity of amplitude and governing frequency on stiffness reduction for dynamic analysis and influence of thickness and Youngs Modulus on stiffness reduction for static analysis as explained during green light meeting. - *Sec. 6 Comparison with analytical calculation NPR 9998:* expanded explanation of method Wijte, included comparison NEN-EN 1996-1-1 static cross-section verification, added sensitivty analysis to overburden load of FE models, checked load-displacement behaviour with numerical model, added comparison of boundary conditions. - *Sec. 7 Conclusion:* rewritten to reflect more on the research goals. Statements are generally less strict. - *Sec. 8 Recommendations:* Rewritten the recommendations into a running paragraph to add context and given further explanation on why further research is important. - Added list of symbols, nomenclature and acronyms - Grammatical corrections

STRUCTURAL MECHANICS, DELFT UNIVERSITY OF TECHNOLOGY

Submitted on 5th June 2015. Revision 3

Validation of efficient numerical models for out-of-plane bending of unreinforced masonry walls

Written by: Jos van Dam, *MSc Student, Delft University of Technology, Faculty of Civil Engineering, Department of Structural Mechanics*

Summary: This study investigates four numerical models to approximate the static and dynamic resistance of an Unreinforced Masonry (URM) wall loaded in one-way out-of-plane bending. From validation with experimental data it was found that for the combination of shell and interface elements with discrete cracking the static and dynamic behaviour of URM walls for out-of-plane bending is dependent on the interface stiffness. Due to Euler-Bernouilli's hypothesis, on which these elements are based, the deformation over the thickness remains straight, while in reality the wall deforms non-linearly over the thickness. A reduction of the interface stiffness is proposed to mimic crack opening with a linear deformation and obtain realistic results. The validated model is used for comparison with the analytical calculation of NPR 9998. This shows that the boundary condition assumptions can be made differently to increase the resistance of out-of-plane walls.

Keywords: Out-of-plane bending, unreinforced masonry, numerical validation, shell elements, earthquake loading, one-way bending, micro-modelling, interface stiffness

Graduation Committee:
Prof. dr. ir. J.G. Rots
Dr. ir. M.A.N. Hendriks
Dr. V. Mariani
Dr. ir. K.C Terwel
Ir. L.J.M. Houben

Table of Contents

1 *Introduction*

Induced earthquakes, caused by gas extraction by the Nederlandse Aardolie Maatschappij (NAM), damages the typical masonry buildings in Groningen. The goal of this study is to validate different Finite Element (FE) models that are able to find the capacity of URM structures loaded in out-of-plane bending in an efficient and accurate way. The models are accurate if the test results do not show significant with Doherty [2000] and if deformations and failure modes are similar to the experimentally found ones. The efficiency of the models is validated by comparing the computing costs of the models, generally more nodes means more computing time.

One-way bending of unreinforced masonry walls has experimentally been studied by Doherty [2000]. Both quasi-static and dynamic tests have been performed for different width/height ratio's with different amounts of overburden. The FE models developed in this study were validated against the results of this experiment.

The validation of different FE methods for determination of the capacity of unreinforced masonry structures in out-of-plane bending is part of a broader research program carried out by ARUP, EUCentre and TU Delft. One of the objectives of this program is to increase the accuracy of numerical analysis by using cross-validation, based on six different experimental studies, between the FE implementations used by the institutes. TU Delft uses the FE package DIANA.

This study tries to validate four different numerical models. These are selected from a literature survey, since they use a micro-modelling approach. The accuracy and efficiency of these models is investigated. A summary of the literature survey is presented in Sec. 2. For the full literature review the reader is referred to Literature Review [2015].

The first numerical model uses plane strain elements placed orthogonal to the plane of the wall. These elements are used to represent three dimensional brick elements. Since in this study only out-of-plane bending is investigated, the wall's longitudinal dimension is of no interest and thus this simplification is made. A smeared cracking material model is used to model the cracks in the wall.

The second model also uses plane strain element but with line interface elements at mid-height. Instead of a smeared cracking approach discrete cracking is used in these interface elements.

The third model consists of curved shell elements placed in the longitudinal direction of the wall. These elements reduce the wall's thickness to one node and are therefore more efficient to use in full structures than three dimensional brick elements. A smeared crack material model is applied to these elements as well.

The last model is similar to the third except for a line interface at mid-height with discrete cracking. The shell elements behave elastic in this model.

These models are subjected to static and dynamic loads and are compared to the experimental results of Doherty for validation. For full details on these and other less complex models the reader is referred to the Modelling Report [2015].

To show an application of the validated FE model it is compared with the NPR 9998, which is the first guideline for NEN-EN 1998-1 specific for the Netherlands. This guideline proposes two methods to find the out-of-plane resistance of URM buildings loaded by earthquakes. The first method uses time history analysis, the second an equivalent static load with verification according to NEN-EN 1996-1-1, for which an example calculation is provided. This calculation is step by step compared with the validated FE model.

2 *Literature Survey*

From literature six methods where compared to model the behaviour of URM masonry in out-of-plane bending, see Fig. 2.1 for an overview of all methods.

The Yield-Line Theory approximates the capacity of the wall by using the cracking moment analogous to the plastic yield moment for determination of the capacity of a steel plate, see Fig. 2.2. Although Brinker [1984] states that tensile and compressive strength do not influence the capacity, this is highly questionable since the cracking moment increases for greater strength properties. Doherty [2000] states that the wall can have more resistance after cracking. He defines this as the semi-rigid threshold. Lourenço [2000] states that a yield-line analysis is not suited for masonry structures since a typical yield-line pattern can only be observed at the ultimate failure, while at peak load a distributed crack pattern is visible.

Shibata and Sozen [1976] originally proposed the Linearized Displacement Based Analysis (LDBA), which uses a substitute single degree of freedom model to approximate the structure as a whole, see Fig 2.3. Doherty et al. [2002] proposed a simplified method to find the parameters of an appropriate substitute-structure from a tri-linear load-displacement diagram. According to Doherty the difference of the LDBA compared with a time history analysis is in the order of 50%, however it out-performs a force based quasi-static analysis especially for high frequencies.

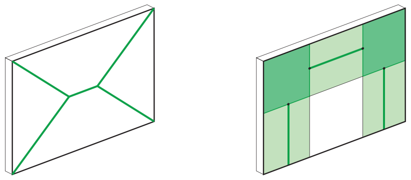

Yield Line Theory Equivalent Frame Method

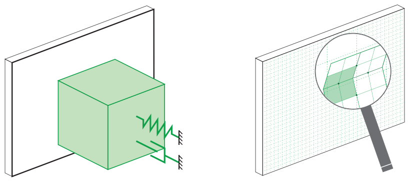

Linearised Displacement Based Analysis Rigid Elements Method

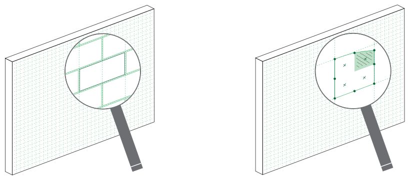

Multisurface Interface Model Anisotropic Continuum Model

Figure 2.1: Schematic representation of methods for modelling URM structures found in literature

Roca et al. [2005] give a detailed explanation of the Equivalent Frame Method, which uses beam elements to simplify walls, piers and spandrels of URM structures, see Fig. 2.4. In principle this method can model out-of-plane deformations, but as explained by Lagomarsino et al. [2013] in the TREMURI FE implementation this degree of freedom has been removed.

Casolo [2000] has developed a model suitable for dynamic analysis specifically for walls which are governed by out-of-plane behaviour. Rigid quadrilateral elements are used to model a wall. These elements are connected by rotational springs at the mid-side nodes of the quadrilateral elements (Fig. 2.5). These springs are subjected to bending and twisting between the two elements. The elastic and plastic behaviour are defined by a non-linear moment-curvature relation.

The Multisurface Interface Model proposed by Lourenco and Rots [1997] gives a micromodelling approach to the URM problem. Brick elements or quadrilateral elements are modelled elastically and are seperated by line interface elements in which all the material properties are lumped, see Fig. 2.6. The model is able to capture all failure modes and is therefore more realistic. The number of interfaces and elements require more degrees of freedom than the other methods. This drastically increases the computation costs especially when an implicit time-integration method is used, since this requires the solution of the system as a whole. This reduces the scalability of this method.

The Anisotropic Continuum Model proposed by Lourenço [2000] uses two dimensional plane elements and a smeared crack approach. This means that a crack in the wall is smeared over an element as a plastic deformation, see Fig. 2.7. Since local deformation due to cracks are not modelled, the results are only of interest when the structure as a whole is observed. The advantage of this method is the reduction of degrees of freedom. Furthermore there is no need to predefine nodes when the wall cracks. This method is of particular interest if a large structure is observed or if the cracks are widely spread over the structure.

The last two methods are of interest for the goal of this study, of which the continuum model is the most interesting. There is no record in literature about the validation of these methods with the use of shell elements for out-of-plane bending statically or dynamically. Therefore this study will verify these methods using the experiments of Doherty [2000].

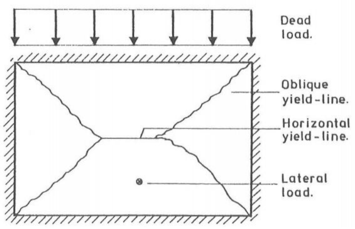

Figure 2.2: Laterally loaded masonry wall with oblique and horizontal yield-lines, [Brinker, 1984]

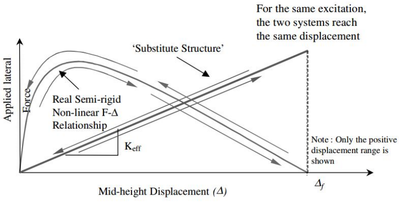

Figure 2.3: Characteristic linear substitute-structure stiffness for displacement analysis, [Doherty et al., 2002]

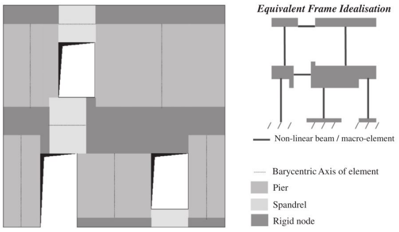

Figure 2.4: Idealisation from facade components to 1D elements, [Lagomarsino et al., 2013]

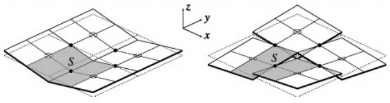

Figure 2.5: Rigid quadrilateral elements connected with rotational springs, [Casolo, 2000]

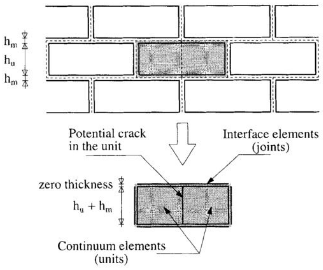

Figure 2.6: Discrete modelling of masonry. Bricks as elastic elements and mortar and potential brick crack lines as interface elements, [Lourenco and Rots, 1997].

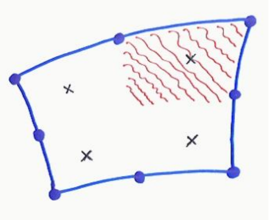

Figure 2.7: Cracked elements, from course CIE5148 (Hendriks and Rots 2012).

3 *Doherty's Experiment*

Geometry The validation of the numerical models will be perfomed with experimental data from Doherty [2000]. Walls of $1.5 \times 0.95 \times 0.11$ m ($h \times b \times t$, Fig. 3.1) are placed on a shake table inside a steel frame (Fig. 3.2).

Boundary Conditions The wall is supported by the steel frame at the top in horizontal direction with the use of two angle cleats (Fig. 3.3). The overburden rig consists of a steel plate that remains horizontal and is pressed on the wall with a translational spring. At the bottom the wall is placed on a damp proof course loose on the table. Since the wall is not rigidly supported at the top and bottom it is able to rotate/rock around it's edges.

Material The material properties are obtained from standardised tests on samples made with the same mortar and bricks as well as on the tested wall specimen themselves. In Table 2.1 material properties for specimen 8, 12, 13 and 14 (of which experimental data is available) are given in addition with the mean and standard deviation of the material properties.

Loads The tests on the specimens are applied in a specific order. For example, first an uncracked static push test at mid-height of the wall is performed on specimen 12, afterwards a series of five transient excitation tests is executed with increasing acceleration amplitudes. This causes all tests with historical earthquake acceleration signals to be on pre-cracked specimen. The most accurate results are found for the Nahanni (NH) 100% acceleration signal on specimen 12. The input accelerations of this signal measured by the instruments at the top (TA) and bottom (TTA) (Fig. 3.2) are depicted in Fig. 3.4 This is also the first dynamic test on this specimen, making it likely that the wall has a small amount of damage. Since the damage is not reported clearly by Doherty it is hard to approximate the experimental results of more severely damaged specimen accurately.

For further reading on Doherty's experiment on out-of-plane bending the reader is referred to Chapter 1 of the Modelling Report, Chapter 5 of the Literature Review and Doherty [2000].

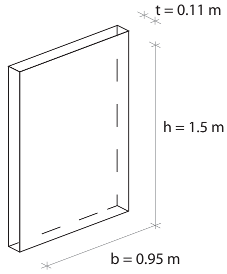

Figure 3.1: Typical dimensions of walls tested by Doherty

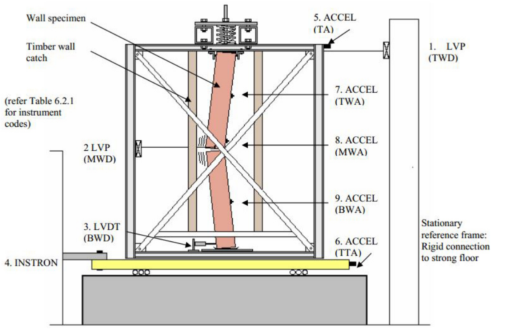

Figure 3.2: Experimental Setup for Out-of-plane testing of URM wall with instruments for measurement of displacements and accelerations [Doherty, 2000]

Figure 3.3: Details of supports experiment Doherty (left: top support, right: bottom support) [Doherty, 2000]

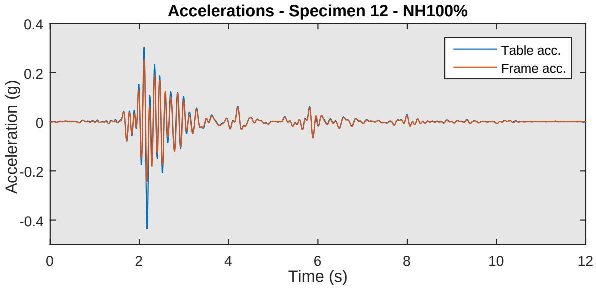

Figure 3.4: Accelerations over time of the Nahanni 100% signal applied on specimen 12 as recorded by the frame (TA) and table (TTA) accelerometers

Specimen	Mass Density	Youngs Modulus	Masonry Compr. Strength	Mortar Compr. Strength	Flexural Tensile Strength
	ρ $[kg/m^3]$	E_m $[MPa]$	f_c $[MPa]$	f_c $[MPa]$	f_t $[MPa]$
8	1800	5,400	9.7	-	0.45
12	1800	11,600	15.7	-	0.30
Mean	-	9,400 / 8,250 *	13.4 / 26.5 *	5.17	0.49
Stan. dev.	-	5,322 / 2,192 *	1.64 / 0.28 *	-	0.15

Table 2.1: Material properties of specimen tested by Doherty. (* The mean values for walls of 110 mm and 50 mm are presented separately.)

4 Finite Element Models

From literature four discretizations were selected. The models are discussed below.

Discretizations

Plane Strain Model smeared cracking The first model uses plane strain elements (Fig. 4.1) which are used as a substitute for three dimensional brick elements. Since for one way bending the length of the wall is not important this dimension is considered of as infinite with the help of the plane strain condition. At the top and bottom line interface elements are used to enforce the boundary conditions.

Plane Strain Model discrete cracking The second model is similar to the first, but has an extra line interface at mid-height, see Fig. 4.1.

Curved Shell Model smeared cracking The third model uses shell elements (Fig. 4.2), for which the thickness direction is reduced to one node. The shells are connected to interface elements via three translational and one rotational degree of freedom. The rotation φ_x and the vertical translation u_y determine the relative displacement Δu in the integration points over the thickness. In these integration points a constitutive t-Δu relationship is prescribed.

Curved Shell Model discrete cracking The last model is similar to the third, but has an extra line interface at mid-height, see Fig. 4.2.

Material models

Smeared cracking For the discretization without interface elements at mid-height of the wall the Total Strain Rotating Crack material model is applied to the quadrilateral elements. When the strength of the material is reached the crack width is smeared over the element as a strain. The σ - ε relationship is defined by the strength, fracture energy and shape of the softening curve. In tension an exponential softening curve is used, in compression this curve has the shape of a parabola, see Fig. 4.3

Discrete cracking For the discretization with interface elements at mid-height of the wall the Discrete Cracking Model us applied to these line interface elements. The other elements in the wall behave elastically. The material model for the interfaces is defined using a t_n-Δu relationship as displayed in Fig. 4.4.

No-tension For the line interface elements at the supports the no-tension material model is applied. The model has a non-linear stiffness diagram with a very small stiffness for relative deformations larger than zero, see Fig. 4.5. The shear resistance is also reduced to zero when an integration point is in tension. The friction failure mode of the bottom support is not modelled.

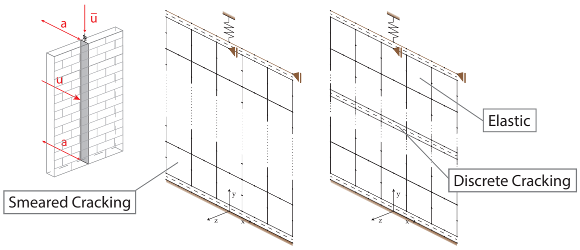

Figure 4.1: Discretization of Plane Strain Model with smeared cracking (left) and Plane Strain Model with discrete cracking (right).

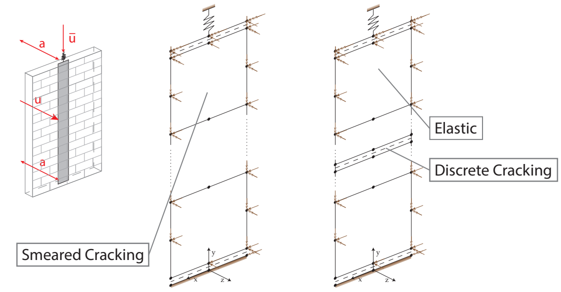

Figure 4.2: Discretization of Curved Shell Model with smeared cracking (left) and Curved Shell Model with discrete cracking (right).

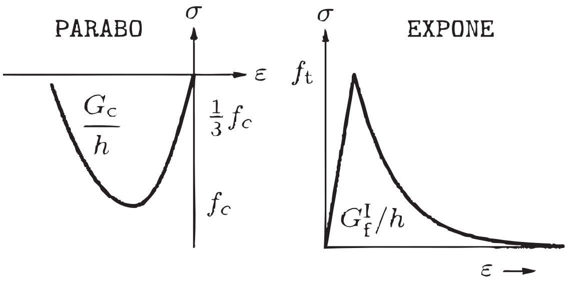

Figure 4.3: Parabolic hardening/softening and exponential softening for Total Strain Model. [TNO DIANA BV, 2014]

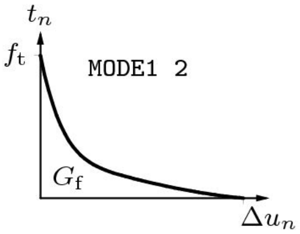

Figure 4.4: Non-linear softening accord. to Hordijk et al. for Discrete Cracking Material Model. [TNO DIANA BV, 2014]

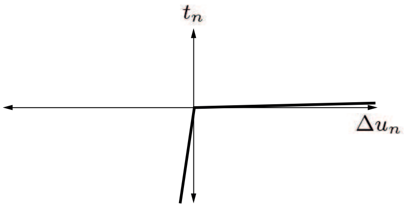

Figure 4.5: No-tension Material Model applied to top and bottom line interface elements as well as cracked line interface elements.

Boundary Conditions

From the physical support conditions explained in Sec. 3, the boundary conditions for the numerical discretizations are derived.

Plane Strain Models The rocking effect is modelled with a line interface in the orthogonal direction of the wall for the Plane Strain Model (Fig. 4.1). This interface has the no-tension material model applied to it, which enables it to rock around the two edges of the wall. At the top of the wall the middle node is supported in horizontal direction to resemble the angle cleats. The overburden rig is modelled with a line interface that behaves identical to the bottom element. The vertical translation of the interface's top nodes are tied with a translational spring. When the spring is loaded by imposing a prescribed displacement $\bar{u}$ of the supported node effectively a stress is applied on the wall.

Curved Shell Models The Curved Shell Model uses line interface elements in the longitudinal direction of the wall to mimic the rocking behaviour (Fig. 4.2). It uses the rotation φ_x and the integration points over the thickness to simulate the rocking behaviour. Since the bottom nodes are supported and the no-tension material model is applied the wall can rock around the outer edges of the wall. The overburden rig is modelled in a similar manner as for the Plane Strain Models. The vertical edges of the shell elements are constraint for translations in the in-plane direction and rotations around the vertical axis. This is to suppress spurious modes during dynamic analysis.

5 *Validation of FE models*

The finite element models discussed in Sec. 4 are executed using DIANA. The results are compared with experimental data from Doherty (Sec. 3).

Static analysis

The static analysis performed is both geometrically as well as physically non-linear. A displacement is imposed at mid-height of the wall with load steps in the order of 0.01 mm. To find convergence of the iteration steps the Newton Raphson method is used, with a relative convergence norm for load, displacement and energy convergence criteria of 1.0×10^{-4}.

In Fig. 5.1 the results from the static push-over test are presented. The initial resistance of the wall is overestimated and the post-peak resistance is slightly underestimated compared to the experiment. After the initial peak the wall is fully cracked and the remaining resistance is totally due to the geometrical stability of the wall. The generated overburden force thus has a high influence on this part.

The overestimation of the physical resistance of the wall is probably the effect of imperfections which are not taken into account by the material tests. Only the Curved Shell Model with discrete cracking drastically overestimates the initial peak. This overestimation is caused by Euler-Bernoulli's hypothesis on which the shell model is based. This is explained in more detail for dynamic analysis. In Fig. 5.2 the results of sensitivity analysis into the interface stiffness are shown. The interface stiffness, expressed as an equivalent URM column height which has similar axial stiffness, is increased for the Plane Strain and Curved Shell Model with discrete cracking. It can be clearly observed that for an increasing stiffness (and thus decreasing equivalent URM column height) the Plane Strain Model with discrete cracking approximates the maximum capacity of the models with smeared cracking, whereas the Curved Shell Model with discrete cracking seems to have no limit for it's capacity.

The post-peak underestimation could be an effect of increasing overburden due to vertical deformation of the wall. The difference between smeared and discrete cracking models is due to the fact that the smeared cracking models have a distributed cracking pattern. This results in a more curved wall resulting in less vertical displacement and thus less overburden.

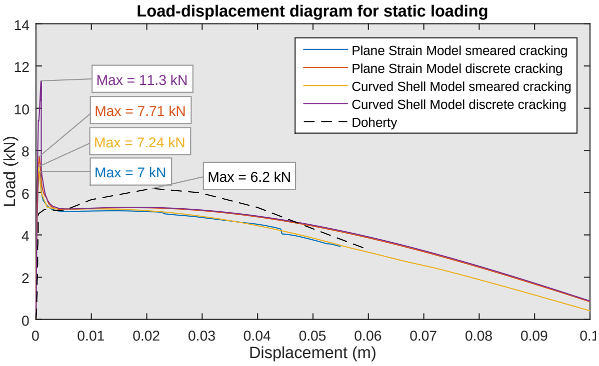

Figure 5.1: Load-displacement diagram for all four discretization compared with the experimental data from Doherty [2000].

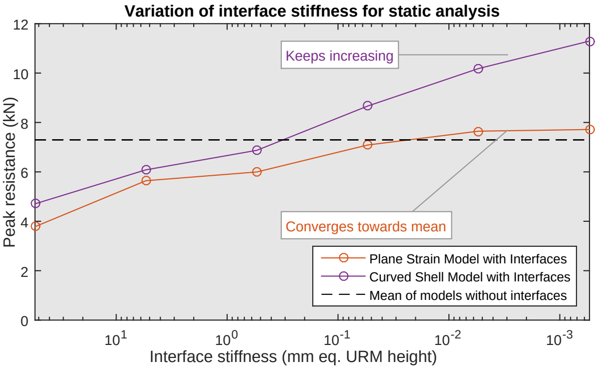

Figure 5.2: Variation of interface stiffness for Curved Shell Model with discrete cracking

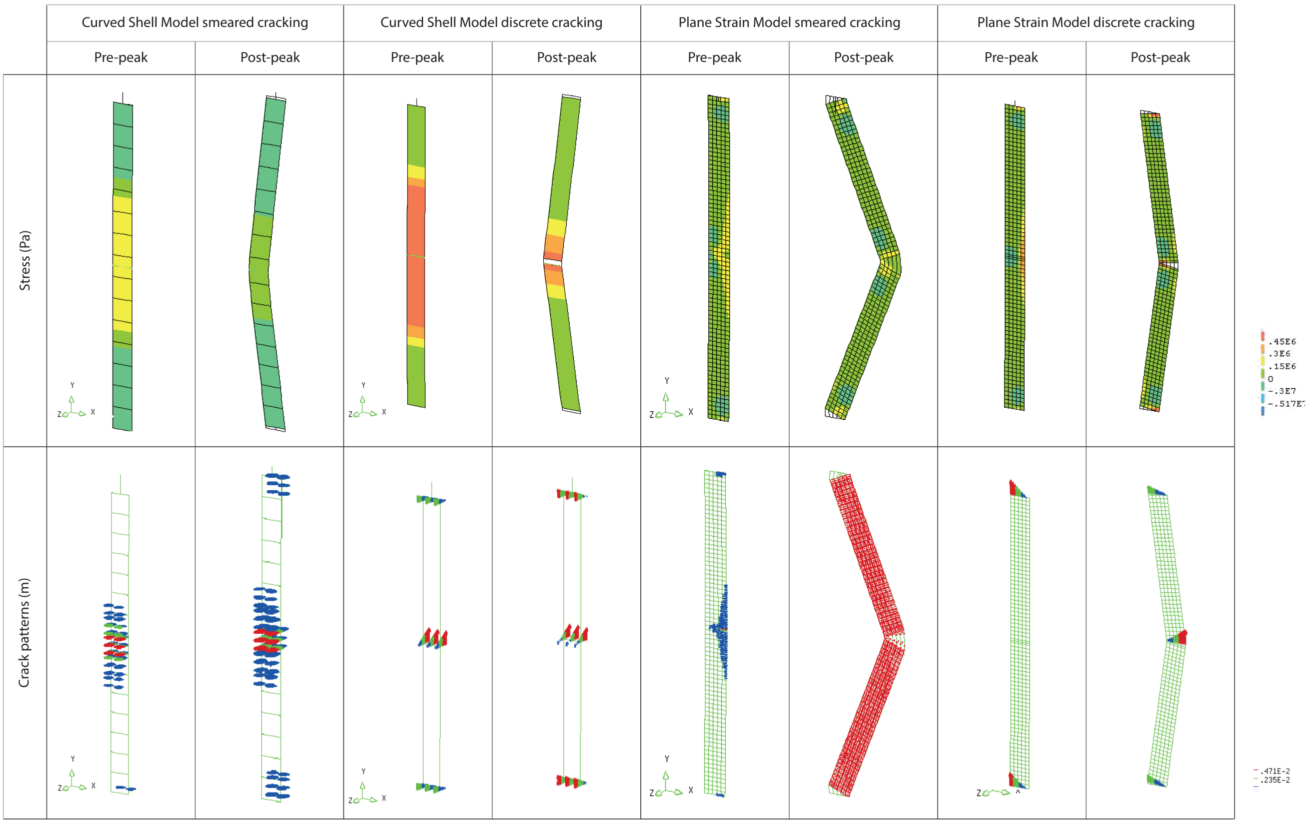

Figure 5.3: Stress (top) and crack/relative deformation plots (bottom) of all four discretizations for pre- and post peak situations.

In Fig. 5.3 the deformation of the wall is shown for pre-peak and post-peak situations. In the pre-peak situations it can be observed that for the models without interface elements at mid-height the cracks are distributed over a certain height. For the Plane Strain and Curved Shell Model with smeared cracking this zone has approximately the same height. However in the Plane Strain Model the number of cracks continues to develop even after a crack at mid-height has formed with a great crack width. The models with mid-height interface elements show more concentrated stress plots, except for the Curved Shell Model pre-peak. This was caused by the high compressive interface stiffness as shown earlier. The relative deformation plots of these models show that the main deformation in the interfaces is tensile deformation, which confirms the rocking effect.

The efficiency of the methods is compared by comparing the average computing time. Since the computing time is a combination of number of iterations and time per iteration it is dependent on the convergence as well as the number of nodes. The discrete cracking models both converge easily and therefore have an average computing time of 2 min. The Plane Strain and Curved Shell Model with smeared cracking have an average computing time of 20 and 7 min.

Dynamic Analysis

The dynamic analysis performed is both geometrically as well as physically non-linear. The Backward Euler time integration scheme is used with time steps of $0.002s$. To find convergence of the iteration steps the Newton Raphson method is used, with a relative convergence norm for load, displacement and energy convergence criteria of 1.0×10^{-4}.

For the dynamic analysis, models without interface elements at mid-height were found to be unsuitable. Since the experiments were on cracked walls a phased analysis was performed in which the wall was first cracked with a static analysis as explained above whereafter it was excited by imposed accelerations at the bottom and top support. This however resulted in early divergence which could not be solved by smaller time steps. Directly imposing the acceleration signals on uncracked walls did not generate a sufficient amount of cracks to start the wall to rock.

The models with interface elements did result in suitable results. For both the Plane Strain and the Curved Shell Model with discrete cracking, rocking behaviour similar to experimental data was found, see Fig. 5.4. From a Fast Fourier Transform the amplitude spectra were obtained. The governing frequency, which is the frequency with the biggest amplitude, corresponds to the rocking frequency, see Fig. 5.5. This frequency is especially well approximated by the Curved Shell Model with discrete cracking.

Two important parameters were optimized to find these results; the thickness of the wall at the mid-height of the wall and the compressive stiffness of the interface elements. The thickness can be reduced if mortar drops out of the joints. The rotation of the wall is then no longer around the outer edges of the wall causing the geometric resistance to be smaller and thus the reaction to accelerations to be bigger.

The compressive stiffness of the line interface material model was found to be of the most significant influence for the Curved Shell Model with discrete cracking. Normally, the compressive stress of interface elements should be set in such a way that compressive deformation is observed mainly in the structural elements and not in the line interface. This is achieved by choosing a relative high dummy stiffness k for the line interface, using e.g. a factor thousand, $k = \frac{E}{h_{elem}} \cdot 10^3$, where E is the Modulus of Elasticity and h_{elem} the typical length of the neighbouring elements. However this validation shows that the stiffness should be chosen much lower. If the stiffness is chosen too high no effect is found for the out-of-plane direction. This would thus lead to an overestimation of the capacity, which can lead to dangerious situations where buildings are validated to be safe, but in reality will fail due to out-of-plane bending.

The reason for the lower interface stiffness to give a correct response is found from studying the deformation of the wall during opening of the crack. From the Plane Strain Model with discrete cracking it can be found that during opening of the crack the deformation is non-linear over the thickness (Fig. 5.6 top). Small deformations are found in the compressive zone, whereas big deformations are found where the crack has opened. In the Curved Shell Model with discrete cracking these deformations are not possible since the interface elements are based upon Euler-Bernoulli's hypothesis: plane section remain plane (Fig. 5.6 bottom). When a high dummy stiffness is used, only very small compressive deformations are allowed which causes the point of rotation to be on the very edge of the cross-section. This greater distance to the point of rotation causes the wall to have a greater resistance against deformations which will thus remain small.

When only shell elements are used with smeared cracking this problem does not occur since there is no high dummy stiffness. Instead the Modulus of Elasticity E is used to calculate the stresses over the thickness of the wall. Since this stiffness is equal to that of the plane strain elements a similar compressive zone can be formed and thus correct static peak resistance can be found, see Fig. 5.1.

The solution to this problem lies in reducing the stiffness in such a way that the plane section can remain plane but the point of rotation follows the crack tip during the opening of the crack similar to the Plane Strain Model with discrete cracking.

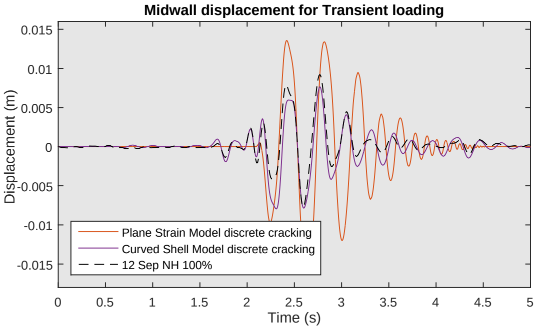

Figure 5.4: Time-displacement diagram for Curved Shell and Plane Strain Model with discrete cracking.

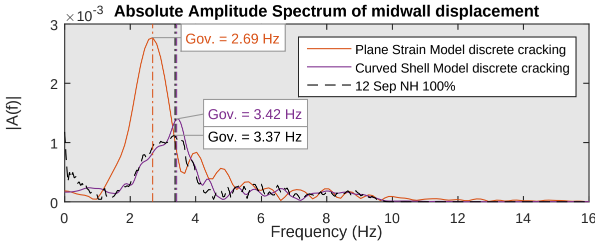

Figure 5.5: Amplitude spectrum of midwall displacement for Curved Shell and Plane Strain Model discrete cracking.

Deformation of Plane Strain Model with discrete cracking

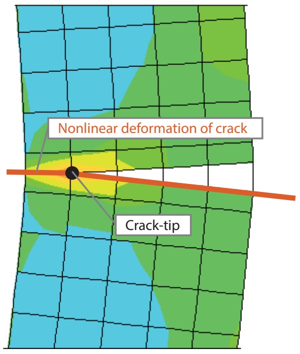

Deformation of Curved Shell Model with discrete cracking

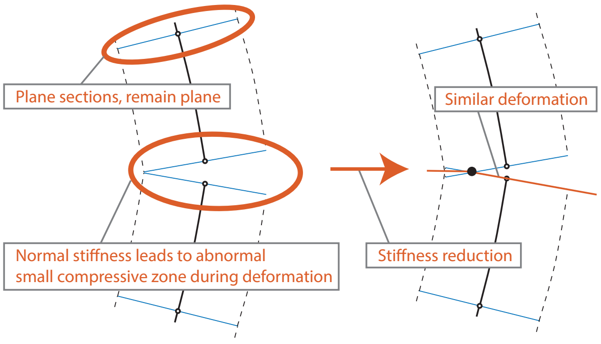

Figure 5.6: Reduction of interface stiffness enables the Curved Shell Model with discrete cracking to have the same deformation behaviour as the Plane Strain Model with discrete cracking.

The appropriate reduction for static analysis can be obtained from comparison of the peak capacity with other models, see Fig. 5.2. For dynamic analysis this is obtained from comparison the experimental data of Doherty [2000]. In Fig. 5.7 and 5.8 the results of a sensitivity analysis are given for the governing frequency and maximum amplitude. The appropriate stiffness is in the order of 0.1 mm which is similar to the results found from the static sensitivity analysis.

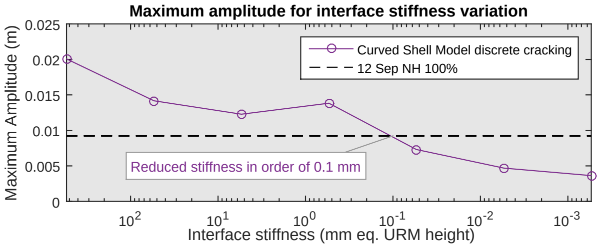

Figure 5.7: Maximum amplitude for variation of interface stiffness for the Curved Shell Model with discrete cracking

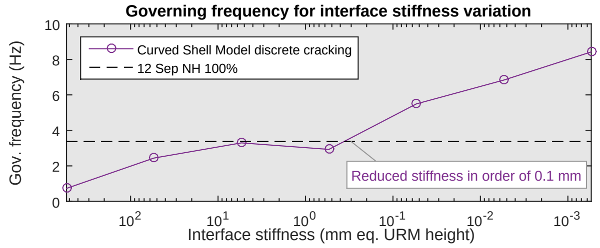

Figure 5.8: Governing frequency for variation of interface stiffness for the Curved Shell Model with discrete cracking

In Fig. 5.9 and 5.10 results from an investigation on the influence of the Youngs Modulus and the wall thickness on the reduced interface stiffness is presented. This is done using the static comparison approach from Fig. 5.2. From the first figure it can be concluded that there is no influence of the Youngs Modulus on the reduced stiffness. From the second figure it is concluded that the thickness of the wall does influence the stiffness reduction.

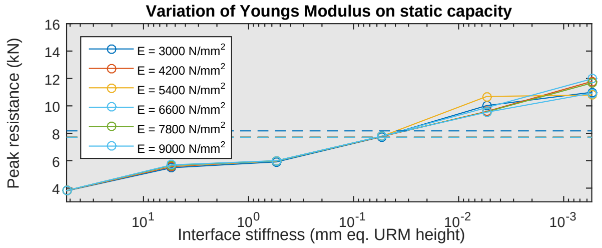

Figure 5.9: Influence of Youngs Modulus on static peak capacity is insignificant.

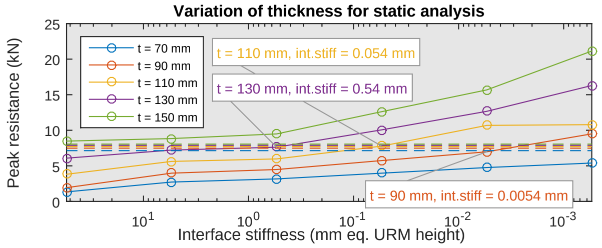

Figure 5.10: Influence of wall thickness t on static peak capacity is significant.

6 *Comparison with analytical calculation NPR 9998*

The validated numerical model can be used for comparison with the new guideline for earthquake resistant constructing in the Netherlands, the NPR 9998. It serves as an informative National Annex to NEN-EN 1998-1 and gives clarification where needed.

For resistance of unreinforced masonry walls NEN-EN 1998-1 recommends the restriction of geometric properties to be specified in the National Annex. NPR 9998 has a different approach. It requires that URM walls should be able to resist earthquakes in out-of-plane direction (NPR 9998, 9.1.1, note for NEN-EN 1998-1, 9.5.1(5)). This can be checked by using a non-linear time history analysis or by using a check of the capacity according to NEN-EN 1996-1-1 with an equivalent horizontal loading in the out-of-plane direction.

The analytical method with equivalent loading is described in the report [Wijte, 2014] and schematically depicted in Fig. 6.1. In this approach Wijte lumps the mass of the wall in three points. The horizontal load is distributed as point loads over the three point masses proportional to the horizontal displacement of the wall. These forces are equivalent to the Peak Ground Acceleration (PGA) of an earthquake. The relation between the accelerations and the point loads is formed by the multiplication of the mass and acceleration with the Dynamic Amplification Factor (DAF). This DAF is obtained from a design spectrum. The characteristic period T and the behavioural factor q on which the design spectrum is based are obtained from the load-displacement relationship of the wall during imposed horizontal loading.

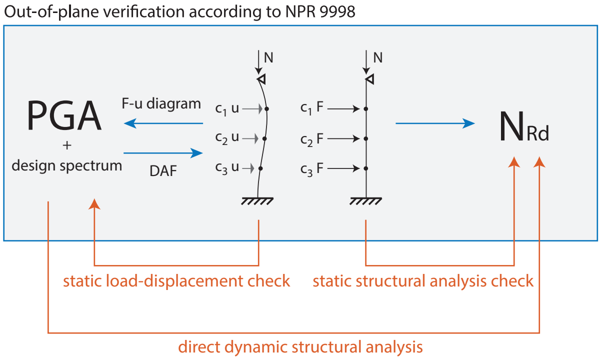

Figure 6.1: Schematic representation of calculation steps of Wijte (green arrows) and numerical checks (blue arrows)

From the assumed boundary conditions the eccentricity of this axial force can be found, see Fig. 6.2. The applied external forces lead to a moment distribution along the height h of the wall. With this moment distribution and the axial load the wall capacity N_{Rd} is checked according to NEN-EN 1996-1-1. This check is based on the axial compressive strength of the cross-section reduced by a factor which is dependent on the slenderness, eccentricity and loading of the wall. These three effects are all expressed as an eccentricity e and the reduction factor is a linear function from 1 for $e = 0$ to 0 for $e = \frac{1}{2}t$ at the top and bottom. At mid-height the eccentricity due to horizontal loading is high and the reduction factor, which is a exponential function given in appendix G of NEN-EN 1996-1-1, reduces the capacity for axial loading significantly.

This equivalent loading method is compared with the validated numerical models explained in Section 5. Three comparisons are performed to check different aspects of the analytical calculation. These are indicated in Fig. 6.1 to give an overview of the analytical calculation and the checks performed.

First a static analysis is used to verify the structural integrity check according to NEN-EN 1996-1-1. In Fig. 6.3 the static capacity of the four validated numerical models is shown for increasing overburden ratio's. Although some of the models show some divergent results, the capacity trends towards an increase for low overburden ratio's and a decrease when the overburden increase to full axial strength. In the first stage the compressive force has a beneficial effect while is the second stage the wall fails early due to crushing.

These results are obtained with boundary conditions similar to the ones assumed by Doherty. If these boundary conditions are used to verify the wall according to NEN-EN 1996-1-1 the results of Fig. 6.4 are obtained. The difference between the numerical and the analytical resistance is explained by the fact that NEN-EN 1996-1-1 does not take tensile strength into account and does not allow high axial loads due to stability considerations. This is not taken into account by the plane strain model, since this should be doen with a separate stability analysis in DIANA.

The second comparison is made between the load-displacement diagram used to find the design spectra and DAF values. In Fig. 6.5 the load-displacement diagram according to Wijte and from the Plane Strain Model with smeared cracking are presented. Wijte uses a derived moment-curvature relationship (Fig. 6.6) were the tensile strength is not taken into account. The derivation is performed with MATLAB both with and without tensile strength, similar

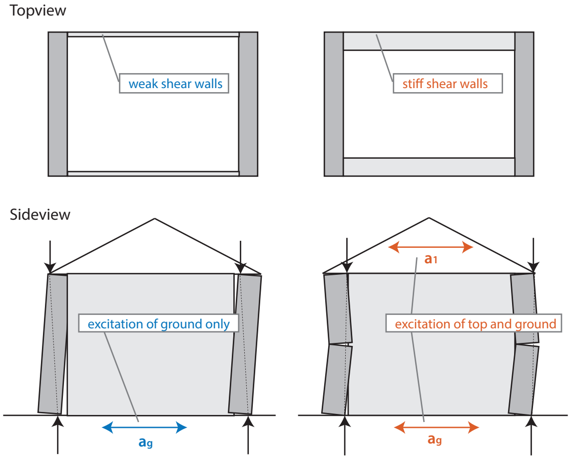

Figure 6.2: Static capacity of numerical models for increasing overburden.

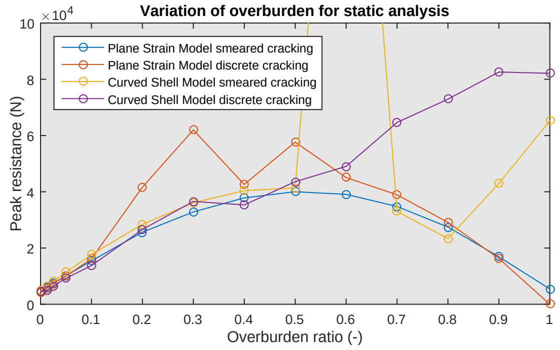

Figure 6.3: Static capacity of numerical models for increasing overburden.

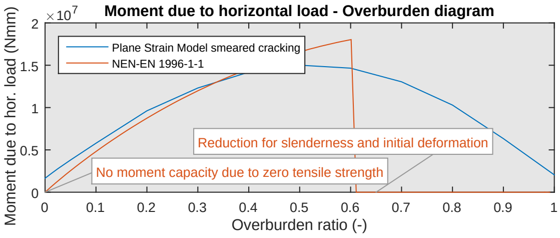

Figure 6.4: Moment capacity for horizontal loading for increasing overburden compared with NEN-EN 1996-1-1.

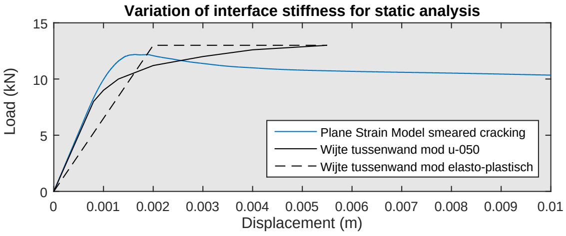

Figure 6.5: Comparison of load-displacement diagram

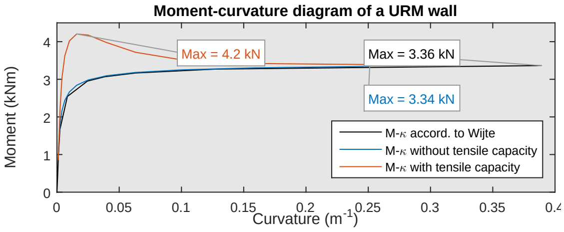

Figure 6.6: Relationship between moment due to horizontal loading and axial force.

results are found. The difference in the load displacement diagram of Fig. 6.5. Could be due to several effects. In the moment-curvature derivation the normal force is assumed to be applied at the centre of the cross-section. However the eccentricity of the normal force varies over the height and is dependent on deformations. These effects are taken into account by the Plane Strain Model with smeared cracking. The difference has an effect on the parameters T and q on which the design spectrum is based.

It should also be noted that for this derivation the horizontal boundary condition at the top of the wall is assumed to be fully constraint. This is different from the assumption made as sketched in Fig. 6.2.

The final comparison with the analytical calculation is made with the dynamic analysis. For this goal an harmonic acceleration signal with increasing amplitude is imposed on the numerical Plane Strain Model with smeared cracking. The acceleration for which the first crack develops is given in Fig. 6.7. It can be observed that the difference is very big.

This difference can be explained by the various assumed boundary conditions. In Wijte's analytical check according to NEN-EN 1996-1-1 the wall check is dependent on the resistance at mid-height, which is heavily reduced due to the moment in that cross-section. There is no balancing moment from the axial load since the eccentricity of the axial load is zero due to the assumed boundary conditions, see Fig. 6.2. If the boundary conditions of Doherty are used the balancing moment increases and thus the resistance of the wall.

The assumption of the boundary conditions depends on the stiffness of the structure as a whole. If the structure has stiff walls orthogonal to the walls verified for out-of-plane resistance that are well connected to the upper floor it can be assumed that these walls and the upper floor will start vibrating with similar excitations as the ground. This phenomenon is described by Priestly [1985], see Fig. 6.8. This will cause the wall to be excited both on the top as well as on the bottom boundaries. This justifies the assumptions of Doherty.

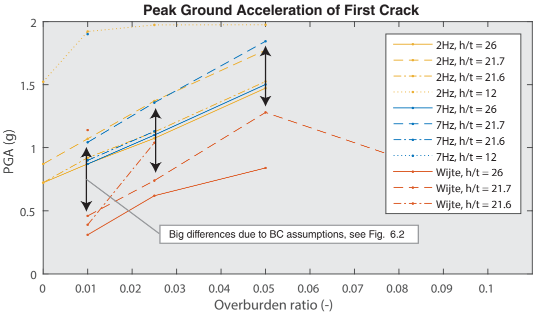

Figure 6.7: Peak ground accelerations of first crack for endwalls show big differences with results from Wijte due to difference in BC assumptions as indicated in Fig. 6.2.

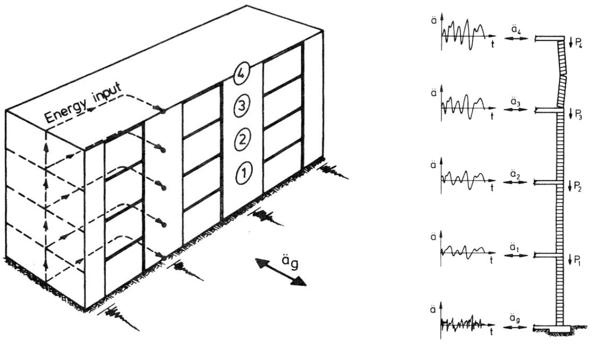

Figure 6.8: Acceleration signal is transferred via the shear walls to upper floors [Priestly, 1985]

7 Conclusion

Four numerical models of a URM wall subjected to out-of-plane excitations have been developed. From validation of the Plane Strain and Curved Shell Model for discrete and smeared crack material model with the experimental results of Doherty the following conclusions can be drawn.

For static analysis all models are able to give an accurate approximation of the physical and geometrical resistance in comparison with the experimental results. However, when the Curved Shell Model with discrete cracking is used the line interface stiffness should be reduced. This study has shown that it is likely that the reduction is dependent on at least the thickness of the wall and is similar for both static and dynamic analysis. Although it is not yet possible to give an estimate of the stiffness reduction a priori, it is possible to give an estimate of the reduction by comparing the results of a sensitivity analysis with the Plane Strain Model.

For dynamic analysis accurate results for models with smeared cracking were not found. Also the out-of-plane resistance for the Curved Shell Model with discrete cracking is overestimated when the interface stiffness is not sufficiently reduced. It should also be noted that the crack pattern should be known a priori, although this can be accurately found from a static analysis with shell elements and smeared cracking.

The efficiency of the numerical models depends on the number of nodes in the model and the material model that is applied. This was found from average computing times of the models. The Curved Shell Model with discrete cracking is the most efficient for modelling out-of-plane bending of URM walls, whereas the Plane Strain Model with smeared cracking is the least efficient. However if the reduced interface stiffness cannot be obtained directly a sensitivity analysis is needed making this approach less favourable.

The goal of this study was to validate different FE models that are able to model the out-of-plane bending of URM walls in an accurate and efficient way. This study has shown that all four models are able to find accurate results. The efficiency of the models depends on the knowledge about the stiffness reduction a priori. It is therefore case dependent which Finite Element (FE) model is best to use.

As an application of the validated numerical model a comparison is made with the analytical calculation of URM walls loaded in out-of-plane bending according to NPR 9998. The comparison has shown that the assumption on the boundary condition are most important since these influence the points of application of the overburden force and the reaction force at the bottom support which determines the resistance statically as well as dynamically. Furthermore the analytical approach does not take into account tensile strength making it conservative for low overburden ratio's. This also results in a lower elastic stiffness of the equivalent elasto-plastic load-displacement curve, which in turn influences the design spectrum and DAF for determining the peak ground acceleration.

8 Recommendations

To improve the knowledge and guidelines considering out-of-plane bending for URM walls more investigation is needed into the reduction of interface stiffness. Since shell elements are far more efficient for big structures these are the preferred elements for analysis. As made plausible in this study there seems to be a relation between the thickness of a URM wall and the reduced stiffness. This should be further investigated with more experimental data and more numerical tests. Furthermore the influence of other properties like the dimensions of neighbouring elements should be investigated.

Apart from the reduction itself also it's influence on in-plane behaviour should be examined. For out-of-plane behaviour it is important to reduce the stiffness but for in-plane behaviour this could lead to lower resistance. For three dimensional modelling both situations are important and should give safe estimations of the capacity.

More investigation into the effects of the boundary conditions on the out-of-plane resistance for the NPR 9998 is required. If some eccentricity of the normal force at the mid-height cross-section of the wall is allowed this would increase the capacity of the wall significantly. A better explanation of the assumptions could clarify it's effects and thus leave room for other assumptions which can be used for strengthening purposes.

References

Rune Brinker. Yield-Line Theory and Material Properties o f Laterally Loaded Masonry Walls. *Masonry International*, 1:8–17, 1984.

Siro Casolo. Modelling the out-of-plane seismic behaviour of masonry walls by rigid elements. *Earthquake Engineering & Structural Dynamics*, 29 (September):1797–1813, 2000.

K. Doherty, M. C. Griffith, N. Lam, and J. Wilson. Displacement-based seismic analysis for out-of-plane bending of unreinforced masonry walls. *Earthquake Engineering & Structural Dynamics*, 31(4):833–850, 2002.

Kevin Thomas Doherty. *An investigation of the weak links in the seismic load path of unreinforced masonary buildings*. Phd, University of Adelaide A, 2000.

Sergio Lagomarsino, Andrea Penna, Alessandro Galasco, and Serena Cattari. TREMURI program: An equivalent frame model for the nonlinear seismic analysis of masonry buildings. *Engineering Structures*, 56:1787–1799, 2013.

Paulo B. Lourenço. Anisotropic softening model for masonry plates and shells. *Journal of Structural Engineering*, 126(9):1008–1016, 2000.

Paulo B. Lourenco and Jan G. Rots. Multisurface interface model for analysis of masonry structures. *Journal of engineering mechanics*, 123(7):660–668, 1997.

NEN. NEN-EN 1998-1:2005: Eurocode 8 - Ontwerp en berekening van aardbevingsbestendige constucties - Deel 1: Algemene regels, seismische belastingen en regels voor gebouwen. Technical report, Nederlands Normalisatie-instituut, Delft, 2005.

NEN. NEN-EN 1996-1-1 + A1: Eurocode 6 - Ontwerp en berekening van constructies van metselwerk - Deel 1-1: Algemene regels voor constructies van gewapend en ongewapend metselwerk. Technical report, Nederlands Normalisatie-instituut, Delft, The Netherlands, 2015a.

NEN. NPR 9998: Nederlandse praktijkrichtlijn: Beoordeling van de constructieve veiligheid van een gebouw bij nieuwbouw, verbouw en afkeuren - Grondslagen voor aardbevingsbelastingen: Geïnduceerde aardbevingen. Technical report, Nederlands Normalisatie-instituut, Delft, The Netherlands, 2015b.

M.J.N. Priestly. Seismic behaviour of unreinforced masonry walls. *Bulletin of the New Zealand National Society for Earthquake Engineering*, 18(2):191 – 205, 1985.

Pere Roca, Climent Molins, Antonio R Marí, and M Asce. Strength Capacity of Masonry Wall Structures by the Equivalent Frame Method. *Journal of Structural Engineering*, 130(10):1601–1610, 2005.

Akenori Shibata and Mete A Sozen. Substitute-structure method for seismic design in R/C. *Journal of the Structural Division*, 102(1):1–18, 1976.

TNO DIANA BV. *DIANA-9.6 User's Manual*. Delft, The Netherlands, 2014.

J. van Dam. *Literature Review: Out-of-plane bending of URM masonry*. Msc thesis, Delft University of Technology, 2015a.

J. van Dam. *Modelling Report: Out-of-plane bending of URM masonry*. Msc thesis, Delft University of Technology, 2015b.

Simon Wijte. Notitie 24-11-2014, NPR 9998 Metselwerkwanden belast uit het vlak. Technical report, Rijswijk, The Netherlands, 2014.

List of symbols

ε Strain. 5

φ Rotation of node. 5

σ Stress. 5

Δu Relative deformation. 5

b Width of the URM wall. 4

E Modulus of Elasticity. 8

e Eccentricity. 10

N_{Rd} Axial design capacity of the URM wall according to NEN-EN 1996-1-1 reduced for imperfections and horizontal load. 10

k Dummy interface stiffness. 8

T Period of a vibration of a one-mass-spring system. 11

h Height of the URM wall. 4, 10

q Behavioural factor of a one-mass-spring system. 11

t Thickness of the URM wall. 4, 9

t_n Traction normal to the interface. 5

u Imposed displacement at mid-height of the URM wall. 5

$\bar{u}$ Prescribed displacement of spring to impose overburden stress. 6

Nomenclature

cross-validation Validation in which results from different FE implementations are compared to obtain better results. 2

discrete cracking Modelling approach in which the discrete deformation of a crack is represented by a relative displacement between two nodes. 2

equivalent URM column height Stiffness of an interface element expressed as the axial stiffness of an equivalent URM column of a certain height. 6

FE implementation Computer program which can be used for numerical calculations using finite elements. 2

interface elements Elements with zero thickness in which a relation is described between the traction and the relative displacement over sets of nodes. 2

interface stiffness The compressive dummy stiffness of an interface element which is used to keep the deformation in the interface to a minimum when non-tensile loads are applied. 1

load-displacement diagram Relation between the horizontally applied load and the horizontal displacement at the same position. 2

micro-modelling Modelling of materials using the stress properties of the wall to model deformations and failure in integration points. 1

numerical validation Comparison of a numerical model with experimental data to check it's validity. 1

one-way bending Situation in which a walls spans in one direction either from top to bottom or left to right. 1

out-of-plane bending Bending of a wall around an axis which intersect with the plane of the wall, for example around the length or height of the wall. 1

overburden The load that is applied on top of the wall and applies a compressive axial force on the wall. 1

plane strain elements Two dimensional finite elements in which the strain out-of-plane is equal to zero.. 2

quasi-static Load procedure in which the load is slowly increased to reduce inertia effects. 1

shell elements Two dimensional finite elements which represent structures of which one dimension is small in comparison with the other two.. 1

smeared cracking Modelling approach in which the discrete deformation of a crack is represented as a smeared strain over an element. 2

time history analysis Analysis over time in which an historical acceleration signal of an earthquake can be applied. 2

Acronyms

DAF Dynamic Amplification Factor. 9, 10, 12

FE Finite Element. 1–3, 12

LDBA Linearized Displacement Based Analysis. 2

NAM Nederlandse Aardolie Maatschappij. 1

NPR Nederlandse Praktijkrichtlijn. 1, 2, 9, 12

PGA Peak Ground Acceleration. 9

URM Unreinforced Masonry. 1

JOS VAN DAM

LITERATURE REVIEW

DELFT UNIVERSITY OF TECHNOLOGY

Revisions

Rev.	date	status	remark
0	30-9-2014	concept	Discussed at first committee meeting
1	14-1-2015	concept	- Corrected anisotropic and orthotropic definitions in Sec. 3.1 and 3.2 - Added Chapter 4 *Use of Masonry in Buildings* - Rewritten Sec. 7.6 *Anisotropic Continuum Model* - More quantifiable comparison of methods, see Table 7.1 - Visualisation of methods Chapter 7 - Grammatical corrections
2	26-1-2015	concept	- Grammatical corrections - Comments from Karel Terwel
3	4-6-2015	final	

STRUCTURAL MECHANICS, DELFT UNIVERSITY OF TECHNOLOGY

Submitted on 4th June 2015. Revision 3

Contents

Introduction

Masonry is one of the most used buildings materials worldwide. It performs very well in resisting gravity loads, is available anywhere and is relatively cheap and easy to work with. However, it does not preform well when loaded in a lateral direction, for instance due to earthquakes. unreinforced masonry (URM) buildings are relatively weak against earthquakes when compared to reinforced concrete, steel and wood. This low resistance to lateral forces derives from the low tensile strength as well as from the brittle nature of the materials. Bruneau (1994) had the following to say about this phenomenon:

> "The potential out-of-plane failure of URM elements (...) during earthquakes constitutes the most serious life-safety harzard for this type of construction."

This report is a literature review about the behaviour of URM loaded in the out-of-plane direction by earthquakes. The report constitutes part of my master's thesis and is part of a research program relating to induced earthquakes in Groningen, as explained in Chapter 1. The next things to discuss are the characteristics of earthquakes (Chapter 2) and unreinforced masonry (Chapter 3). To translate the masonry structure into a realistic model some information about the use of masonry in buildings is given in Chapter 4. The experimental research which will be used as data for experimental validation and for the cross validation of methods is presented in Chapter 5. Time-integration methods are briefly discussed in Chapter 6. Chapter 7 discusses the most important methodologies for analysing out-of-plane loaded URM walls, and will conclude with a comparison of the methods. Finally, the overall conclusions are given (Chapter 8) in which the research questions of the remaining part of this thesis are presented.

1

Earthquakes in Groningen

Gas extraction in Groningen causes earthquakes. The first extractions from the Groningen gas field commenced in 1963. On December 26 1986 the first earthquake was recorded near Assen. Until December 2013 about 1000 earthquakes had been reported (KNMI, 2013). The strongest earthquake was found to have a magnitude of 3.6 on the Richter scale.

While in the early years the earthquakes were mild and infrequent, in recent years they have become more severe. Houses have suffered greater damage and some farms have even collapsed (RTV Noord, 2014). The earthquake in Huizinge on August 16 2012, which was experienced as being too severe, was the reason for the government to act.

The Minister of Economic Affairs opened a research program which led to a change in the NAM's "winningsplan". This plan has once again become valid until 2016, when the NAM has to present a new version. As a part of this plan, the NAM has to make a *deformation model*, about the ground response to the gas extraction, as well as an *exposure model*, about the buildings' response to the ground.

For the exposure model the NAM has asked TU Delft, ARUP and EUCENTRE to take part in a joint research program. In this program, physical tests and cross validation modelling will be performed. The cross validation modelling comprises benchmarks and typologies.

This master's thesis is about one of the benchmarks, the experimental study carried out by Doherty (2000). He studied the dynamic behaviour of unreinforced masonry walls subjected to one-way out-of-plane bending, this will be further discussed in Chapter 5.

2

Load Characteristics

2.1 *Earthquakes*

An earthquake is a sudden release of stress in the earth due to shifting of different soil layers. This shifting causes seismic waves travelling through the earth causing the earth to shake with a certain frequency and amplitude. This wave travels from the epicentre in three directions. Therefore the shaking of the earth is in horizontal as well as vertical direction. Most earthquakes originate from tectonic faults which can be 700 km deep. A depth of less than 70 km qualifies as shallow.

The earthquakes in Groningen are induced earthquakes which means that they are the effect of human action. The gas is extracted from a permeable stone layer at three kilometres depth. The layer is covered with a non-permeable stone layer to store the gas. If the gas is extracted the permeable stone layer has three kilometres of rock to carry without the gas pressure. This is not possible so the soil subsides. This can go slowly or in shocks. (KNMI, 2013)

The acceleration of an earthquake is mostly characterized by a short period of increasing amplitude followed by a period of constant strong ground motion and a longer period of degrading ground motion.

2.2 *Loading methods*

Calvi and Kingsley (1996) give a good explanation of ways to simulate seismic motion. In this report a fourth category is added which is static pushover.

Static Pushover is used in many studies to find the load-displacement relationship as well as the maximum load. Although this method does not represent the seismic load in a realistic way it does give insight into the behaviour of the structure as well as a possible failure mechanism. Mendes and Lourenço (2009) describes an adaptive pushover technique to push in proportion to higher eigenmodes.

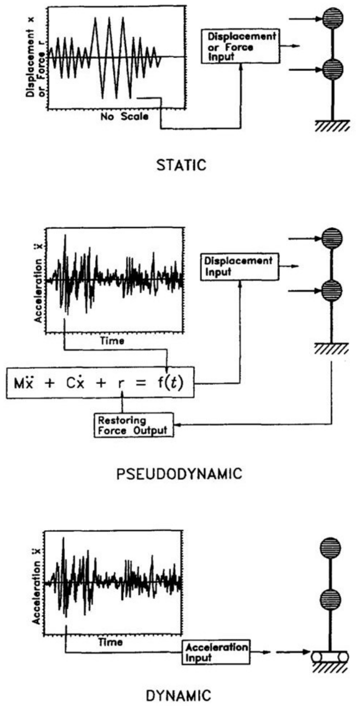

Figure 2.1: Static, pseudo-dynamic and dynamic tests of MDOF, (Calvi and Kingsley, 1996).

Quasi-static testing is applying a displacement or a force as input over a number of cycles. This method can be used to find geometrical or material influences in the loading and unloading process. It does not take into account the inertial forces neither higher natural frequency modes of the structure. Therefore this method does not represent the dynamic characteristics of an earthquake response.

Pseudo-dynamic testing is a method to take into account the inertial forces. It is a computer controlled method where numerically the equations of motions are solved. The displacements are applied on the system and the reaction forces are put back in the equations of motion to find the next displacement. Advantage of this method is that it is displacement controlled which makes it possible to find the post-peak behaviour of a structure.

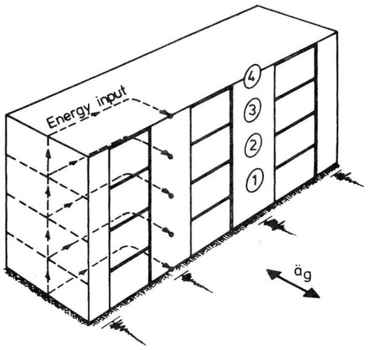

Figure 2.2: Load path of the imposed earthquakes through the stiff parts of the construction, from (Priestly, 1985).

Dynamic testing is simply applying an acceleration at the supports of a structure. This gives a realistic representation of the earthquake. It is however harder to find the post-peak behaviour since the displacement of the structure is not controlled.

Calvi and Kingsley (1996) state that especially in MDOF systems quasi-static load input is not realistic since this only loads the first eigenmode. Therefore a dynamic or pseudo-dynamic method should be applied.

Mendes and Lourenço (2009) find from an experimental case study on "Gaioleiro" buildings that static pushover results in another failure mode than dynamic excitation. This is because static pushover pushes the structure in its first eigenmode. For these buildings this is however not governing. Adaptive pushover analysis can account for this problem.

2.3 Dynamic filtering and Phase difference

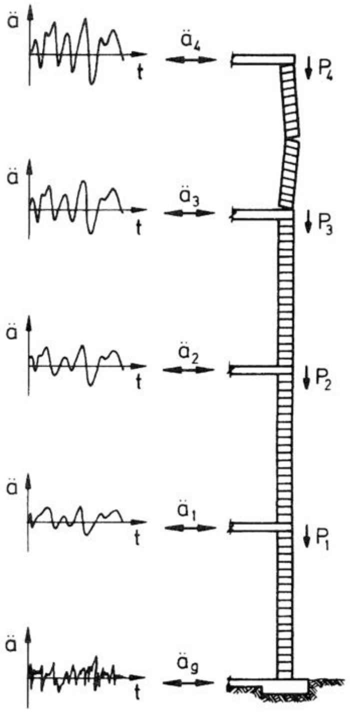

Figure 2.3: Resulting accelerations per floor, from (Priestly, 1985).

Since masonry walls in buildings are connected to other walls dynamic filtering can change the earthquake acceleration applied to the laterally loaded wall. Priestly (1985) suggests that the dynamic excitation of the boundaries of a out-of-plane wall are affected by dynamic filtering. In other words the excitation of the top boundary of the lateral wall is the response of the in-plane walls and floor to the excitation. A visualization of this effect is given in Fig. 2.2 and 2.3.

The phase difference in input of the accelerations at the top and bottom of the wall have an effect on the displacement and deformation of the wall. However, ABK (1984) found that the critical case is no phase difference and thus an in-phase excitation of both top and bottom is used in experiments and numerical simulations.

2.4 *Types of input*

If earthquakes are simulated in experiments or numerically by imposed accelerations a few different types of input can be used.

Recorded earthquakes, or natural accelerograms, can be used to give a realistic view of the response of the structure to an earthquake. The results however do not give decisive answers. Every earthquake has a completely different signature, both frequency, duration and peak ground acceleration can be different. The question if an earthquake is destructive depends also on the natural frequency of the structure. A big draw back of these accelerograms is the limited availability, which requires scaling to get a higher diversity of input.

Artificial accelerograms can produce more earthquakes, which reduces the disadvantage of recorded earthquakes. An artificial accelerogram should be compatible with a design response spectrum defined by a local code or the Eurocode. However according to Penna et al. (2013) these are not preferable over recorded earthquakes, since natural accelerograms have all the aspects which influence earthquakes like source, path and site as wells as the relation between vertical and horizontal acceleration. Calvi and Kingsley (1996) give an example of two natural accelerograms and spectral accelerations to compare these, see Fig. 2.5 and 2.4. As can be seen the artificial earthquake clearly has a different character having a far longer period of high peaks. Also the spectral accelerations show an other composition, the artificial acceleration has more high frequency and less low frequency accelerations. Therefore Calvi and Kingsley (1996) conclude that an artificial accelerogram is not a good representation of a real earthquake.

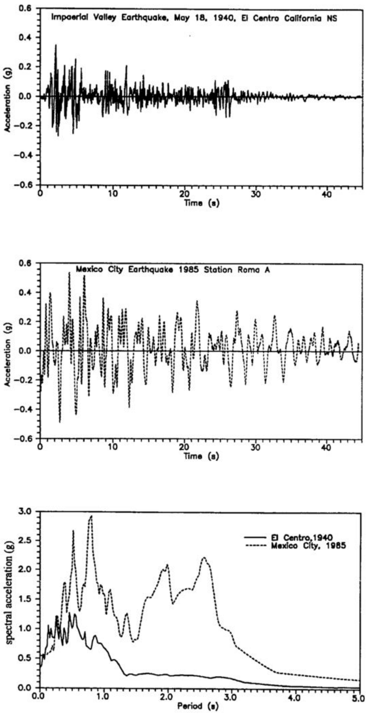

Figure 2.4: Natural accelerations and spectral acceleration, (Calvi and Kingsley, 1996).

Harmonic accelerograms with increasing amplitude can be used to find the influence of different frequencies on the response, as well as the ultimate acceleration before instability for a given frequency.

Impulse and free vibration tests are to observe the free vibration of the wall from which the natural frequency can be found, as well as damping characteristics.

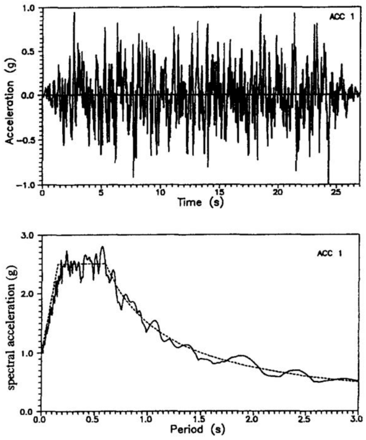

Figure 2.5: Artificial accelerations and spectral acceleration, (Calvi and Kingsley, 1996).

To conclude, recorded earthquakes are preferable and should be used for experimental research. For the validation of numerical models these same accelerations should than be used. To generate more results for a sensitivity analysis artifical accelerograms can be used. Harmonic and impulse vibrations can be used, however, the validity of these results is questionable since these are very different from realistic vibrations.

3
Unreinforced Masonry Behaviour

Masonry has a complex behaviour due to its orthotropic geometry and its material properties. When URM walls are loaded in a cyclic manner complex failure mechanisms can develop and unloading paths with recovery of stiffness occur which make the modelling of masonry a challenging task. In this chapter the behaviour of unreinforced masonry is discussed.

3.1 Orthotropic Geometry

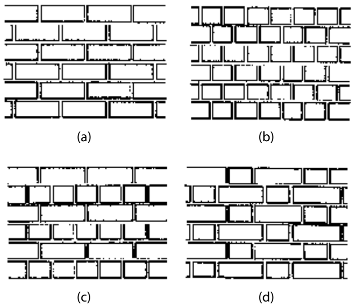

Figure 3.1: Fundamental rules of bonding patterns to avoid superimposed vertical joints, (Guillaud et al., 1995).

The stacking of masonry can be made in different ways. The number of wythes (bricks in the lateral direction of the wall) can vary as well as the length/width ratio of the bricks which determines the stacking. Some forms of stacking are depicted in Fig. 3.1 different patterns are shown of which (a) is one-wythe and (b), (c) and (d) are two-wythe patterns.

The vertical joints between the bricks are called the head joints and the horizontal joints are called the bed joints. Since bed joints form a continuous connection over the width of a wall and head joints are interrupted by bricks, the effective properties over a cross-section in the total wall in vertical direction is different from the horizontal direction.

3.2 Material properties

The material properties of the bricks and the mortar are different but comparable. Both behave as a brittle material in tension where a clear cracking point can be observed followed by exponential softening. In compression hardening behaviour is found after some initial crushing after which a parabolic softening relation is found. Typically the connection between the mortar and the bricks is the weakest link. This causes a typical stepped diagonal cracking pattern. The constitutive relation can be applied to the model in different ways according to the method used, more can be found in Chapter 7. Combined with the orthotropic geometry effective material properties in the two directions can be derived.

3.3 Global Failure Mechanisms

URM buildings loaded by earthquakes can fail in different ways depending on geometry, material and loading pattern factors. Bruneau (1994) gives a good summary of the possible global failure modes observed by researchers between 1984 and 1991. The out-of-plane failure is described in more detail since this is the main focus of this thesis.

FAILURE OR LACK OF ANCHORAGE. A good connection between floors or roof and URM walls is of great importance for earthquake resistance. Since normally these connections are only loaded in vertical direction or by wind loads the horizontal resistance due to friction may not be sufficient for earthquake loading. In cavity walls a good connection between the outer and inner wall is needed, if not the outer walls can behave as cantilever walls over the total height of the building. If anchorage is present, most of the time this is not designed specifically for earthquake resistance and failure can still occur. This can be rupture of the steel anchorage or failure of the wall around the connection point where high forces are introduced in the wall. The resulting failure is slip of the floor or roof from the wall, as depicted in Fig. 3.2, this may result in life threatening situations.

Figure 3.2: Failure of anchorage and slip of floor inside the building, (Bruneau, 1994).

Figure 3.3: In-plane cracking of pier due to shear stresses, (Bruneau, 1994).

IN-PLANE FAILURES. When walls are loaded in-plane by earthquakes shear cracking of the wall can occur. Diagonal cracks can occur, especially in piers where forces are brought down through a small high masonry element, see Fig. 3.3, . Other possible failure types are horizontal shear at the bottom or top of a pier resulting in slipping and toe-crushing of a pier resulting in excessive rotation. In-plane failure does not automatically lead to the global collapse of the structure.

Figure 3.4: Out-of-plane failure over two levels due to flexible floor, (Bruneau, 1994).

OUT-OF-PLANE FAILURE. Out-of-plane failure occurs when the wall bends in the lateral direction, which is the weakest direction due to its small thickness. A pattern of vertical, horizontal and diagonal cracks develops depending on boundary conditions and material properties.

When one-way bending is examined in the vertical direction cracks parallel to the bed joints will be found. These cracks are caused by the low tensile strength of the bond or the bricks. Micro-cracks in the material cause the softening effects observed in load-displacement curves. It is also possible that the wall fails due to unit crushing when high axial stresses are applied, this is discussed in more detail in Section 3.7. For one-way bending in the horizontal direction two failure modes can occur, a toothed or zigzag pattern over the joints and a straight crack through units and/or joints.

After cracking, the wall can be found in a phase of, what ABK (1984) called, "dynamic stability". Doherty (2000) described this phenomenon as rocking behaviour. He distinguished two semi-rigid bodies after cracking. The bodies can rotate from one extreme fibre to the other. The load on the wall exerts a negative moment around the rotation point at the bottom. The self-weight as well as the vertically applied force exert a positive moment around the point. As long as the negative moment does not push the work-line of the vertical forces over the point of rotation the system is stable and will not fail. Since the load is of a dynamic nature it will switch sign, thus it is not inevitable that the load will push the wall until it becomes unstable. So in the cracked phase a dynamic stable system can be found. As has already been discussed, the stability is dependent on the amount of deformation of the system. Thus this is a geometric non-linear problem.

When floors do not provide a sufficient constraint in lateral direction the height over which the wall can bend will be larger resulting in a lower resistance, such an effect can be observed in Fig.3.4. Out-of-plane behaviour results in a loss of load-bearing capacity and thus in the collapse of (part of) the building. These situations can be life threatening.

COMBINED IN-PLANE AND OUT-OF-PLANE EFFECTS. Earthquakes are not loads which impose only loads in in-plane or out-of-plane direction, but are bidirectional. This can result in combined failure modes where the wall is first weakened by in-plane shear cracks which reduce the out-of-plane bending resistance. Dolatshahi et al. (2014) showed with numerical analysis that the out-of-plane strength can be reduced by 60% due to in-plane damage.

3.4 *Local Failure Modes*

Global failure mechanisms are a result of local failure of the masonry. Masonry can fail in several ways due to its orthotropic nature. In Fig.3.5 from Lourenco and Rots (1997) the possible local failure modes are depicted, as follows:

(a) Joint tension cracking

(b) Joint slip

(c) Unit direction tension crack

(d) Unit diagonal tension crack

(e) Masonry crushing

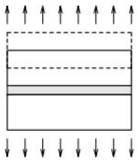
(a) Joint tension cracking

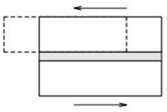
(b) Joint slip

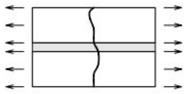
(c) Unit direction tension crack

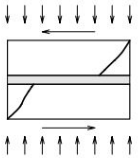
(d) Unit diagonal tension crack

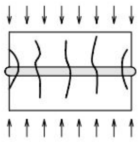
(e) Masonry crushing

Figure 3.5: Local failure modes of masonry, (Lourenco and Rots, 1997).

Local masonry failure also changes its properties. When cracks occur masonry cross-sectional area changes and so does the stiffness of the total wall. This changes the eigenfrequency of the wall and thus also the response to a dynamic load of a certain frequency. This was originally found by Bariola et al. (1990) from experimental research.

3.5 *Hysteresis*

The hysteresis effects can be observed from the way in which a masonry structure responds to cyclic loads. Hysteresis behaviour is the dependence of the output to the input as well as the history of the element. The result is degradation of sectional stiffness and strength due to plastic deformation in previous loading cycles. This can be observed from the stress-strain or load-displacement curves, as depicted in Fig.3.6. Some of the important characteristics in the behaviour of masonry, which can be found in hysteresis effects, are the reduced unloading stiffness and the recovery of stiffness due to the closing of cracks.

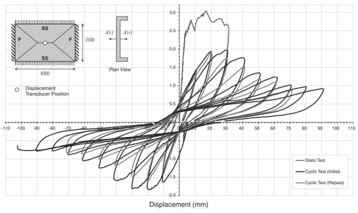

Figure 3.6: Load-displacement curve from experimental testing of a quasi-static cyclic loaded wall, from (Griffith et al., 2007).

Paulay and Priestly (1992) described the inelastic behaviour of a single degree of freedom system and the corresponding hysteresis relations. In Fig. 3.7 a few different possible hysteresis patterns are given. Curve (d) shows a resemblance with the results found by Griffith et al. (2007). According to Paulay and Priestly (1992) it is especially the area which is inside a loop that is of importance since this is equal to the amount of energy which is dissipated. In the ideal elastoplastic case this can be clearly observed. The area is purely created by the plastic strain, the horizontal line. Although the structure finds its original elastic deformation at the end of the loop, energy has been dissipated through plastic deformation in positive and negative directions. A correct unloading and reloading stiffness is required to correctly model the amount of dissipated energy.

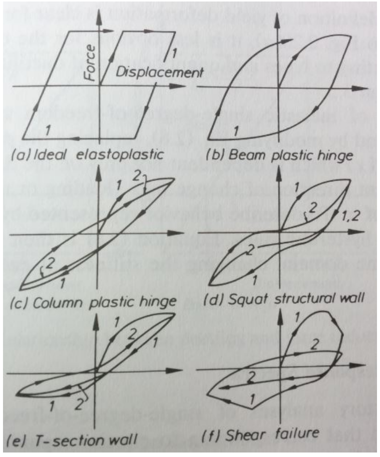

Figure 3.7: Hysteresis effects characteristics, from (Paulay and Priestly, 1992).

The unloading of URM walls loaded out-of-plane can have a different stiffness if cracks have already formed. When the wall is totally unloaded it is not unnecessary that for cracks to be closed, some plastic deformation may still be present. If one assumes that the stiffness is secant as is done in DIANA, it is therefore not correct, see Fig. 3.8.

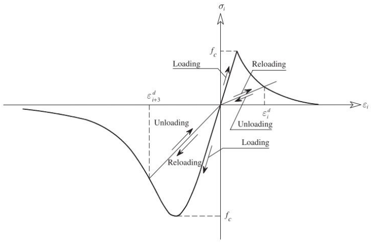

Figure 3.8: Constitutive relation with unloading and reloading behaviour as implemented in DIANA, from (Mendes and Lourenço, 2009).

The recovery of stiffness due to closing of the cracks is important for the reloading phase of cyclic loading. A tensile crack can if closed transfer compressive stresses. If in the tensile part of the reloaded cross-section, which was previously loaded in compression, no cracks are formed, than it has the same stiffness as the original cross-section.

The damage plasticity model of Lubliner et al. (1989), later adapted to three dimensions by Lee and Fenves (1998) takes these effects into account. In Fig. 3.9 a possible load path, as proposed by this model, can be found. First tension is applied and the linear regime is entered until cracking begins at a stress σ_{t0}. Then softening sets in until the point at which the unloading starts. The unloading stiffness is dependent on the amount of damage due to tension in the cross-section. When compression returns to the cross-section the stiffness is recovered and the section behaves as if it were uncracked.

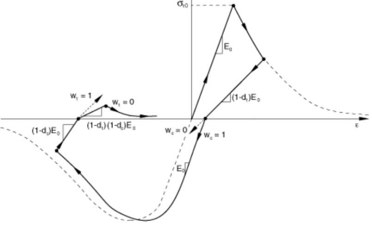

Figure 3.9: Stress-strain relation of masonry applied in Abaqus, from (Dassault Systèmes, 2013).

The compressive regime is different from the tensile regime and has no clear cracking point. First it is linear, then some crushing occurs but the stress continues to increasing. Finally softening gradually reduces the stress to zero with a lot of deformation. If unloading starts the stiffness is reduced due to the crushing damage. When the cycle is completed a new cycle resumes with tension, the stiffness is reduced due to both the tensile and the compressive damage.

3.6 *Directional response*

As briefly described in Section 3.3 earthquakes are bi-directional by nature, because the direction is never totally in-plane or out-of-plane. Dolatshahi et al. (2014) used discrete bricks combined with damage plasticity model to assess the behaviour of URM walls when subjected to pushover analysis from different angles to the wall.

One of the results of this study indicated that the displacements were not in the direction of the applied force but more in the in-plane direction. Since this direction is stiffer it takes more load than the out-of-plane direction.

It was also found that no cracks due to out-of-plane bending developed if the force was introduced at an angle smaller than 85° to the wall. This indicates that almost always combined behaviour is appropriate.

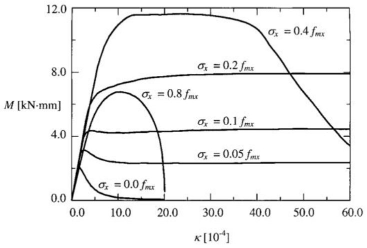

Figure 3.10: Moment-curvature diagrams different axial compression, from (Lourenço, 2000).

3.7 *Applied Overburden Force*

On a URM wall a vertical in-plane force can be applied. This could, for instance, be the self-weight of floors and walls, or variable loads applied to the floors. This force has an effect on the stresses in the wall, it is comparable to pre-compression. (Lourenço, 2000) investigated the effect of axial compression on the bending strength and found that initially the effect is positive, because a higher bending strength was found for moderate axial compression. However, this effect decreased for high compressive forces. Compressive stresses due to bending added to the axial stress then caused crushing. For the ductility the same effect was found, see Fig. 3.10.

Doherty (2000) describes the difference between high and low applied overburden in a qualitative way. A wall which has a low applied overburden stress will generally fail when the cross-section is cracked, since the semi-rigid resistance threshold in the post-cracked stage is lower than the elastic resistance, see Fig. 3.11. When a high overburden stress is applied the elastic resistance is lower than the semi-rigid resistance threshold and the wall has a reserve capacity to rock, as described in Section 3.3.

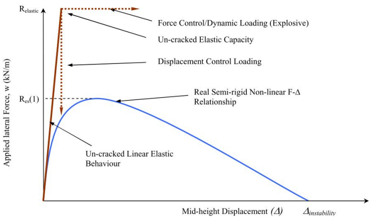

Figure 3.11: Force-displacement diagram for a wall with low applied overburden, from (Doherty, 2000).

3.8 Geometrical non-linear effects

When the wall deforms the applied overburden as wall as the workline of the self-weight changes. These effects are geometrical non-linear effects, since they are dependent on the geometry.

Doherty (2000) has examined this effect for one-way out-of-plane bending. When the wall deforms in the lateral direction it can (dependent on the boundary conditions) rotate around the edges of it's base and top support. This causes a shift in the workline of the self-weight and overburden. However, for as long as the deformation is not too big (the workline does not shift pass the point of rotation) these forces generate a stabilising moment. Therefore, it is possible that the wall has some extra resistance capacity after cracking. Doherty (2000) defines this as the semi-rigid resistance threshold.

4

Use of Masonry in Buildings

To model the behaviour of a URM wall or building in a representative way some knowledge of the building details is needed. Especially the connections are of importance since these determine how the boundary conditions should be modelled.

Doherty (2000) described some typical URM masonry connections which are common practise in Australia.

A PARTITION WALL can be found in Fig. 4.1. The wall is connected to the ceiling using timber or plaster cornices. Between the ceiling and the floor no vertical forces can be transferred. The timber pieces can keep the wall at it's place, it therefore acts as a horizontal support. The connection has no moment capacity and has some freedom to rotate thanks to the open space between the wall and the ceiling.

A CAVITY WALL can be constructed with the inner or the outer wall as load-bearing, Fig. 4.2 and 4.3. The non-load-bearing wall has less resistance due to the absence of an overburden force as described in Section 3.7. It is therefore connected to the load-bearing wall by anchors. These anchors should for a reliable connection and should be resistant against corrosion. If the anchors fail the non-load-bearing wall has little resistance against lateral loading and can easily 'peel off' of the load-bearing wall. This type of failure has been reported frequently after the Newcastle Earthquake, Australia. On top of the load-bearing wall a wooden plank or steel truss can be placed which is connected to the roof using nails or anchors and provide shear resistance. Uplift of the roof is resisted using anchors (see Fig. 4.3).

TYPICAL FLOOR CONNECTIONS are depicted in Fig. 4.4 and 4.5. A vertical component is placed to prevent the wall to translate in horizontal direction, however this component is not applied everywhere. Between the URM wall and the floor a Damp Proof Course (DPC) is added which prevents water damp from entering the wall. This has some friction resistance with the floor. Beyond the mortar the connection provides no extra moment resistance.

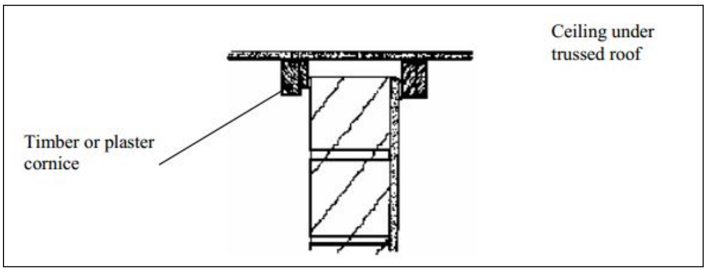

Figure 4.1: Internal partition wall ceiling connection detail

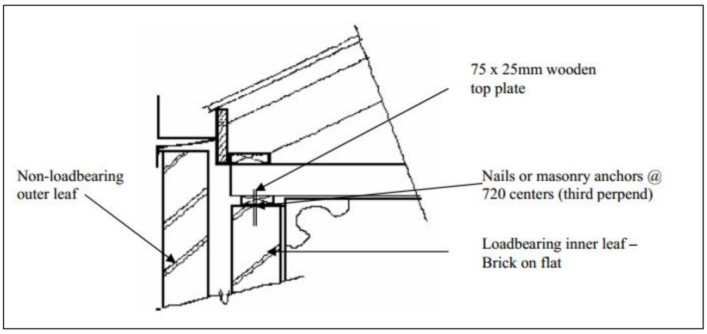

Figure 4.2: Cavity wall roof connection with inner wall as load-bearing

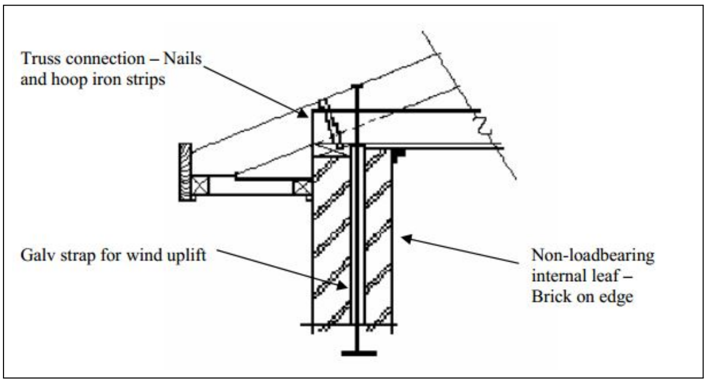

Figure 4.3: Cavity wall roof connection with outer wall as load-bearing

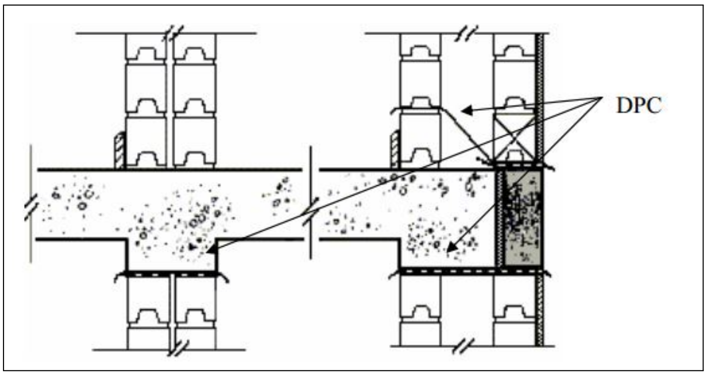

Figure 4.4: Connection wall with inter story floor

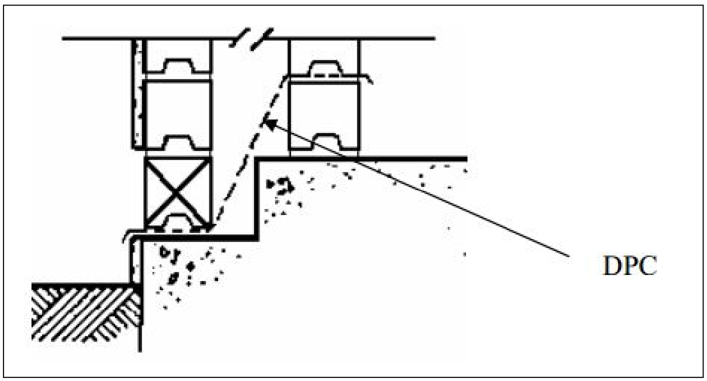

Figure 4.5: Connection wall with ground floor

5

Experimental Research

Unreinforced masonry is a very old building material. As such is has been used over the centuries and building guidelines developed by trial and error. When research was preformed on URM walls it was mostly statically loaded. Since quasi-static response can differ quite a bit from dynamic response also dynamic tests have been performed. The first being ABK (1984) which indeed proved the difference between quasi-static and dynamic loaded walls. Bariola et al. (1990) found that after cracking the stiffness of a wall degraded resulting in a different dynamic response. Main result of all the experimental studies is that dynamic loaded URM walls have a greater capacity than what is found from quasi-static experiments.

THE TWO TESTS that will be discussed in this chapter are test on one and two-way bending. Both are well documented and thus will serve good for experimental validation.

5.1 *Doherty tests, Dynamic One-way Bending*

The goal of the tests performed by Doherty (2000) is "physical understanding underlying one-way dynamic bending". Shaking table tests have been performed at the University of Adelaide. From this point these test will be referred to as the Doherty tests.

FOURTEEN URM WALLS are tested in this experimental program. Eleven had dimensions of 1500 x 110 mm (height x thickness) and three a thickness of 50 mm to get a more realistic slenderness ratio of 30. The width is not specified, but since one-way spanning walls are examined this is not relevant. The specific weight of both types of walls have been determined at 1800 and 2600 kg/m^3 respectively.

The bricks used have dimensions 230 x 110 x 76 mm (width x thickness x height) and have three holes with a diameter of 45 mm, see fig. 5.1. In the thinner walls bricks of 230 x 50 x 33 mm are used. The mortar used is made up of a mix 1:1:6 (cement : limestone : sand).

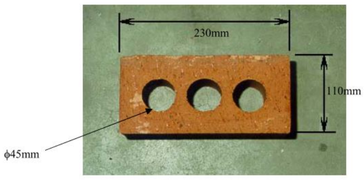

Figure 5.1: Dimensions of a standard brick in Doherty tests, from (Doherty, 2000).

THE MATERIAL PARAMETERS are determined from several two-brick, five-brick prisms and 100 x 100 x 100 mm cubes which were constructed during fabrication of the walls. From bond wrench and compressive tests the material parameters as presented in Table 5.1 are determined.

Material parameter	Symbol	Mean value (in MPa)	St. dev. (in MPa)
Flexural tensile strength masonry	$f_{m;t}$	0.49	0.15
Youngs modulus masonry (110 mm)	E_m	9,400	5,322
Youngs modulus masonry (50 mm)	E_m	8,250	2,192
Compressive strength masonry (110 mm)	$f_{m;c}$	13.4	1.64
Compressive strength masonry (50 mm)	$f_{m;c}$	26.5	0.28
Compressive strength mortar	$f_{mor;c}$	5.17	-

Table 5.1: Material properties of Doherty tests, (Doherty, 2000)

USING A SHAKING TABLE accelerations are imposed at the base of the wall. A steel frame was made to mimic the effect of the shear walls and floors and their dynamic filtering effect, as explained in Section 2.3. This results in an in-phase excitation at the top and the bottom of the URM wall.

THE WALL IS SIMPLY SUPPORTED at both top and bottom. In Fig. 5.2 the top support in sketched. It can be seen that the two steel angles with small rubber strips indeed allow rotation and small vertical displacements but prevent significant horizontal displacements.

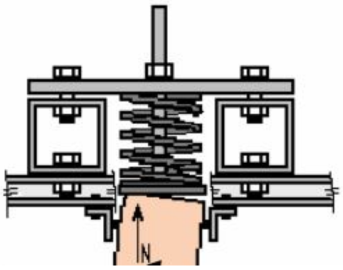

Figure 5.2: Top support with axial force imposed by springs, (Doherty, 2000).

THE AXIAL FORCE AT THE TOP of the wall is applied with six springs. Since the top can rotate a small vertical displacement can also occur.

This causes an increase in the force in the spring. Doherty (2000) explains that a significant increase in the vertical imposed force is overcome by selecting springs accordingly. This can mean two things, either springs with a non-linear force-displacement relationship have been selected or the increase of force per mm is very small. For the 50 mm wall this indeed resulted in a acceptable change of the vertical force of ± 5%. For the 110 mm wall the vertical elevation is bigger and so is the vertical force, which makes the increase only acceptable up to 20% displacement at mid-height of the wall.

As can be seen in Fig. 5.2 with rotation the vertical force also is shifting towards the compressive part of the cross-section. This is in line with the real situation.

MEASUREMENTS are recorded using acceleration and displacement instruments. These are placed at specific points on the test rig, see Fig. 5.3. LVD and LVDT are instruments to measure displacements, ACCEL instruments measure accelerations.

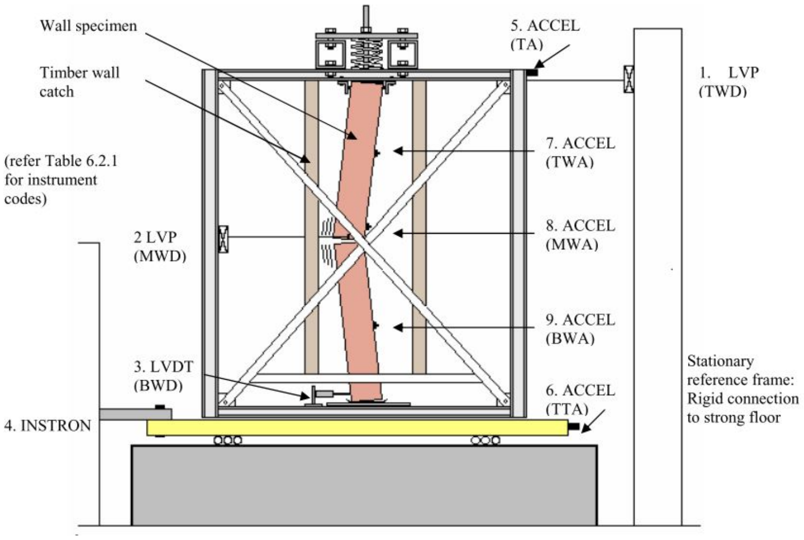

Figure 5.3: Test rig Doherty tests with instrumentation, (Doherty, 2000).

HARMONIC, PULSE AND TRANSIENT excitations are performed to find physical and dynamic behaviour of the URM walls. Also static pushover and free vibration tests are undertaken for more data on the walls, as well as to compare the results with other experimental data. The results are presented in tables and figures by Doherty (2000).

ARUP analysed the results of Doherty and concluded from the Nahanni earthquake data that the acceleration are inconsistent with the displacements and therefore cannot be used. (This is checked in the main part of this master's thesis and found to be wrong.)

In Fig. 5.4 results for specimen 12 with 66% El Centro excitations are presented. These results seem most reliable and should be modelled first.

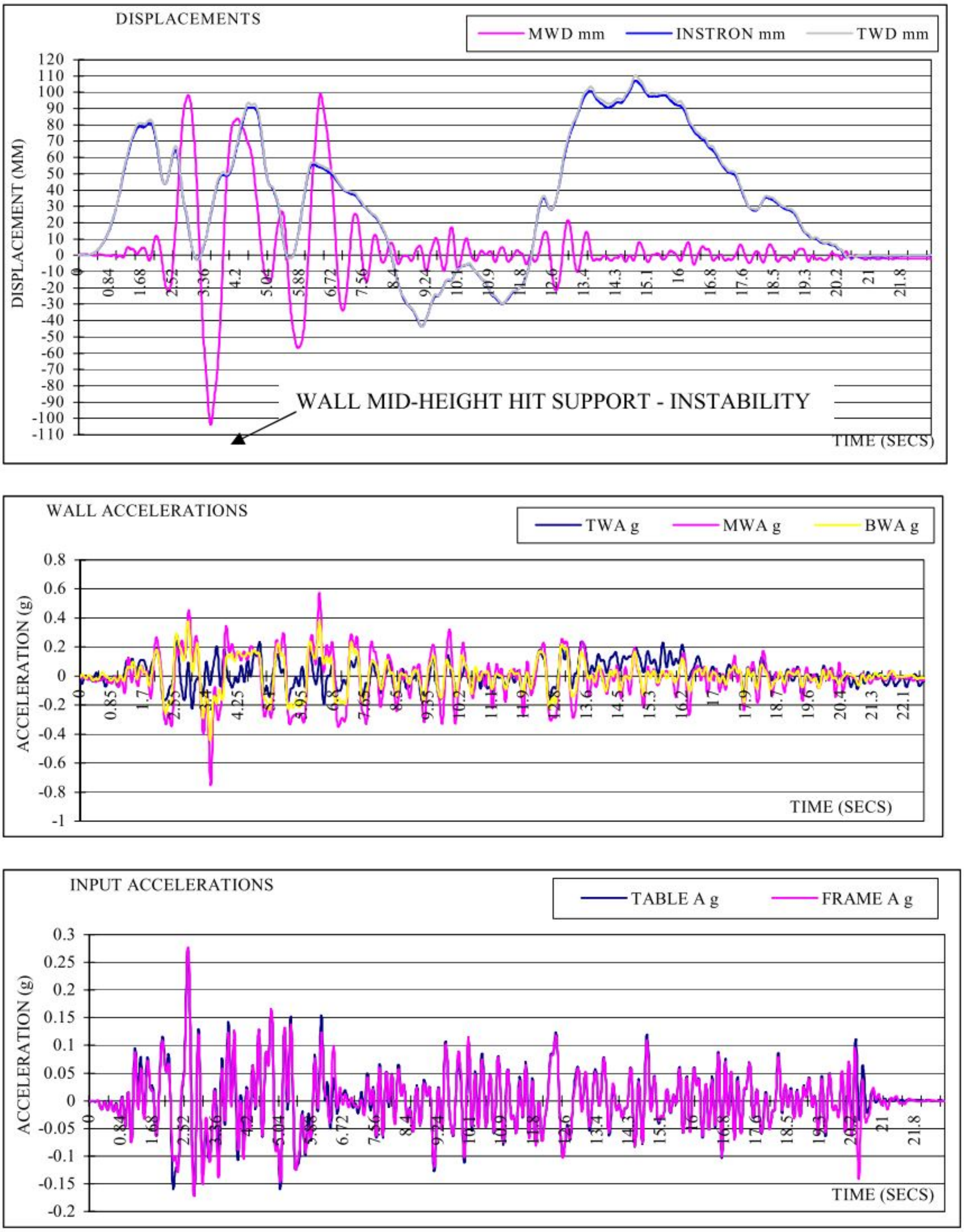

Figure 5.4: Results of transient excitation test - 66% El Centro, (Doherty, 2000).

5.2 *Griffith tests, Quasi-static Two-way Bending*

The Griffith tests aim to "provide a basis for the development of a non-linear inelastic hysteresis model for masonry in two-way bending" and are well presented by Griffith et al. (2007).

Eight unreinforced masonry walls were subjected to cyclic static face loads. The walls were supported at all edges, this way the walls bend in both horizontal and vertical direction, which is a representation of a wall in a building supported by two shear walls and a top floor. The walls are full scale and have different dimensions with window openings.

The bricks used have dimensions 230 x 110 x 76 mm (width x thickness x height) and have ten small holes, see Fig. 5.5. The mortar used is made up of a mix 1:2:9 (cement : limestone : sand).

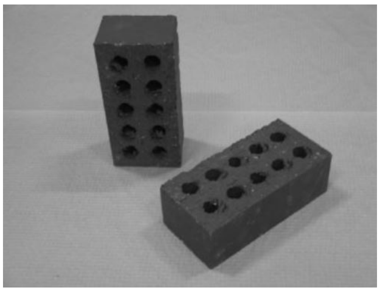

Figure 5.5: Dimensions of a standard brick in Griffith tests, from (Griffith et al., 2007).

The material parameters are determined from small-scale masonry specimen and are presented in Table 5.2.

Table 5.2: Material properties of Griffith tests, (Doherty, 2000)

Material parameter	Symbol	Mean value (in MPa)	CoV
Lateral modulus of rupture brick	$f_{b;ut}$	3.55	0.27
Youngs modulus brick	$E_{b;m}$	52,700	0.35
Flexural tensile strength masonry	$f_{m;t}$	0.614	0.19
Youngs modulus masonry	E_m	3,540	0.41
Compressive strength masonry	$f_{m;c}$	16.0	0.14

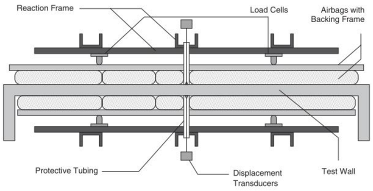

Figure 5.6: Test rig Griffith tests with instrumentation, from (Griffith et al., 2007).

Using airbags a face pressure is imposed over the full area of the wall. The airbags are placed on both sides to simulate the cyclic loading through inflation and deflation.

Most walls are supported with a simple support at both top and bottom and with fixed support on the sides. The simple supports are constructed of steel angles to make rotation possible. Less attention is paid to the influence of the vertical applied force during big rotations. At the bottom steel members provide lateral support. The sides are fixated by two shear walls which give not a rigid moment support but moments can be transferred.

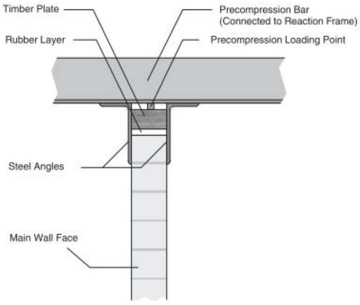

Figure 5.7: Top support Griffith Tests, from (Griffith et al., 2007).

Measurements are recorded using one displacement tool which is most of the time located at the middle of the wall. Since at the position of the instrument no load can be applied, less measurements give more realistic results.

Cyclic static loads with an increasing character have been applied after an initial static strength test was applied. This static test displaced the wall until 20 to 30 mm, which was enough to form a failure mechanism. The load application is displacement based. Two different patterns are applied to see if one gives a better insight into the hysteresis effects than the other.

GRIFFITH ET AL. (2007) REPORT clear plots of the load-displacement curves for all eight walls. Clear big hysteresis loops are found which indicates a high dissipation of energy. Griffith et al. (2007) also report that from these loops the equivalent viscous damping ratios were derived and found to be between 13 and 18%.

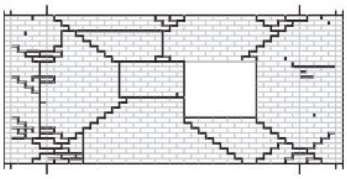

Figure 5.8: Crack pattern wall 5 (outside face), from (Griffith et al., 2007).

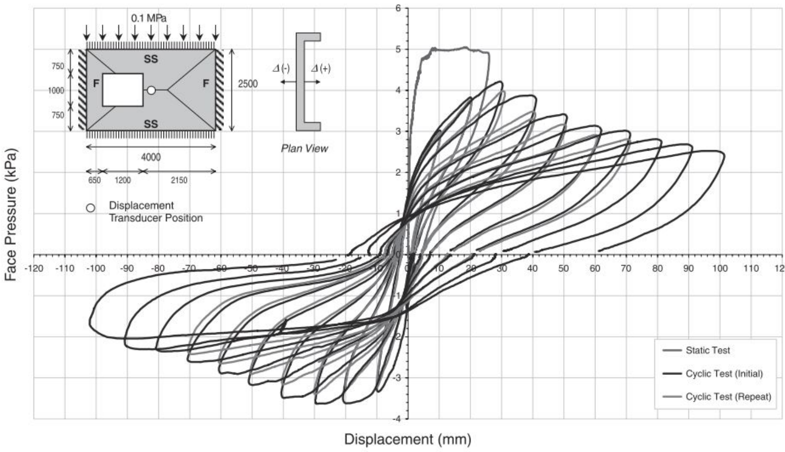

Figure 5.9: Results of quasi-static cyclic load test wall 3, (Griffith et al., 2007).

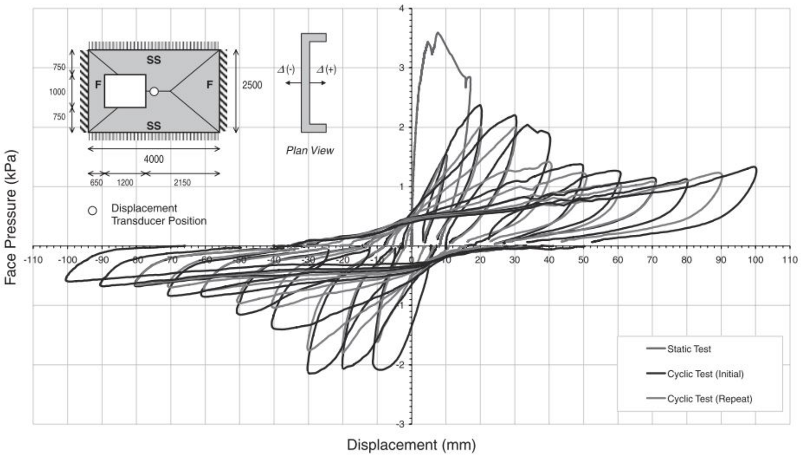

Figure 5.10: Results of quasi-static cyclic load test wall 5, (Griffith et al., 2007).

6
Time-integration

6.1 Equations of Motion

A problem is defined by the equations of motion which can be derived as explained in Section 7.4.

$$\mathbf{M}\,\ddot{\mathbf{q}} + \mathbf{C}\,\dot{\mathbf{q}} + \mathbf{K}\,\mathbf{q} = \mathbf{f}(t) \tag{6.1}$$

This system of equations can be solved using an explicit or an implicit time integration method. Most methods first rewrite the second order differential equations into a set of first order differential equations. This is the most robust method since any higher order problem can be reduced to a first order problem and solved by simple time-integration methods.

6.2 Explicit integration

In explicit methods the solution of the next time step is only a function of the previous time steps. To find the solution at the next time step an algebraic function needs to be solved. An example of such a method is the Forward Euler method.

$$w_{n+1} = w_n + (t_{n+1} - t_n)\; f(w_n, t_n) \tag{6.2}$$

Where the function f is the derivative of y, and w is the approximation of y. Other examples of explicit methods are Modified Euler, Runge-Kutta and Central Difference method. The latter is implemented in the LS Dyna software which is used by ARUP.

6.3 Implicit integration

In implicit methods the solution of the next time step is also a function of the next time step. To find the solution a system of equations needs to be solved. This requires more computations then solving an algebraic function. However, implicit methods have a better numerical stability, which makes it possible to choose from a big time steps and still obtain a convergent result. An example of such a method is the Backward Euler method.

$$w_{n+1} = w_n + (t_{n+1} - t_n)\; f(w_{n+1}, t_{n+1}) \tag{6.3}$$

Other examples of implicit methods are the Trapezium method, the Newmark method and the Hilber-Hughes-Taylor method, which is a special version of the Newmark method and is implemented in DIANA.

For both methods it is possible to find the global and local error as well as the convergence criteria. This determines if a numerical solution method is stable, in other words converges to the real solution.

7

Methods for Structural Analysis

An unreinforced masonry wall can be analysed with quite some different analytical and numerical methods. Generally, the numerical methods can be split in two types, micro and macromodelling. Micromodelling is looking at the individual components and really trying to model the physical properties. Macromodelling is looking from a more phenomenological point of view were the behaviour of the masonry as a whole is attempted to be modelled.

In this chapter, six methods are examined which can be of used for the modelling of unreinforced masonry walls loaded out-of-plane. At the end of the chapter the methods are compared.

The methods discussed in this chapter are:

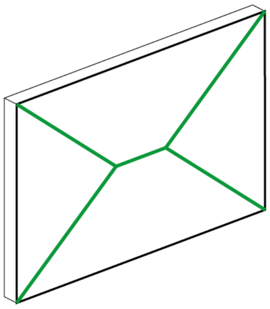
Yield Line Theory

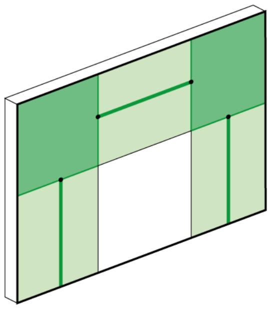
Equivalent Frame Method

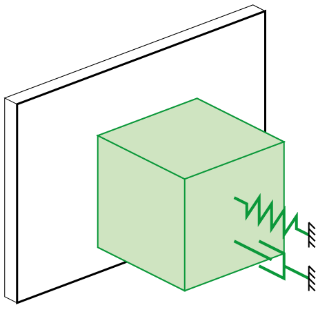
Linearised Displacement Based Analysis

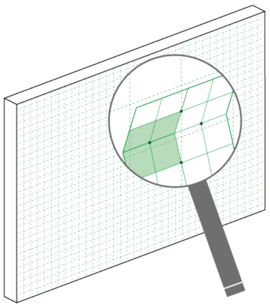
Rigid Elements Method

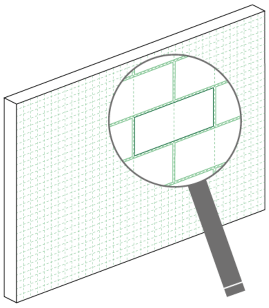
Multisurface Interface Model

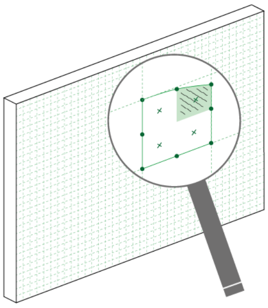
Anisotropic Continuum Model

7.1 *Yield Line Theory*

The yield line theory is an analytical method to determine the upper-bound ultimate resistance of, in this case, a masonry wall loaded out-of-plane. An important assumption for the validity of this model is the ductility needed to let a yield pattern develop. This model has originally been proposed by Losberg and Johansson (1969). The method explanation and the prove of ductility explained below are obtained from Brinker (1984).

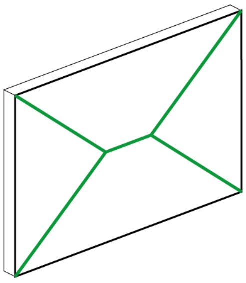

Figure 7.1: Visualisation of Yield Line Theory

BRINKER (1984) EXPERIMENTALLY STUDIED the stress-strain relationship and moment capacity of horizontal and oblique yield lines for different material combination. A pattern of horizontal and oblique yield lines can be found in Fig. 7.2. It was assumped that the masonry had no tensile strength. The plastic behavior shown in Fig. 7.3 clearly shows that masonry has enough ductility to use the yield line theory.

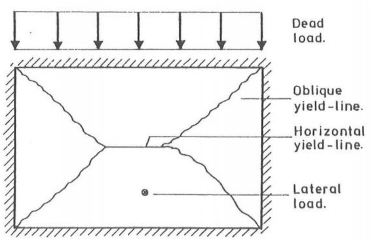

Figure 7.2: Laterally loaded masonry wall with oblique and horinzontal yield-lines, (Brinker, 1984)

THE MOMENT CAPACITY of yield lines determine the ultimate lateral load on the masonry. The horizontal and oblique yield lines are treated separate, for the oblique lines a further distinction is made between bending and torsion. For bending over the horizontal and oblique yield lines, no material dependency was found. The moment capacity can be calculated using the following formula's for horizontal and oblique lines respectively.

$$M = \mu_0 K \qquad M_1 = \mu_1 K_2 \tag{7.1}$$

Where μ are friction parameters and K are the axial loads applied. For the torsion moment over the oblique yield lines the cohesion is of significant influence and so the moment can be found as,

$$M_2 = c + \mu_2 K_2 \tag{7.2}$$

The friction parameter for bending is not dependent on material parameters, for torsion it is.

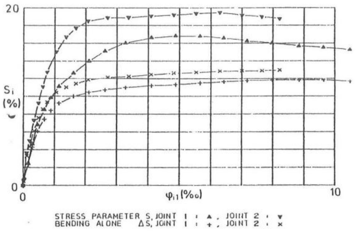

Figure 7.3: Stress-strain relationship s_1^*, ϕ_{11} and s_2^*, ϕ_{21} together with contributions from bending alone, (Brinker, 1984)

TO CONCLUDE Brinker (1984) acknowledges that this method is more of a qualitative use than of a quantitative use. However the ductile behaviour proves that is is allowed to use the yield line theory to find an upper-bound value of the moment capacity.

7.2 *Linearised Displacement Based Analysis*

Force-based calculations used in practise underestimate the capacity of URM walls, which do have ductile capacity. Goal of this analysis method is to develop a linearised substitute structure which is able to mimic the non-linear behaviour of the URM wall and thus provide a quick way to account for the ductility. From the substitute-structure method originally proposed by Shibata and Sozen (1976), Doherty et al. (2002) proposed a simplified method to find the parameters of an appropriate substitute-structure from a tri-linear force-displacement relation.

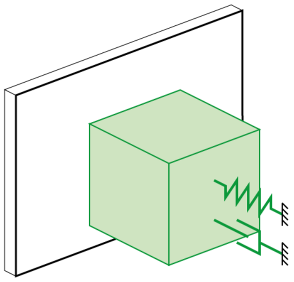

Figure 7.4: Visualisation of Linearised Displacement Based Analysis

STARTING WITH A RIGID BLOCK ASSUMPTION the force-displacement relation can be derived. Two stages are examined, the moment at which a mechanism is formed and the moment of instability. For the situation where the wall is simply supported, as pictured in Fig. 7.5. From these stages the force-displacement relation can be obtained, see Fig. 7.6.

From this relation the tangential stiffness can be found as well as the average secant stiffness over a loading cycle. From experimental Gaussian pulse tests the average secant stiffness is found to be a good approximation for the average stiffness of the wall. With this approximate stiffness, the natural frequency can be determined.

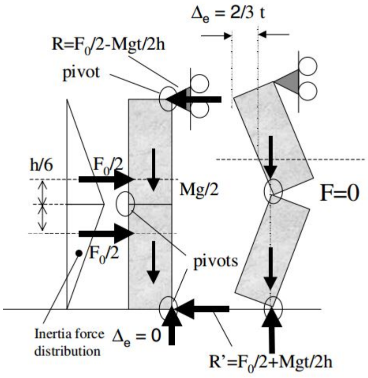

Figure 7.5: Inertia forces and reactions on rigid URM walls. Simply-supported wall at incipient rocking and point of instability, (Doherty et al., 2002)

IF DEFORMABLE BLOCKS are assumed, a more realistic model is obtained. The consequences of this deformability leads to a bending (displacement) of the wall before cracking and a smeared rotation area, instead of a infinitely thin rotation line. This results in a smooth force-displacement relationship, given in Fig. 7.6, which can be approximated with a tri-linear relationship. Like with the rigid blocks, the average secant stiffness can be used as an approximation for the average stiffness and with it the natural frequency can be found.

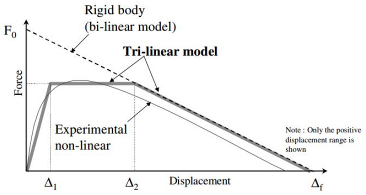

Figure 7.6: Force-displacement relationship of deformable URM walls, (Doherty et al., 2002)

A SUBSTITUTE-STRUCTURE IS COMPOSED to mimic the non-linear behaviour of the original wall. A good approximation is found when the same ultimate displacement is found for the same imposed accelerations. To reach this effect the constant stiffness of the linearised substitute-structure is set equal to the average stiffness of the tri-linear force-displacement relation and the ultimate displacement is defined as the displacement for which the wall becomes unstable.

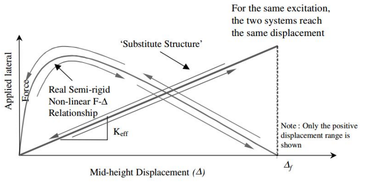

[2em]

Figure 7.7: Characteristic linear substitute-structure stiffness for displacement analysis, (Doherty et al., 2002)

TO VERIFY THE MODEL numerical analyses are performed with a non-linear time history method (THA), a quasi-static method (QS) and the linearised displacement based method (DB). Although the variation between THA and DB can be 50% it out performs the force based QS method, which can have an error an even bigger error especially for high frequencies.

7.3 *Equivalent Frame Method*

The equivalent frame method is developed with the objective to reduce the computational costs and complexity but still obtain accurate and applicable results. The method uses one dimensional elements to describe a system of piers and spandrels of which a wall is build up, see Fig. 7.9.

THE FINITE ELEMENT IMPLEMENTATION is explained in detail by Roca et al. (2005). In this approach Timoshenko beam elements are used with two nodes, each six degrees of freedom. Explained is how the initial stress state and the applied forces over the beam contribute to the stress vector at a certain cross-section. Through a stiffness matrix these stresses are related to the strains which determine the deformation of the beam and finally the displacement of the end node.

A Timoshenko beam element is used to realistically model the deformation of wide, low walls where the deformation is primarily governed by shear.

Three numerical simulations, of which one pictures in Fig. 7.10, are performed to show the accuracy and applicability of the frame equivalent method. From the three tests it can be concluded that the method is able to predict the global failure modes in a good and accurate way. It can also predict the ultimate capacity of the model although this is less accurate.

THE TREMURI PROGRAM implementation of this method explained by Lagomarsino et al. (2013) shows an even further simplification. In this program the number of degrees of freedom per node is reduced to three, two displacements and one rotation in-plane, see Fig. 7.11. This means that the model can only be used for in-plane simulations. It is assumed that local out-of-plane failure is prevented by following conservative design rules given by codes, such as good connections and minimal slenderness ratios.

This reduces the applicability of the program for a lot of existing structures since these are not designed by these design rules. Especially for out-of-plane failure which starts local but can have significant impact on the global structure.

THE ACCURACY of the equivalent frame method is found to be sufficient in situations where local failure mechanisms are prevented. The method is able to correctly predict the global failure mechanism. Lagomarsino et al. (2013) reports from a validation with an experiment that the accuracy is high in the linear regime but the method overestimates the resistance by approximately 20% in this case.

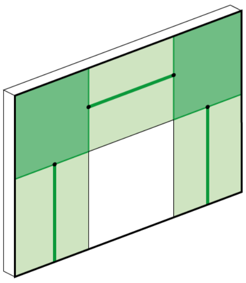

Figure 7.8: Visualisation of Equivalent Frame Method

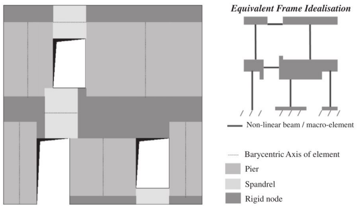

Figure 7.9: Idealisation from facade components to 1D elements, (Lagomarsino et al., 2013)

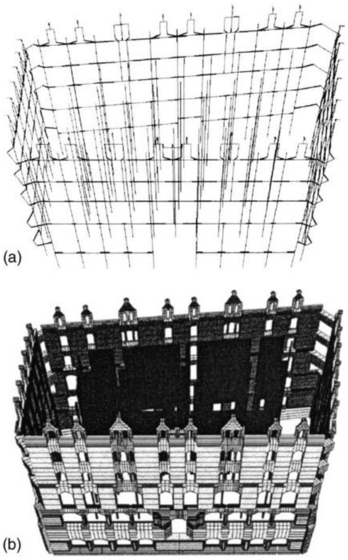

Figure 7.10: Example of a full building modelled with 1D elements, (Roca et al., 2005)

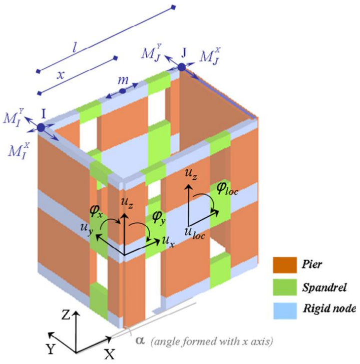

Figure 7.11: Simplification of TREMURI implementation, (Lagomarsino et al., 2013)

7.4 *Rigid Element Method*

Casolo (2000) has developed a model suitable for dynamic analysis specifically for walls which are governed by out-of-plane behaviour. The goal of this model is to reduce the number of degrees of freedom for investigating the effects of varying certain structural parameters. Since out-of-plane behaviour is governed by stiffness and strength degradation these effects are described in an orthotropic constitutive model.

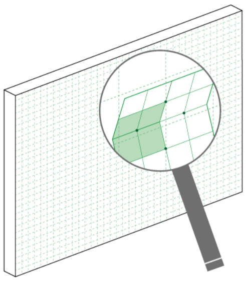

Figure 7.12: Visualisation of Rigid Element Methods

RIGID QUADRILATERAL ELEMENTS are used to describe a wall. These elements are connected using spherical hinges at the mid-side nodes of the quadrilateral elements. These hinges are subjected to bending and twisting between the two elements, see Fig. 7.13. The elastic and plastic behaviour are defined by a moment-curvature relation which is enforced in the hinges.

The deformation of each elements can be described using three parameters with which the lateral displacement of the element is defined. When the internal compatibility and external constraint equations are applied the total number of degrees of freedom reduces to less than the number of elements.

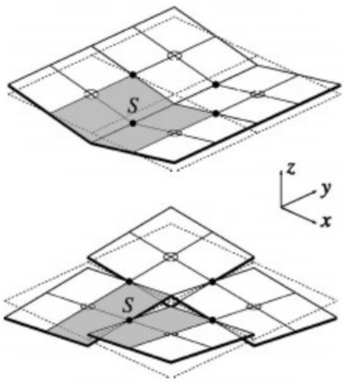

Figure 7.13: Discretization with four square elements subjected to pure flexural bending (top), and pure twisting (bottom), (Casolo, 2000)

THE CONSITITUTIVE RELATIONS are obtained from the masonry behaviour as explained in Chapter 3, with the hysteresis effects as explained in Section 3.5. Since rotation springs are used between the elements, the relation has the form of a moment-curvature diagram. The bending moment out-of-plane has an equal behaviour in both positive and negative direction, see dotted line (skeleton) in Fig. 7.14. Until the points E^- and E^+ the behaviour of the joint will be linear, after this cracks form and the skeleton of the curve will be followed until unloading sets in. The unloading is derived as a function of the maximal and minimal displacements, and a constant. Using smart algorithms, this relationship is completely enforced and the hysteresis behaviour is successfully modelled.

The absolute value of the points in this relationship are dependent on the orientation of the joint (head or bed joint) and the direction of the moment (twisting or bending).

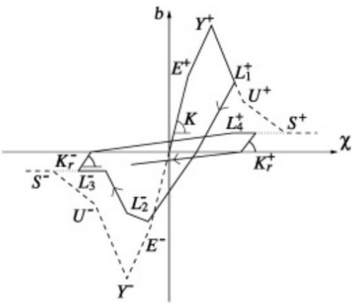

Figure 7.14: Hysteresis behaviour of the connection joint, (Casolo, 2000)

THE DYNAMIC LOADING is modelled using the Euler-Lagrange equations of the problem. These are composed by means of the first variation of virtual work.

Both the degrees of freedom $\ddot{q}$ as well as the imposed accelerations due to the earthquake $\ddot{g}$ affect the inertia of the structure. The first variation of the kinetic energy equals (Casolo, 2000),

$$\partial\mathcal{T} = -(\mathbf{M}\,\ddot{\mathbf{q}} + \mathbf{G}\,\ddot{\mathbf{g}})^T\,\partial\mathbf{q} \tag{7.3}$$

The constitutive relations are captured using the stiffness matrix which is dependent on the history of the curvature as well as the maximum sectional moment as previously described. Possible initial moments between the nodes are also considered. The first variation of the potential elastic energy equals, (Casolo, 2000),

$$\partial \mathcal{V}_e = -(\mathbf{f}^0 + \mathbf{K}\,\Delta\mathbf{q})^T\,\partial\mathbf{q} \tag{7.4}$$

Damping is considered to account for the effects of energy dissipation. A constant viscous damping is assumed which is proportional to the generalized mass matrix $\mathbf{C} = a_0\,\mathbf{M}$. This is a form of Rayleigh Damping with a zero parameter for the proportionality to the generalized stiffness matrix. The first variation of the potential damping energy equals,

$$\partial \mathcal{V}_d = -(\mathbf{C}\,\dot{\mathbf{q}})^T\,\partial\mathbf{q} \tag{7.5}$$

Equations 7.3-7.5 are assembled, resulting in,

$$\mathbf{M}\,\ddot{\mathbf{q}} + \mathbf{C}\,\dot{\mathbf{q}} + \mathbf{K}\,\Delta\mathbf{q} + \mathbf{f}^0 = -\mathbf{G}\,\ddot{\mathbf{g}} \tag{7.6}$$

With this system of equations expressed in the generalized degrees of freedom the problem is defined. The implicit method of Newmark is used to solve the system of equations over time. Newton-Raphson iterations are applied to solve the system at every time step.

The assembly of the Euler-Lagrange equations is not specific for this method and is applied on other methods as well.

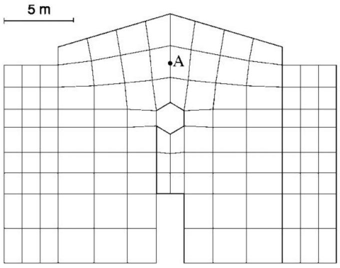

Figure 7.15: Rigid element discretization of Church of Transfiguration, Moggio del Friuli, Italy; 114 elements; position of point A, (Casolo, 2000).

A NUMERICAL VERIFICATION of the rigid element method compared with a finite element method on the front faÃğade of a damaged church is performed. The front faÃğade is modelled using 114 rigid elements, Fig. 7.15 shows the discretization. The finite element model uses 1010 elements. The resulting displacement of point A on the faÃğade are presented in Fig. 7.16. This clearly shows a very good resemblance. Therefore it can be concluded that the model is suitable for investigation of parameter influences.

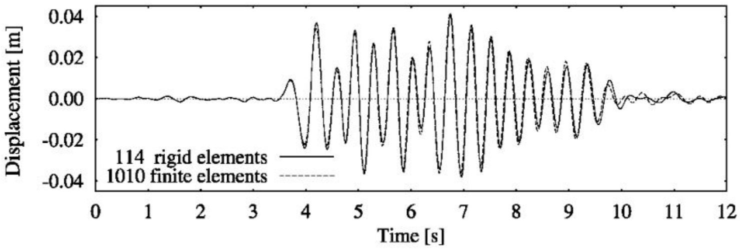

Figure 7.16: Comparison of the linear elastic response of the rigid element model versus the finite element model. The displacements are evaluated at point A of Figure 8, (Casolo, 2000).

7.5 *Multisurface Interface Model*

Another variant of micromodelling is the Multisurface Interface Model developed by Lourenco and Rots (1997). In this method all the plastic deformation occurs in interface elements which are placed between and within the bricks, see Fig. 7.18. In this way, the numerical model is simplified and behaves more robust, which makes it possible to follow the load path after cracking.

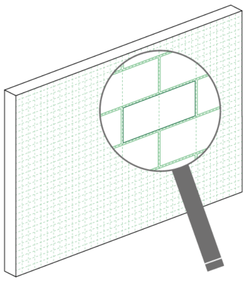

Figure 7.17: Visualisation of Multisurface Interface Model

THE INTERFACE ELEMENTS are placed between the bricks and have zero thickness. They mimic the mortar behaviour and the mortar brick interaction and therefore, must be able to fail in tension, shear or compression, failure modes (a), (b) and (e) of Fig. 3.5. With a two-dimensional Mohr-Coulomb stress criterion with an additional compression cap this is possible.

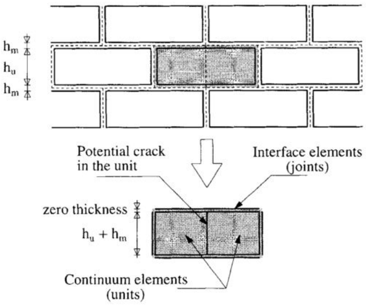

Figure 7.18: Discrete modelling of masonry. Bricks as elastic elements and mortar and potential brick crack lines as interface elements, (Lourenco and Rots, 1997).

This "Interface Cap Model" is presented in Fig. 7.19. As can be seen from the diagram hardening and softening is possible. Using return mapping algorithms (backward Euler) the stress at an interface can be determined and if needed brought back to the yield surface. If the stress is on the yield surface the interface element yields and the strain increases.

The softening stress strain relations for the shear and tension modes are according to Van der Pluijm (1997)'s experiments. For both modes a yield criterion is defined as well as a softening law. Both modes are coupled for the post peak regime, if softening sets in in one of the modes, the other mode softens with the same proportion.

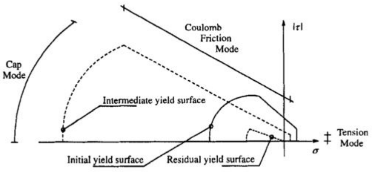

Figure 7.19: Interface Cap Model, (Lourenco and Rots, 1997).

THE VALIDATION OF EXPERIMENTS with the Interface Cap Model for in-plane URM walls show that these a in good agreement for ultimate strength and behaviour. Lourenco and Rots (1997) also report a very good convergence both globally and for the return mapping to the yield surface.

OUT-OF-PLANE MODELLING is possible with the help of this method if the stress over the thickness of the lateral direction can be computed using shell elements and seven-point Simpson integration or with help of three-dimensional elements.

A THREE-DIMENSIONAL interface model has been developed by Aref and Dolatshahi (2013) to attain a better understanding of masonry behaviour under cyclic loads. Lourenco and Rots (1997)'s cap yield surface is not applied since in experimental research it has been found that due to its limited thickness the mortar has high confining stresses and the mortar is therefore not damaged.

A STIFFNESS DEGRADATION model is applied by Aref and Dolatshahi (2013) where the relation between the plastic and the elastic strain is kept constant.

7.6 *Anisotropic Continuum Model*

Lourenço (2000) also proposed a continuous way to model masonry structures. The Anisotropic Continuum Model tries to find a compromise between simplicity (of the material properties and the degrees of freedom) and accuracy. This is possible since, in practise, the interaction between bricks and mortar modelled in the Multisurface Interface Modelling approach is not needed to make an engineering judgement about the behaviour of the masonry structure as a whole. Therefore the Anisotropic Continuum Model combines the material and geometrical properties of the mortar and bricks into effective material parameters. The effective material properties of the masonry wall are dependent on the masonry orientation (Sec. 3.1) and the material properties (Sec. 3.2).

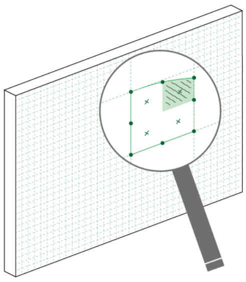

Figure 7.20: Visualisation of Anisotropic Continuum Model

A SMEARED CRACKING APPROACH is applied in this model to simplify the numerical implementation. This means that a crack (or crushing) is smeared out as if it were a plastic strain a over part of the element. On the integration points in the element the stress is computed. If the stress state at the integration point exceeds the yield criterion obtained from the constitutive relationship part of the element belonging to that integration point is considered to be cracked. The crack opening is then smeared out over the element as a plastic strain. The orientation of the crack is in the direction normal to the principal stress. An element with a cracked integration point is depicted in Fig. 7.21.

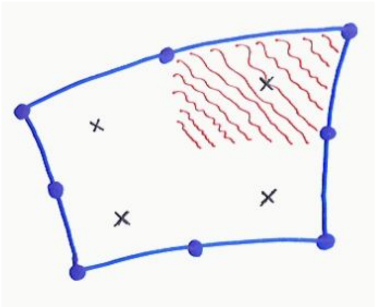

Figure 7.21: Cracked elements, from course CIE5148 (Hendriks and Rots 2012).

LOURENÇO ET AL. (1997) developed this model for plane stress elements in which the assumption is made in which $\sigma_z = 0$, where z is the thickness direction of the wall. For these elements the strain and strain vectors are,

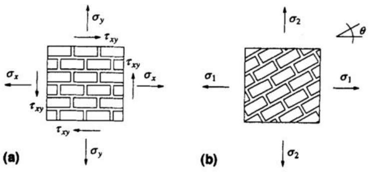

Figure 7.22: Orientation of the stress state dependent on the masonry orientation, from (Lourenço et al., 1998).

$$\sigma = \left[\sigma_x, \sigma_y, \sigma_z, \tau_{xy}, \tau_{yz}, \tau_{xz}\right]^T \tag{7.7}$$

$$\varepsilon = \left[\varepsilon_x, \varepsilon_y, \varepsilon_z, \gamma_{xy}, \gamma_{yz}, \gamma_{xz}\right]^T \tag{7.8}$$

Since the orientation of the masonry is of importance, the stress components are orientated along the primary axes of the masonry, see Fig. 7.22.

The elements can have different layers over the thickness in which the stress situation is examined. These layers are created using seven-point Simpson integration. This is especially important for out-of-plane bending in which the stress distribution over the element determines the moment capacity of the wall. In the layers the multi-axial stress state is considered. Two yield criteria are enforced to model the behaviour of URM masonry. For tension a Rankine-type criterion and for compression a Hill-type criterion. These criteria are derived from the originals to make them dependent on the effective material parameters in the two orthogonal directions along the material orientation.

THE RANKINE-TYPE CRITERION describes the yield criterion for the tensile behaviour. Assumed is that the cracks are only normal to the middle layer. This means that the shear stresses in the thickness direction are not used. Diagonal cracks are not possible, but stepped crack patterns are. After cracking an exponential softening law is applied for both masonry orientations with independent fracture energies. The criterion reads,

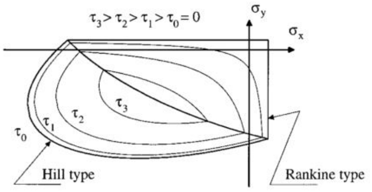

Figure 7.23: Composite yield criterion with iso-shear stress lines, from (Lourenço, 2000).

$$f_1 = \frac{(\sigma_x - \bar{\sigma}_{tx}(\kappa_t)) + (\sigma_y - \bar{\sigma}_{ty}(\kappa_t))}{2} + \sqrt{\left(\frac{(\sigma_x - \bar{\sigma}_{tx}(\kappa_t)) + (\sigma_y - \bar{\sigma}_{ty}(\kappa_t))}{2}\right)^2 + \frac{f_{tx} f_{ty}}{\tau_{u,t}^2}\,\tau_{xy}^2} = 0 \quad (7.9)$$

$$\bar{\sigma}_{tx}(\kappa_t) = f_{tx}\, e^{\left(-\frac{h f_{tx}}{G_{ftx}}\kappa_t\right)} \quad (7.10)$$

$$\bar{\sigma}_{ty}(\kappa_t) = f_{ty}\, e^{\left(-\frac{h f_{ty}}{G_{fty}}\kappa_t\right)} \quad (7.11)$$

where,

$\bar{\sigma}_{tx}(\kappa_t), \bar{\sigma}_{ty}(\kappa_t)$ = yield values
f_{tx}, f_{ty} = uni-axial tensile strengths
$\tau_{u,t}$ = pure shear strength in tension
h = standard equivalent length of elements
G_{ftx}, G_{fty} = fracture energies
κ_t = softening factor

THE HILL-TYPE CRITERION describes the yield criterion for the compressive behaviour. After the yield criterion is reached first a parabolic hardening behaviour is applied, after which parabolic/exponential softening sets in. The criterion reads,

$$f_2 = \frac{\bar{\sigma}_{cy}(\kappa_c)}{\bar{\sigma}_{cx}(\kappa_c)}\sigma_x^2 + \beta\sigma_x\sigma_y + \frac{\bar{\sigma}_{cx}(\kappa_c)}{\bar{\sigma}_{cy}(\kappa_c)}\sigma_y^2 + \frac{f_{cx} f_{cy}}{\tau_{u,c}^2}(\tau_{xy}^2 + \tau_{yz}^2 + \tau_{xz}^2) - \bar{\sigma}_{cx}(\kappa_c)\bar{\sigma}_{cy}(\kappa_c) = 0 \quad (7.12)$$

where,

$\bar{\sigma}_{cx}(\kappa_t), \bar{\sigma}_{cy}(\kappa_t)$ = yield values
f_{cx}, f_{cy} = uni-axial compressive strengths
$\tau_{u,c}$ = fictitious pure shear strength in compression
κ_c = hardening/softening factor

EXPERIMENTAL VALIDATION was provided by Lourenço (2000) using an experiment of Gazzola et al. (1985). In this study five panels, which are constrained at four edges, are loaded with a face load using airbags. No information was available on the load-displacement relation but the failure load was approximated with an extreme error of 13%. This was probably due to the fact that parameters which were not available were estimated.

7.7 *Comparison of methods*

The methods described in this chapter are compared along the following aspects: number of degrees of freedom (DOF) (estimate for one wall), accuracy, possibility to model in-plane and out-of-plane failure mechanisms and possibility to apply the method to a full building. These aspects form the basis of a comparison with which it should be possible to form a statement about the modelling of a URM wall in out-of-plane bending.

The yield-line theory gives an upper-bound estimate of the capacity of a URM wall. Although Brinker (1984) states that tensile and compressive strength do not influence the capacity, this is highly doubtable. Doherty (2000) states that the wall can have more resistance after cracking or 'yielding'. He defines this as the semi-rigid threshold (Section 3.7). Lourenço (2000) states that a yield-line analysis is not suited for masonry structures since a typical yield-line pattern can only be observed at the ultimate failure, while at peak load a distributed crack pattern is visible.

The linearised displacement based analysis uses a substitute single degree of freedom structure as an approximate for the total wall. This method requires the load-displacement curve of the original structure. which is mostly unknown, and is only applicable to structures which can be reduced to one degree of freedom. The method is therefore hard to scale to a full size structure with multiple walls, floors, windows and piers. This method also gives highly unreliable results with errors up to 50%. Due to the linear nature of the substitute structure computation costs are low. This method can account for the geometrical non-linear effect of the applied overburden via the semi-rigid resistance threshold. The other finite element methods do not account for this shifting of the overburden.

The equivalent frame method has a better applicability. It can model structures as a whole and makes cleaver use of knowledge about the behaviour of URM walls to model the components which stay together after failure or have a specific failure mode, for instance piers which can fail in shear, slip or toe crushing. This way failure mechanisms can realistically be modelled. The TREMURI implementation adds an extra simplification, it reduces the degrees of freedom to in-plane displacements, cancelling the lateral displacement and out-of-plane rotations. A single wall, like in the Doherty tests, can still be modelled using one-dimensional elements. However, two-way bending or scaling to a full structure will give problems.

The rigid element method looks like a promising alternative. It models the wall as a set of elements connected with rotation springs. It could be seen as a simplification of the multisurface interface model, with bigger elements and only out-of-plane degrees of freedom. This simplification makes the method only applicable for out-of-plane problems and thus modelling of a full building is not possible. This method does use damage parameters. It does give results which are comparable with the finite element method with nine times less degrees of freedom.

THE MULTISURFACE INTERFACE MODEL gives a micromodelling approach to the URM problem. The model is able to capture all failure modes and is therefore more realistic. Unloading and reloading however is not realistically modelled. The number of interfaces and elements require a lot of degrees of freedom. This drastically increases the computation costs especially when an implicit time-integration method is used, since this requires the solution of the system as a whole. This reduces the scalability of the method.

THE ANISOTROPIC CONTINUUM MODEL uses continuum elements and a smeared crack approach. Although locally all failure modes can occur the smearing of this effect over the element gives a different local effect than the discrete modelling approach. Therefore the results are only of interest when the structure as a whole is observed. For unloading and reloading DIANA uses a secant stiffness, which is not realistic since it does not account for plastic deformations. Advantage of this method is the reduction of degrees of freedom and no need to predefine cracks. This method is of particular interest if a large structure is observed or the cracks are widely spread over the structure.

Method	DOF’s	Accuracy	Failure mechanisms	Full building model
Yield Line Theory	1	Low	OP	Not possible
Linearised DB Analysis	1	Low	OP / IP	Not possible
Equivalent Frame Method	6	Medium	OP / IP	Possible
Rigid Elements	100	Medium	OP	Not possible
Multisurface Interface Model	900	Very high	IP + OP	Possible
Anisotropic Continuum Model	500	High	IP + OP	Possible

Table 7.1: Ranking of methods in accuracy and computational costs, and applicability for Out-of-plane (OP) and/or In-plane (IP)

FOR THE MODELLING OF A URM WALL with out-of-plane bending the local effects would be of interest. Especially when the strength of the current situation is examined an accurate model is wanted. The anisotropic model would be a good choice however with dynamic implicit time-integration and a full scale building this method has very high computational costs. Therefore the continuum model is more preferable. Two effects can be implemented to give more accurate results; 1) The geometrical non-linear effect of shifting overburden force and 2) the use of damage parameters to find the unloading and reloading stiffness.

8
Conclusion

Unreinforced masonry walls loaded to out-of-plane earthquakes are weak points of URM buildings and provide a real threat to people when failure commences. However, a relative low number of experimental studies have been performed in this area of seismic design.

FOR THE CASE OF GRONINGEN were earthquakes are becoming more frequent and more powerfull the need for a reliable and quick analysis method is growing. The Doherty out-of-plane benchmark will be analysed as a part of the Groningen research program. This analysis will be performed by TU Delft, EUCENTER and ARUP and later cross validation of the methods will be performed. The other two institutes will use TREMURI, which is an Equivalent Frame Method and LS-Dyna, which is based on the Multisurface Interface Model and uses explicit time-integration.

IN THE PRESENT STUDY DIANA is used with the Anisotropic Continuum Model and implicit time-integration to model a URM wall. From this literature review it can be concluded that hysteresis loops, which are dependent on unloading and reloading stiffness and geometric non-linearities relating the applied force and the location of the support, are important for simulation. The goal of this research is to model a URM wall in an efficient and accurate manner. The research questions are:

- Can a URM wall in out-of-plane bending due to earthquake excitation be modelled with the Anisotropic Continuum Model?
- Does the use of damage parameters for the unloading and reloading improve the accuracy of the hysteresis effect for a URM wall in out-of-plane bending?
- Can shifting of the overburden force due to non-linear effects be applied to improve the accuracy of the post-peak behaviour for a URM wall in out-of-plane bending?

Nomenclature

$\ddot{\mathbf{g}}$	Imposed accelerations
$\ddot{\mathbf{q}}$	Generalized accelerations
$\dot{\mathbf{q}}$	Generalized velocities
$\mathbf{C}$	Generalized damping matrix
$\mathbf{f}^0$	Generalized forces
$\mathbf{G}$	Participation matrix
$\mathbf{K}$	Generalized tangential stiffness matrix
$\mathbf{M}$	Generalized mass matrix
$\mathbf{q}$	Generalized displacements
$\mathcal{T}$	Kinetic energy
$\mathcal{V}_d$	Potential damping energy
$\mathcal{V}_e$	Potential elastic energy
E_m	Youngs modulus masonry
$f_{m;c}$	Compressive strength masonry
$f_{m;t}$	Flexural tensile strength masonry
$f_{mor;c}$	Compressive strength mortar

Acronyms

DOF degrees of freedom. 38
DPC Damp Proof Course. 19

IP in-plane. 39

OP out-of-plane. 39

URM unreinforced masonry. 5

Bibliography

ABK (1984). Methodology for the Mitigation of Seismic Hazards in Existing Unreinforced Masonry Buildings: The Methodology. *Topical Report*, 8.

Aref, A. J. and Dolatshahi, K. M. (2013). A three-dimensional cyclic meso-scale numerical procedure for simulation of unreinforced masonry structures. *Computers & Structures*, 120:9–23.

Bariola, J., Ginocchio, J., and Quinn, D. (1990). Out-of-plane seismic response of brick walls. In *Proceedings of the 5th North American Masonry Conference*, pages 429–439.

Brinker, R. (1984). Yield-Line Theory and Material Properties o f Laterally Loaded Masonry Walls. *Masonry International*, 1:8–17.

Bruneau, M. (1994). State-of-the-art report on seismic performance of unreinforced masonry buildings. *Journal of structural engineering*, 120(1):230–251.

Calvi, G. and Kingsley, G. (1996). Problems and certainties in the experimental simulation of the seismic response of MDOF structures. *Engineering Structure*, 18(3):213–226.

Casolo, S. (2000). Modelling the out-of-plane seismic behaviour of masonry walls by rigid elements. *Earthquake Engineering & Structural Dynamics*, 29(September):1797–1813.

Dassault Systèmes (2013). 4.5.2 Damaged plasticity model for concrete and other quasi-brittle materials. In *Abaqus 6.13 Online Documentation*, number 1998, chapter 4.5.2. Dassault Systèmes.

Doherty, K., Griffith, M. C., Lam, N., and Wilson, J. (2002). Displacement-based seismic analysis for out-of-plane bending of unreinforced masonry walls. *Earthquake Engineering & Structural Dynamics*, 31(4):833–850.

Doherty, K. T. (2000). *An investigation of the weak links in the seismic load path of unreinforced masonary buildings*. Phd, University of Adelaide A.

Dolatshahi, K. M., Aref, A. J., and Yekrangnia, M. (2014). Bidirectional behavior of unreinforced masonry walls. *Earthquake Engineering & Structural Dynamics*.

Gazzola, E., Drysdale, R., and Essawy, A. (1985). Bending of concrete masonry walls at different angles to the bed joints. In *Proceedings of 3th North American Masonry conference Arlington, Paper*, volume 27.

Griffith, M. C., Vaculik, J., Lam, N. T. K., Wilson, J., and Lumantarna, E. (2007). Cyclic testing of unreinforced masonry walls in two-way bending. *Earthquake Engineering & Structural Dynamics*, 36(6):801–821.

Guillaud, H., Joffroy, T., and Odul, P. (1995). *Compressed Earth Blocks - Volume II. Manual of design and construction.*

KNMI (2013). Aardbevingen door gaswinning in Noord-Nederland.

Lagomarsino, S., Penna, A., Galasco, A., and Cattari, S. (2013). TREMURI program: An equivalent frame model for the nonlinear seismic analysis of masonry buildings. *Engineering Structures*, 56:1787–1799.

Lee, J. and Fenves, G. L. (1998). Plastic-Damage Model for Cyclic Loading of Concrete Structures. *Journal of Engineering Mechanics*, 124(8):892–900.

Losberg, A. and Johansson, S. (1969). Sideway pressure on masonry walls of brickwork. In *Proceedings International Symposium on Bearing Walls,(CIB), Warsaw*.

Lourenço, P. B. (2000). Anisotropic softening model for masonry plates and shells. *Journal of Structural Engineering*, 126(9):1008–1016.

Lourenço, P. B., Borst, R. D., and Rots, J. G. (1997). A plane stress softening plasticity model for orthotropic materials. *International Journal for Numerical Methods in Engineering*, 40(2):4033–4057.

Lourenço, P. B., Rots, J. G., and Blaauwendraad, J. (1998). Continuum model for masonry: parameter estimation and validation. *Journal of Structural Engineering*, 124(6):642–652.

Lourenco, P. B. and Rots, J. G. (1997). Multisurface interface model for analysis of masonry structures. *Journal of engineering mechanics*, 123(7):660–668.

Lubliner, J., Oliver, J., Oller, S., and Onate, E. (1989). A plastic-damage model for concrete. *International Journal of Solids and Structures*, 25(3):299–326.

Mendes, N. and Lourenço, P. B. (2009). Seismic Assessment of Masonry "Gaioleiro" Buildings in Lisbon, Portugal. *Journal of Earthquake Engineering*, 14(1):80–101.

Paulay, T. and Priestly, M. (1992). *Seismic Design of Reinforced Concrete and Masonry Buildings*.

Penna, A., Rota, M., Mouyiannou, A., and Magenes, G. (2013). Issues on the use of time-history analysis for the design and assessment of masonry structures. In Papadrakakis, M., Papadopoulos, V., and

Plevris, V., editors, *Proceedings of 4th ECCOMAS Thematic Conference on Computational Methods in Structural Dynamics and Earthquake Engineering*, number June, Kos Island, Greece.

Pluijm van der, R. (1997). Non-Linear Behaviour of Masonry. *HERON*, 42(1):25–54.

Priestly, M. (1985). Seismic behaviour of unreinforced masonry walls. *Bulletin of the New Zealand National Society for Earthquake Engineering*, 18(2):191 – 205.

Roca, P., Molins, C., Marí, A. R., and Asce, M. (2005). Strength Capacity of Masonry Wall Structures by the Equivalent Frame Method. *Journal of Structural Engineering*, 130(October):1601–1610.

RTV Noord (2014). Onduidelijkheid over ingestorte boerderij Bedum.

Shibata, A. and Sozen, M. A. (1976). Substitute-structure method for seismic design in R/C. *Journal of the Structural Division*, 102(1):1–18.

JOS VAN DAM

MODELLING REPORT

DELFT UNIVERSITY OF TECHNOLOGY

Revisions

Rev.	date	status	remark
0	11-4-2015	concept	Discussed at fourth committee meeting
1	20-5-2015	for review	Adjusted with comments from Max Hendriks
2	4-6-2015	final	

STRUCTURAL MECHANICS, DELFT UNIVERSITY OF TECHNOLOGY

Submitted on 4th June 2015. Revision 2

Contents

Introduction

The behaviour of unreinforced masonry walls can be described by it's geometric and physical non-linear behaviour. To come to a good understanding of both influences a systematic approach has been chosen in which complexity of the model is gradually increased. This way the validity of the final model can be proven. The resulting series of models, the results and the challenges that came with them are presented in this document.

In the first models the physical behaviour is of main importance. From a theoretical stress strain relationship the force-displacement relation is derived. This is validated with the second finite element method which has a discrete cracking material model applied to it.

The geometric non-linear behaviour of the cracked unreinforced masonry wall described by Doherty as 'rocking bodies' is modelled in the third model. Two bodies can be observed with a cracked cross-section in between. This is modelled using two rigid beams connected by a set of elements representing the cracked cross-section. This set of elements only allows movement of the two rigid bodies as if they were rocking.

In the final three models the physical and the geometrical behaviour are combined and the wall is loaded with accelerations from Doherty's experiment. The results are presented and discussed to finally validate the model and use it for comparison purposes.

Overview of models

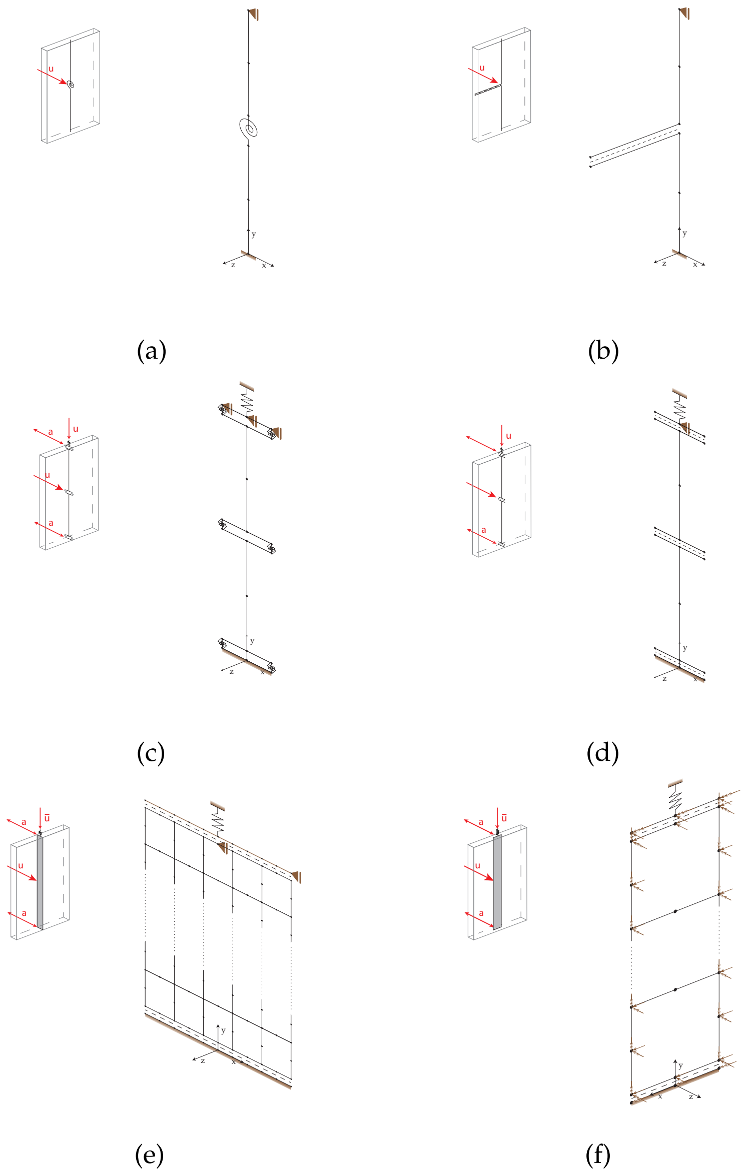

(a) (b) (c) (d) (e) (f)

Figure 1: Overview of numerical models investigated in this study.

(a) Physical Non-linear Spring Model

(b) Discrete Crack Model

(c) Geometric Non-linear Spring Model

(d) Physical and Geometrical Non-linear Interface Model

(e) Plane Strain Model

(f) Curved Shell Model

1

Experimental Details

In 1998 Kevin Doherty tested 14 unreinforced masonry brick walls on the out-of-plane bending resistance. He subjected these walls to quasi-statically imposed horizontal displacement, pulses as well as transient excitations. The goal of this thesis is to use this experiment to validate a numerical model made with the finite element package DIANA from TNO Diana. For this purpose it is important to have a thorough understanding of the experiment conducted. The following points are of importance: geometry, material properties, experimental setup and boundary conditions, loads, instruments and their resulting data.

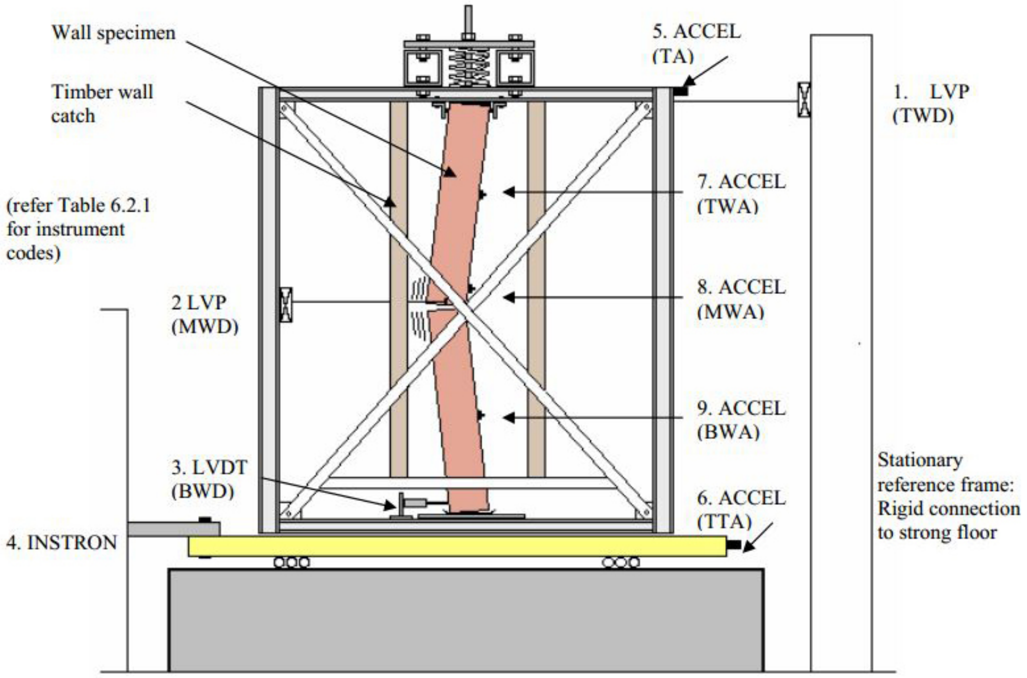

Figure 1.1: Out-of-plane wall test setup and instruments.

1.1 Experimental setup

In Fig. 1.1 the experimental setup is shown. The experiments (quasi-static push test and transient excitations) were performed on the wall supported by a steel frame. Doherty reports that the frame has a significantly higher stiffness and thus also a higher frequency than the wall. This can also be concluded from the acceleration and displacement results from the table and the top of the frame presented in Sec. 1.5. These are comparable and small differences are insignificant to the excitations of the wall itself.

The results of Doherty's tests where recorded using 9 instruments, which are depicted in Fig 1.1, of which five measure the acceleration and four the displacement relative to the steel frame or the rigid surrounding.

1.2 Boundary conditions

Figure 1.2: Top support.

Figure 1.3: Bottom support.

The connections are pictured in Fig. 1.2 and 1.3. At the bottom connection the wall is positioned on a damp proof course (DPC) which is used to keep damp out of the wall and provides some friction between in floor and the wall. The top connection is clamped with two angle cleats and two rubber strips (red in the picture). These restrict the horizontal movement of the wall but allow some rotation. Since it is unknown how much rotational freedom is allowed, full rotational freedom is assumed. On top an overburden rig is attached which can exert a vertical force on the wall and gives some resistance against vertical deformation of the wall due to rotation about the cracks. It consists of a horizontal plate which connects to the wall and a set of springs that connect to the steel frame.

1.3 Geometry

Doherty has tested two sets of walls. Most of the specimen have a thickness of 110 mm but to get more realistic height over thickness ratio's also specimen with a width of 55 mm were tested. The data set obtained at the start of this thesis consists of results for specimen 8, 12, 13 and 14. Their geometrical properties are presented in Table 1.1.

Specimen	Height	Width	Thickness
-	h $[m]$	b $[m]$	t $[m]$
8	1.5	0.95	0.110
12	1.5	0.95	0.110
13	1.5	0.95	0.110
14	1.5	0.95	0.055

Table 1.1: Dimensions of specimen tested by Doherty.

1.4 *Material properties*

Using several material tests Doherty determined most of the material properties. For masonry these are sensitive to imperfections in the wall. Some of the material tests were performed on actual wall segments, but others on separate samples. This reduces the accuracy of the data. For the specimen studied in this thesis the material properties are given in Table 1.2.

Specimen	Mass Density	Youngs Modulus	Masonry Compressive Strength	Mortar Compressive Strength	Flexural Tensile Strength
	ρ $[kg/m^3]$	E_m $[MPa]$	f_c $[MPa]$	f_c $[MPa]$	f_t $[MPa]$
8	1800	5,400	9.7	-	0.45
12	1800	11,600	15.7	-	0.30
13	1800	-	15.7	-	0.29
14	2300	6,700	26.7	-	0.76
Mean	-	9,400 / 8,250 *	13.4 / 26.5 *	5.17	0.49
Stan. dev.	-	5,322 / 2,192 *	1.64 / 0.28 *	-	0.15

Table 1.2: Material properties of specimen tested by Doherty

* The mean values for walls of 110 mm and 50 mm are presented separately.

1.5 *Loads*

The specimen are all loaded with different loads. In Table 1.3 the loads applied on the different specimen are presented. Due to the order in which the wall is loaded the wall has some damage prior to the transient analysis. The state of the wall at the beginning of the transient excitation tests is described by Doherty as new condition (NEW), moderately degraded (MOD) or severely degraded (SEV). These states are however not very helpful since no accurate definition of them is provided. [1]

Construction Lot	Specimen No.	Overburden $[MPa]$	Excitation Signal	Wall Condition	Tests	Data available
June98	8	0.15	-	-	Un-cracked Static Push Test	✓
September98	12	0	-	-	Un-cracked Static Push Test	
		0	100% NH	NEW	Transient Excitation	✓
		0	200% NH	NEW	Transient Excitation	✓
		0	300% NH	NEW	Transient Excitation	✓
		0	400% NH	NEW	Transient Excitation	✓
		0	66% EL	MOD	Transient Excitation	✓
September98	13	0	-	-	Un-cracked Static Push Test	
		0	66% PD	NEW	Transient Excitation	✓
		0	80% PD	NEW	Transient Excitation	✓
		0	100% PD	NEW	Transient Excitation	✓
		0	66% EL	MOD	Transient Excitation	✓
September98	14	0	-	-	Cracked Static Push Test	
		0	100% NH	MOD	Transient Excitation	✓

Table 1.3: Loading of different specimen with availability of data, combination of Tables 6.4.1, 6.4.10-11 from Doherty (2000). Nahanni (NH) and El Centro (EL) are excitation signals applied as loading.

[1] The MOD condition is defined as *visible crack slightly rounded* and the SEV condition as *mortar drop out and crack significantly rounded*.

Damian Grant from ARUP mentioned that the accelerations and the displacements of the Nahanni (NH) data reported by Doherty seem to be inconsistent. He reports that the El Centro (EL) data is consistent. For the Nahanni data a large baseline shift is reported which was not possible to remove.

To verify this the base and top accelerations from instruments 5 (TTA) and 6 (TA), see Fig. 2.3 are integrated twice and compared with the displacements from the instruments 1 (TWD) and 4 (INSTRON) both for the El Centro 66% specimen 12 and Nahanni 100% specimen 12 data sets.

A large baseline shift was indeed found for both input signals. If these signals are used as input in DIANA and the absolute displacements are outputted. The same baseline shifts are found, see Fig. 1.4 and 1.8. These baseline shifts occur due to the unknown integration constant which is again integrated. This is thus a constant velocity and has no effect on the relative behaviour of the wall. DIANA automatically filters this shift out and normally it thus is no issue.

When differentiation is used this problem does not exist and accurate results are found when comparing the accelerations with the displacements, see Fig. 1.5 and 1.6, for frane and table accelerations of El Centro signal and 1.9 and 1.10 for frane and table accelerations of Nahanni signal. The Nahanni 100% specimen 12 show some differences for the table accelerations however from numerical tests it will be shown that the input results in similar midwall excitations and thus the signal is consistent.

El Centro 66% on specimen 12

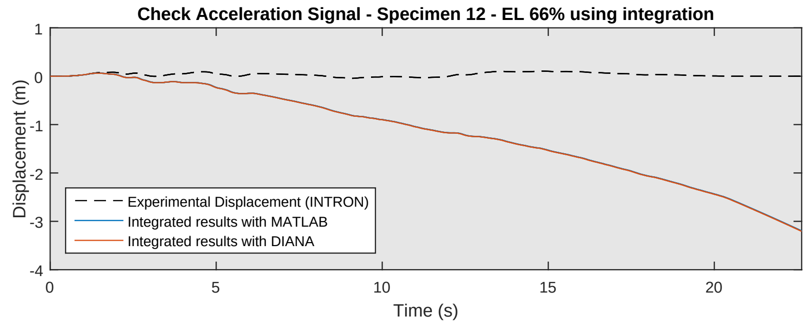

Figure 1.4: Integrated acceleration signal compared with displacement, with hand calculation and DIANA, for El Centro 66% acceleration signal.

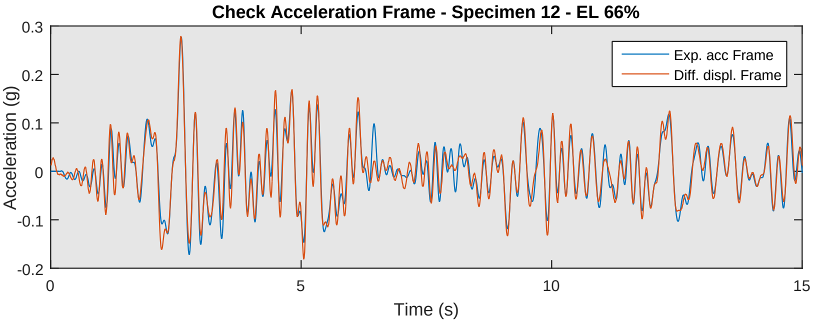

Figure 1.5: Check acceleration of the frame at the top of the wall for specimen 12 with El Centro 66% acceleration signal.

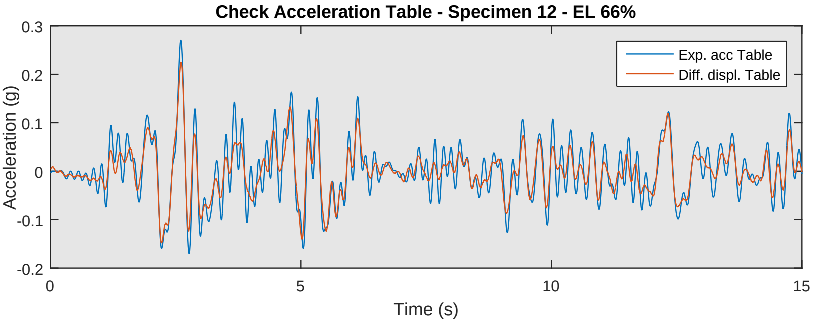

Figure 1.6: Check acceleration of the frame at the top of the wall for specimen 12 with El Centro 66% acceleration signal.

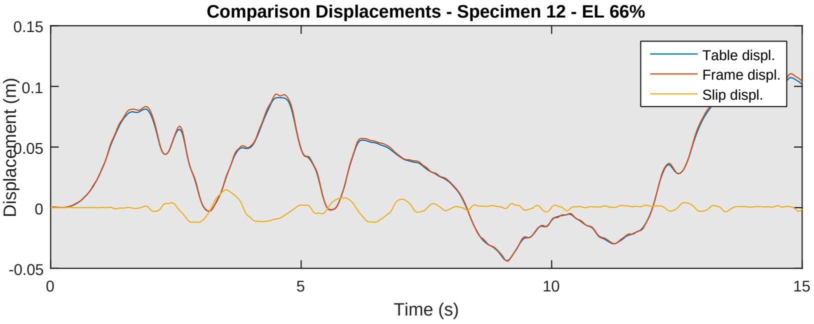

Figure 1.7: Comparison of absolute displacements of the table and top frame, and relative displacement of bottom wall and mid-height wall for specimen 12 with El Centro 66% acceleration signal.

Nahanni 100% on specimen 12

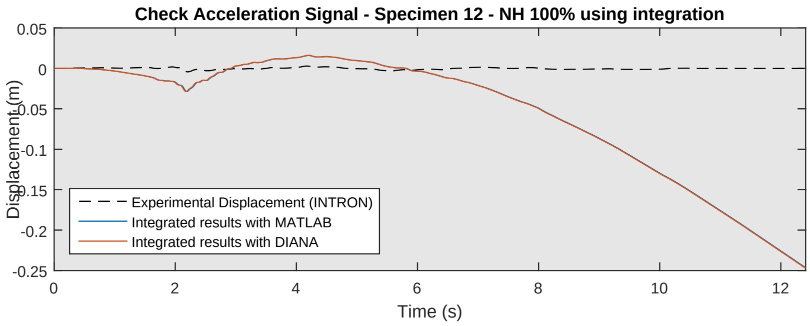

Figure 1.8: Integrated acceleration signal compared with displacement, with hand calculation and DIANA, for Nahanni 100% acceleration signal.

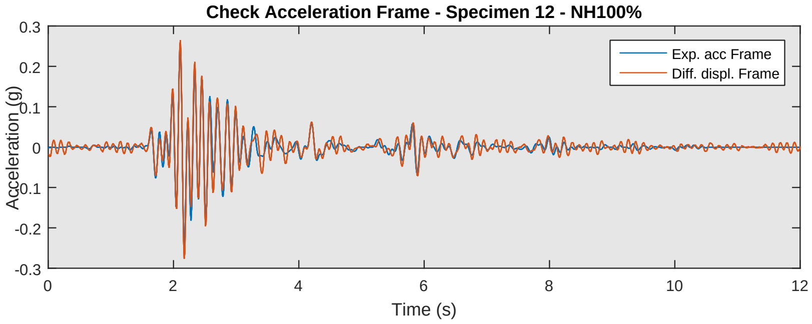

Figure 1.9: Check acceleration of the frame at the top of the wall for specimen 12 with Nahanni 100% acceleration signal.

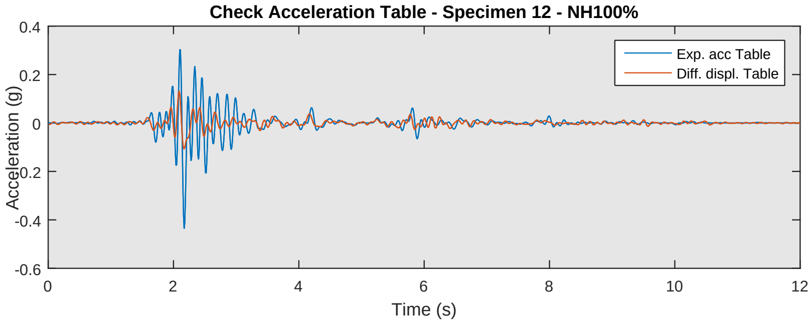

Figure 1.10: Check acceleration of the frame at the top of the wall for specimen 12 with Nahanni 100% acceleration signal.

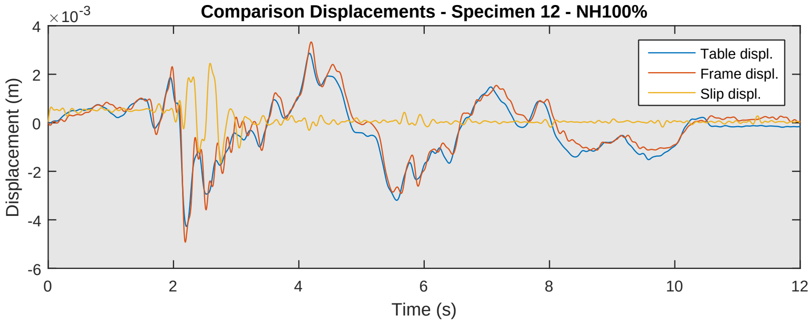

Figure 1.11: Comparison of absolute displacements of the table and top frame, and relative displacement of bottom wall and mid-height wall for specimen 12 with Nahanni 100% acceleration signal.

2

Physical Non-linear Spring Model

The first and simplest model of the URM wall in out-of-plane bending consists of two elements and a rotational spring and is a simplification of the method of Casolo, where the elements are rigid and all the deformation is lumped in the spring. The model is depicted in Fig. 2.1. The main goal of this model is to get a better understanding of the material behaviour of the masonry.

The spring should, with the two connected elements, mimic the behaviour of a wall in out-of-plane bending. This includes elastic deformation of the wall as well as deformation due to cracking. The axial force on the top of the wall does play a big role when geometric effects are considered since the arm of this force to the point of rotation is dependent on the deformed state of the wall. However in this model only the effect of the axial force on the physical resistance of the wall is considered. In later chapters the geometric effects are taken into account.

The behaviour is lumped in the rotational spring for which a non-linear stiffness is derived using a material model based on fracture energy. The resulting relationship is linearized and implemented in DIANA using the user-supplied subroutine for springs.

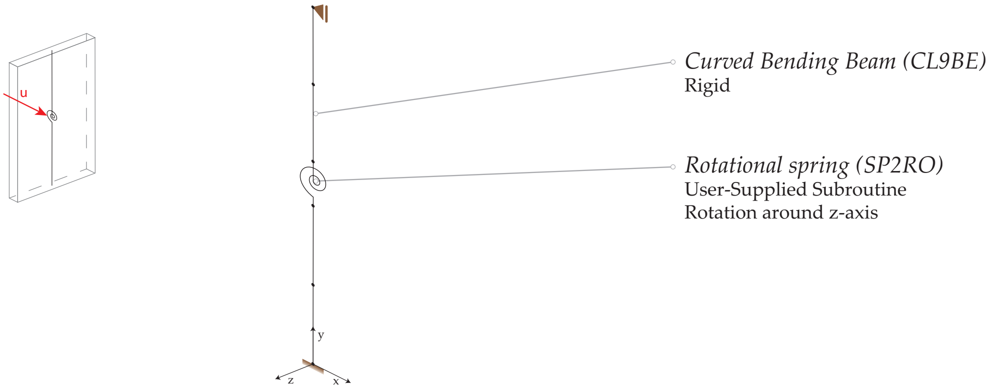

Figure 2.1: One-dimensional model with non-linear spring

2.1 *Discretization*

The model consists of two curved beam elements (CL9BE) and a rotational spring (SP2RO).

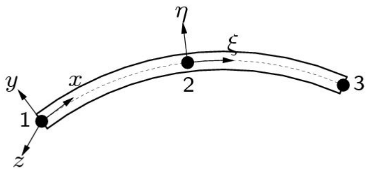

Figure 2.2: Curved beam element (CL9BE) (TNO DIANA BV, 2014)

Figure 2.3: Rotational spring (SP2RO) (TNO DIANA BV, 2014)

The beam elements have three nodes, with three degrees of freedom (u_x, u_y and ϕ_z). Quadratic interpolation of the displacements can be applied, this causes the strains to vary linearly over the height.

The rotational spring has two nodes with each one rotational degree of freedom ϕ_z. The z-axis is thus the axis of rotation for the rotational spring.

The nodes are numbered from the bottom (1) to the top (6) of the wall.

2.2 *Geometry*

The typical dimensions are presented in Table 2.1.

Dimension			Beam Element (CL9BE)	Rotational Spring (SP2RO)
Length	l	$[m]$	0.75	0
Area	A	$[m^2]$	0.95×0.11	-

Table 2.1: Typical dimensions of the elements in Physical Non-linear Spring Model.

2.3 *Boundary Conditions*

The wall is simply supported, see Table 2.2. The translational degrees of freedom of the two beam elements at mid-height of the wall are connected using tyings.

Set	Node	u_x	u_y	ϕ_z
Top node	6	✓	-	-
Bottom node	1	✓	✓	-

Table 2.2: Boundary conditions of the Physical Non-linear Spring Model.

2.4 *Material properties*

A linear elastic material model is applied to the beam elements. The general material properties are presented in Table 2.3.

Element	Mass Density $\rho\ [kg/m^3]$	Youngs Modulus $E\ [N/m^2]$	Poisson's Ratio $\nu\ [-]$	Stiffness $K\ [Nm/rad]$
Beam elements (CL9BE)	1800	5.4×10^12	0.0	-
Rotational spring (SP2RO)	-	-	-	1.0×10^9 ×

Table 2.3: Material parameters applied in Physical Non-linear Spring Model.

× Non-linear material model applied using User-Supplied Subroutine, see Fig. 2.5

Via a user-supplied subroutine the total physical non-linear behaviour (Fig. 2.4.a, Table 2.4) of the wall is enforced. To find the moment-rotation behaviour of the wall after cracking a numerical derivation is performed for a theoretical approach.

The shear stress over the thickness is assumed to be zero and the stress normal to the cross-section is evaluated using the constitutive relation for the stress and the relative deformation. With the normal force, the vertical equilibrium is iteratively found by adjusting the point of rotation in the cross-section. The moment is found by evaluating the equivalent forces of the stress times the arm to the point of rotation. The resulting moment-normal-force-rotation relationship is depicted in Fig. 2.4.c. The full derivation is given in Section 2.A

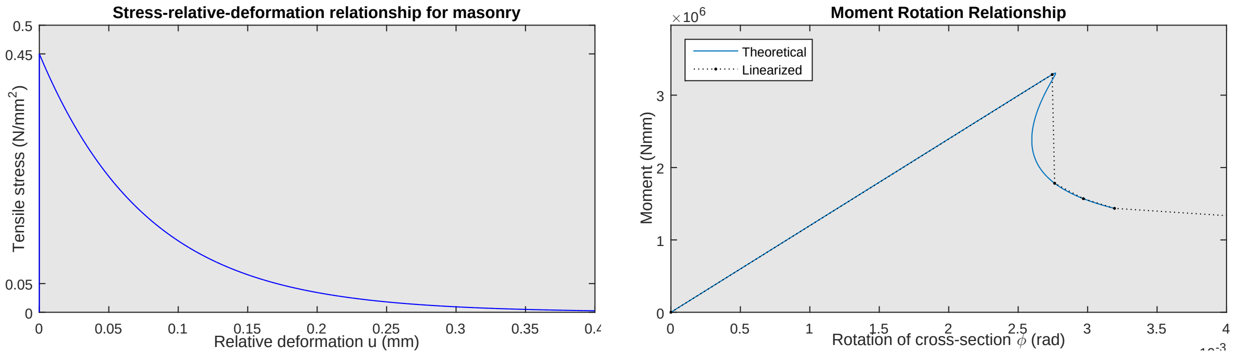

Figure 2.4: a. Stress-strain relationship that should be applied to the individual straws. b. Straw model. c. Moment-Normal force-rotation relationship

Element	Tensile strength $f_t\ [N/m^2]$	Mode-I fracture energy $G_{ft}\ [J/m^2]$	Compressive strength $f_c\ [N/m^2]$
Masonry	0.45×10^6	35	5.17×10^6

Table 2.4: Material parameters of masonry.

2.A *Derivation Moment-rotation Relationship*

The moment rotation relationship of a masonry wall cross-section during cracking is numerically derived. This behaviour is dependent on the strength of the wall as well as the fracture energy belonging to the failure mode.

The moment rotation relationship can be split into two parts. Pre-cracking where the behaviour is linear and post-cracking where it is non-linear. In the following two sections the behaviour will be discussed and derivation and calculations will be elaborated.

Pre-cracking The cracking resistance can be found from the moment at which the ultimate tensile strength is reached in one of the outer fibres. The stress in the outer fibre is dependent on the normal force and the moment in the cross-section. Until cracking, the rotational spring should remain closed and the spring should thus behave very stiff.

The cracking moment is equal to,

$$M_{cr} = \frac{2}{3}\, t \cdot f_t \cdot \frac{1}{4}\, t\, b = \frac{1}{6}\, f_t\, t^2\, b \tag{2.1}$$

Before cracking the deformation is purely elastic and due to bending of the wall. In this model the wall is modelled by two rigid beam elements and thus the elastic deflection of the wall should be replicated by the rotational spring,

$$w_{el} = \frac{1}{2}\, \varphi_{el}\, \frac{h}{2} \tag{2.2}$$

$$w_{el} = \frac{1}{48}\, \frac{F\, h^3}{E\, I} \tag{2.3}$$

Since the wall is simply supported we know that,

$$M = \frac{1}{4}\, F\, h \tag{2.4}$$

$$F = \frac{4\, M}{h} \tag{2.5}$$

Combining results in,

$$\varphi_{el} = \frac{M\, h}{3\, E\, I} \tag{2.6}$$

From the relation between the moment and the cracking rotation we can use this equation to calculate the elastic rotation that corresponds to every moment. If we then sum up the two rotations we end up with the total rotation of the spring.

Post-Cracking The post-cracking behaviour is described by the fracture energy. This reduces the stress for continued deformation of the cracked tensile fibres. An exponential softening curve is used to define the stress-strain relationship (depicted in Fig. 2.4.a),

$$\sigma(\Delta u) = f_t \cdot e^{-\lambda \Delta u}$$

The exponential decay parameter λ can be found from the fraction energy,

$$G_t = \int_0^\infty f_t\, e^{-\lambda u}\, du = \left[-\frac{1}{\lambda}\, f_t\, e^{-\lambda u} \right]_0^\infty = 0 + \frac{f_t}{\lambda}$$

$$\lambda = \frac{f_t}{G_t}$$

Equilibrium iterations The rest of the moment-rotation relationship is obtained by numerical iterations. With an incremental rotation an attempt is made to find a stress distribution for the current rotation and the associated elongations of the fibres which makes equilibrium with the normal force. If needed the point of rotation is shifted until equilibrium is found.

From the found equilibrium the moment is calculated. The cross-section is divided into three parts according to the relative deformation of the fibres, a compressive area, a linear elastic tensile area and a cracked tensile area. The stresses are integrated over the area to obtain the equivalent forces and the moment arm,

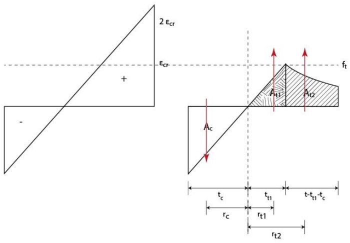

Figure 2.5:

$$\begin{aligned}
F_{t;1} &= \frac{1}{2}\, f_t\, t_{t1}\, b \\
F_{t;2} &= b \int_0^{t-t_{t1}-t_c} f_t\, e^{-\lambda u(x)}\, dx \\
u(x) &= \frac{u_t - u_{cr}}{t - t_c - t_{t1}} \cdot x \\
&= b \left[-\frac{f_t}{\lambda} \cdot \frac{t - t_c - t_{t1}}{u_t - u_{cr}} \cdot e^{-\lambda u(x)} \right]_0^{t-t_{t1}-t_c} \\
F_c &= \frac{1}{2}\, \frac{f_t}{t_{t1}}\, t_c^2\, b
\end{aligned}$$

Now the arm between the two forces can be found using the first moment of area using integration by parts. [1]

$$\begin{aligned}
S_{y;t;2} &= \int_0^{t-t_{t1}-t_c} x\, f_t\, e^{-\lambda u(x)}\, dx \\
u(x) &= \frac{u_t - u_{cr}}{t - t_c - t_{t1}} \cdot x = \alpha x \\
&= -\frac{x\, f_t}{\lambda\, \alpha}\, e^{-\lambda \alpha x} \Big|_0^{t-t_{t1}-t_c} - \int_0^{t-t_{t1}-t_c} -\frac{f_t}{\lambda \alpha} e^{-\lambda \alpha x}\, dx \\
&= -\frac{x\, f_t}{\lambda \alpha}\, e^{-\lambda \alpha x} \Big|_0^{t-t_{t1}-t_c} - \frac{f_t}{\lambda^2 \alpha^2}\, e^{-\lambda \alpha x} \Big|_0^{t-t_{t1}-t_c} \\
&= -\frac{(t - t_{t1} - t_c)\, f_t}{\lambda \alpha}\, e^{-\lambda (u_t - u_{cr})} + \frac{f_t}{\lambda^2 \alpha^2} \left(1 - e^{-\lambda (u_t - u_{cr})} \right)
\end{aligned}$$

---

[1] Integration by parts,

$$\int u\, dv = u\, v - \int v\, du$$

$$u = x \qquad v = -\frac{f_t}{\lambda}\, e^{-\lambda (t-a-b)}$$

$$du = dx \qquad dv = f_t\, e^{-\lambda (t-a-b)}\, dx$$

The arm of the equivalent force of the part of the tension zone is equal to,

$$r_{t;2} = t_{t1} + \frac{S_{y;t;2}}{F_{t;2}/b}$$

The arm of the total tension zone is,

$$r_t = \frac{\frac{2}{3}\, t_{t1}\, F_{t;1}/b + r_{t;2}\, F_{t;2}/b}{F_{t;1}/b + F_{t;2}/b}$$

The normal force adds a constant force to be added to the cross-section. This causes the rotation point of the moment to be shifted. This shift should be adjusted for and can be calculated using,

$$\Delta x_{na} = \left(\sigma_c + \frac{N}{A}\right)\frac{t_{c1}+t_{t1}}{\sigma_t+\sigma_c} - t_{c1};$$

The final moment-rotation relationship can be found in Fig. 2.6 The moment-rotation relationship can be found in blue as well as the linearized relationship in black. The linearized diagram will be used by DIANA using the user-supplied subroutine.

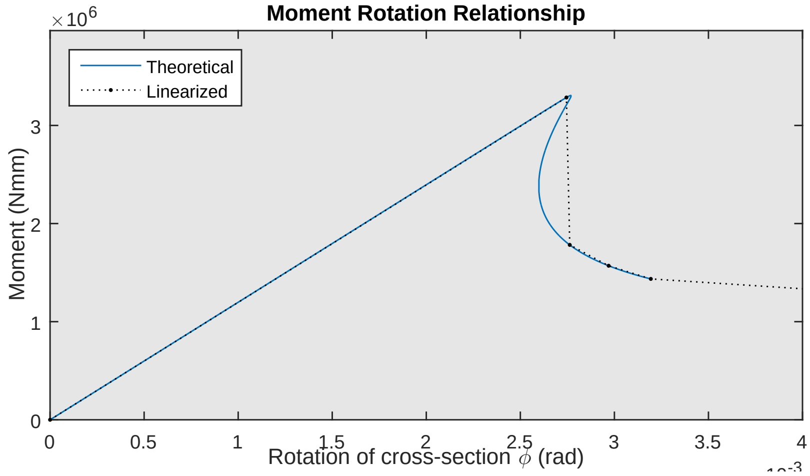

Figure 2.6: Moment-rotation relationship for user-supplied subroutine as well as stress distribution over the cross-section for given rotations.

2.5 User-Supplied Subroutine

To implement the linearized non-linear behaviour of the rotation spring, the user-supplied subroutine USRSPR is used. The input and output variables are obtained from DIANA-9.5 User's Manual. A schematized representation of the Fortran program written to implement the NL spring is presented in Fig. 2.7 and the Fortran program is added to Sec. **??**.

Explanation of USRSPR The USRSPR user-supplied subroutine updates the moment, rotation and the stiffness of the spring for a given original and incremental rotation, schematized in rows 6 and 7 of Fig. 2.7. DIANA uses the moment as an internal force of the element and the stiffness for numerical iteration towards the next result. The updated stiffness from the USRSPR is used in DIANA's iteration procedure and determines the convergence and numerical stability of the model. The numerical convergence of the non-linear spring model is presented in Fig. 2.10.

The moment in the spring depends on its history, and thus hysteresis effects can be found. To implement these effects the maximum and minimum rotation as well as its associated moment are saved as state variables. These variables are passed to the next iteration step. In every step the final rotation is compared to the extreme values, and if needed these are adjusted. This procedure is schematized in Fig. 2.7 in rows 8 and 9.

The reloading and unloading stiffness is determined using these state variables. Since the unloading of the material means unloading of the individual straws of the cross-section, secant unloading of the individual straws does not have to mean secant unloading of the total cross-section. In Section 2.A a prove is given that for secant unloading this reasoning can be made and for non-secant unloading not. In rows 2 to 5 the loading state of the analysis is determined and the stiffness is updated.

Programming the USRSPR gave some difficulties. The model sometimes shows an incorrect stiffness. For example, the secant stiffness for unloading is used for updating the rotation while the load is still increasing and not reloading. These errors in the USPRSPR algoritm result in incorrect moment-rotation diagrams. This is overcome by adding an error margin, see Section 2.B.

The user-supplied subroutine can be expended to obtain a full $M - N - \varphi$ relationship. This can be done by translating the MATLAB numerical derivation to FORTRAN. The normal force can be obtained from one of the adjoining beam elements. An extra iteration loop should be added to the subroutine where the elastic and cracking components of the rotation are dertemined. This is possible since the moment in the spring can be calculated for both individual components and they should be equal. If this is implemented there is no need for a linearized moment-rotation diagram. The tangential moment can than be calculated for all possible rotations.

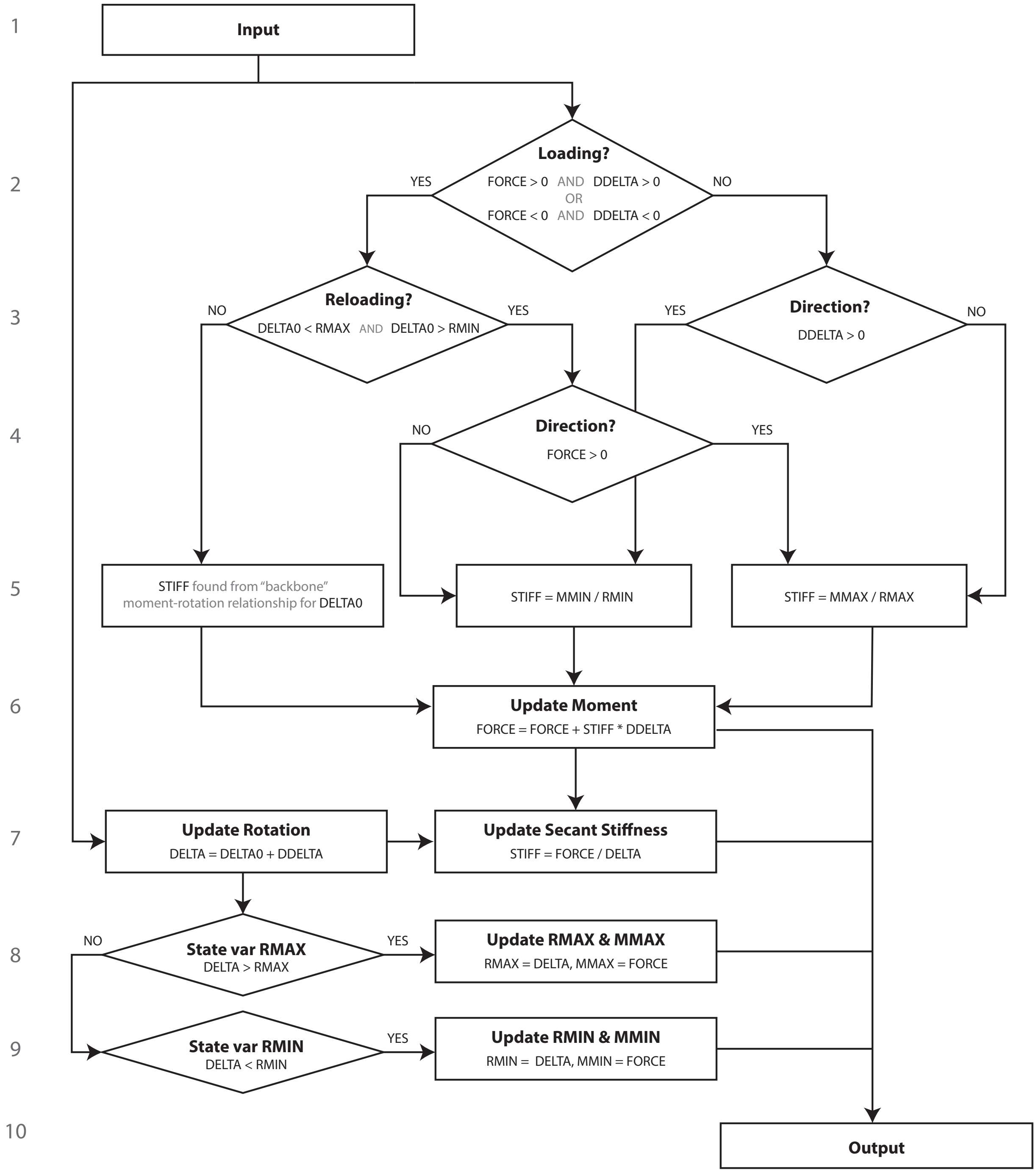

Figure 2.7: Schematized representation of User-Supplied Subroutine USRSPR

2.6 *Loads*

Self-weight and a cyclic horizontal displacement is applied on this model. The details of the loads applied on the model are presented in Table 2.5 for the static analysis.

Order of application	Type of load	Point of application	Amount (steps)	Direction
1	Self-weight	-	- (1)	-y
2	Displacement	Node 3	2.5×10^{-3} m (40), -2.5×10^{-3} m (40)	x

Table 2.5: Applied loads on USRSPR Model during static analysis.

2.7 *Convergence Criteria*

For the static three convergence criteria have been specified. The incremental step is converged if all three criteria are simultaneously met. The iteration method continuous with the next step if the criteria are not met and the maximum number of iterations is reached. Only when the intermediate solution diverges the calculation is aborted.

Details on the convergence criteria are specified in Table 2.6.

Method	Convergence norm	Rel. convergence tolerance
Newton-Raphson	Displacement	$1.0 \cdot 10^{-3}$
"	Force	$1.0 \cdot 10^{-3}$
"	Energy	$1.0 \cdot 10^{-3}$

Table 2.6: Details on convergence criteria of USRSPR Model.

2.8 *Static Analysis*

The load-displacement diagram resulting from the static analysis is presented in Fig. 2.9. In Fig. 2.10 the convergence plot from the loading part of the analysis as well as the deformed shape of the wall before and after cracking is shown.

From the deformed shape it can be concluded that the non-linear spring behaves as expected, first stiff as an interface element and after cracking it takes all the deformation and the beams are almost not bended any more.

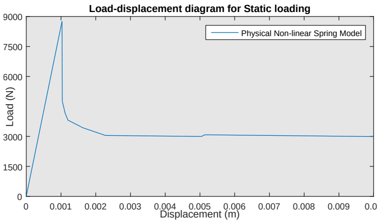

Figure 2.8: Loading direction for static analysis of USRSPR Model.

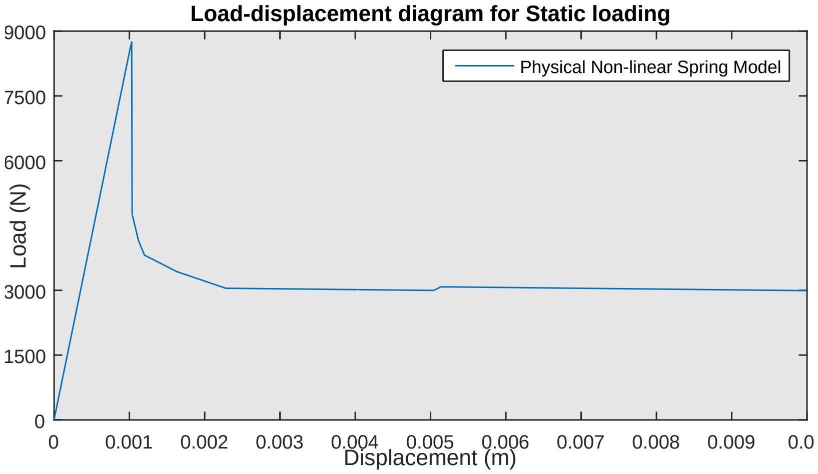

Figure 2.9: Load-displacement diagram from static analysis of Physical Non-linear Spring Model.

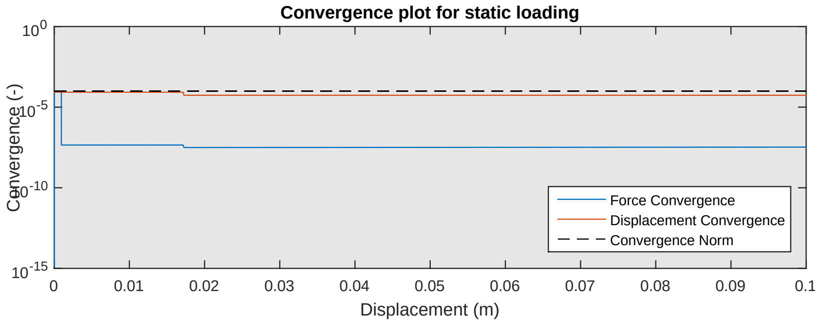

Figure 2.10: Convergence plots from static analysis of Physical Non-linear Spring Model.

2.9 Conclusion

The non-linear material behaviour of the masonry is translated to a moment-normal-force-rotation relationship using a constitutive stress-relative-deformation relationship for masonry based on fracture energy. Via a numerical derivation the moment-normal-force-rotation relationship is obtained. The relationship is implemented in a non-linear spring using a user-supplied subroutine.

The numerical derivation shows the shift of the point of rotation during cracking in the cross-section. Also the influence of the axial force on the physical behaviour of the wall is found. This influence is of great importance when trying to prevent cracks.

In the next chapter the found load-displacement curves are compared with result from a discrete cracking model.

2.A Unloading Stiffness NL spring

The non-linear spring has a linearized moment-rotation relationship (Fig. 2.11). This relationship is derived from the loading of the tensile and compressive fibres in the thickness direction of the wall. The stress of the tensile fibres is reduced after the tensile strength is reached (Fig. 2.12). The individual tensile fibres are assumed to unload in a secant manner (Fig. 2.12). However, it is uncertain if this also results in secant unloading of the total cross-section.

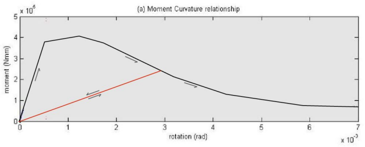

Figure 2.11: Moment-rotation relationship with unloading (red).

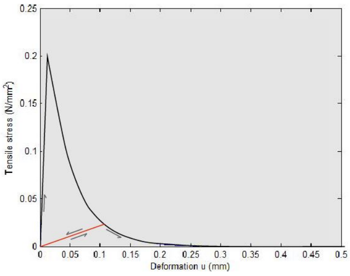

Figure 2.12: Force-deformation relationship with unloading (red).

Thie moment capacity for a given rotation is dependent on two parameters, the arm and the equivalent force. The equivalent force is the stress integrated over the area. Since secant unloading is a linear relation between stress and deformation in a point a reduction of the deformation of all points with a factor 2 would mean a stress reduction of all points with a factor two. This results in an equivalent force reduction with a factor 2. Under the hypothesis that plane sections remain plane, the relationship between the rotation and deformation along the vertical axis of the wall is linear. This means that a reduction of the rotation by halve results in a reduction of the equivalent force by halve. The arm of the couple is influenced by the cracking of the cross-section. The further the crack propagates the smaller the arm becomes, shifting the point of rotation. When secant unloading of the individual fibres is concerned the stress is reduced linearly with the rotation of the cross-section. Therefore the relative distribution of the stress does not change and so the arm is constant. The shift of the point of rotation is caused by the cracking of the cross-section, during unloading and reloading this stays constant since there is no crack propagation.

Thus, secant unloading of the moment-relationship is a result of the secant unloading of the individual fibres. However, non-secant unloading results in a more non-linear relation between local force-deformation and global moment-rotation relationships.

2.B *Transition from reloading to loading*

After some initial good performances the behaviour of the non-linear spring showed some inaccurate behaviour. In Fig. 2.13 and 2.14 show in red the increase of the moment with an incorrect stiffness.

During loading the stiffness suddenly changes to the secant stiffness. This is clearly not right and causes significant higher moment in the spring for large rotations as can be seen in the first figure. This problem is caused by the check for the loading, see Fig. 2.7. The user-supplied subroutine suddenly thinks that the spring is in the reloading state and then changes the stiffness to the secant stiffness.

The check preformed is an IF statement where the rotation at the beginning of the load step, DELTA0, is compared with the minimum and maximum rotations observed so far, RMIN and RMAX. If the load is as in both figures depicted here in the first load cycle, DELTA0 should always be equal to RMIN or RMAX and makes the reloading state impossible to occur. However, if both variables are examined, there is a very small difference are found which occasionally causes the IF statement to be true. This round-off error is probably caused by a permutation of DELTA0 after the user-supplied subroutine saves the same value as the user state variables RMIN and RMAX.

To solve the problem the boundaries in the check for reloading should be adjusted such that DELTA0 has to be equal to RMIN or RMAX but within the margin of a round-off error, now set at 1.0E-017. This solves the problem, see Fig. 2.15. In Fig. 2.16 the error margin is schematically shown. The margin causes a little error in actual transitions from reloading to loading due to earlier unloading. However since the margin is significantly smaller than the incremental step size this is negligible.

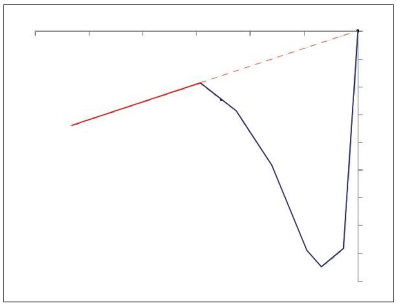

Figure 2.13: Moment-rotation diagram with secant loading in red.

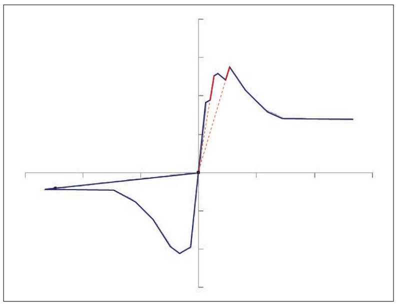

Figure 2.14: Moment-rotation diagram with secant loading in red (2).

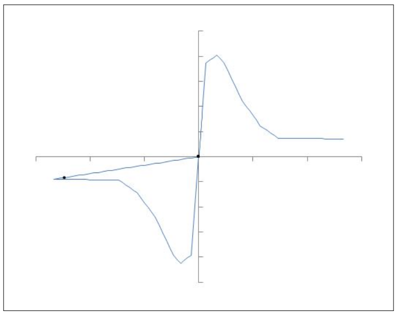

Figure 2.15: Proper moment-rotation diagram.

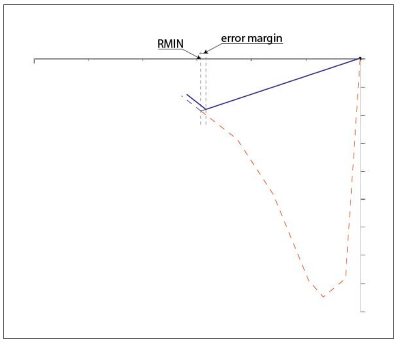

Figure 2.16: Error margin.

3

Discrete Crack Model

The Discrete Crack Model is used to check the derived relationship of the Physical Non-linear Spring Model. It is applied using a line interface element which is placed in between the beam elements in the longitudinal direction of the wall. The two ends of the line interface element are tied together to reduce the element to two nodes which are connected to the beams. Over the width of the interface element (in x-direction), eleven integration points are used to apply the material model.

The goal of this model is to confirm the results found in Chapter 2 by comparing the load-displacement diagrams. This would confirm the understanding of the cracking mechanism of the out-of-plane behaviour of masonry walls.

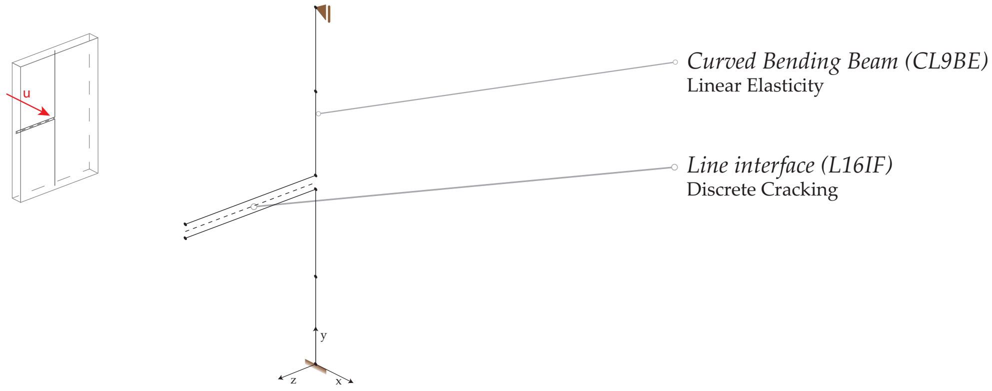

Figure 3.1: Schematized representation of the Discrete Crack Model.

3.1 *Discretization*

The model consists of two curved bending beam elements (CL9BE) and a line interface elements (L16IF).

The beam elements have three nodes, with three degrees of freedom (u_x, u_y and ϕ_z). Quadratic interpolation of the displacements can be applied, this causes the strains to vary linearly over the height.

The line interface element has four nodes, with four degrees of freedom (u_x, u_y, u_z and ϕ_z). It has eleven integration points in the thickness direction of the wall. Since only the behaviour of the wall over the thickness of the element is of interest the two bottom nodes and the two top nodes are tied to each other.

The nodes are numbered from the bottom of the wall (1) to the top (6). The extra nodes of the line interface element are from bottom (13) to top (14).

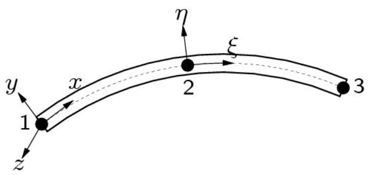

Figure 3.2: Curved beam element (CL9BE) (TNO DIANA BV, 2014)

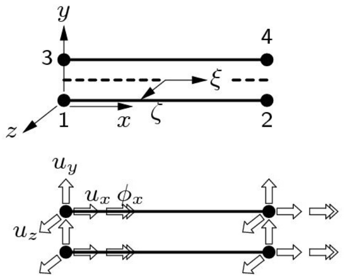

Figure 3.3: Line interface element (L16IF) (TNO DIANA BV, 2014)

3.2 *Geometry*

The typical dimensions are presented in Table 3.1.

Dimension			Beam Element (CL9BE)	Line Interface Elements (L16IF)
Thickness	t	$[m]$	-	0.11
Length	l	$[m]$	0.75	0.95
Area	A	$[m^2]$	0.95×0.11	-

Table 3.1: Typical dimensions of the elements in Discrete Crack Model.

3.3 *Boundary Conditions*

The wall is simply supported, see Table 3.2.

Set	Node	u_x	u_y	ϕ_z
Top node	6	✓	-	-
Bottom node	1	✓	✓	-

Table 3.2: Boundary conditions of the Discrete Crack Model.

3.4 *Material properties*

A linear elastic material model is applied to the beam elements and the discrete crack material model is applied to the line interface element. The general material properties are presented in Table 3.3.

Element	Mass Density $\rho\ [kg/m^3]$	Youngs Modulus $E\ [N/m^2]$	Poisson's Ratio $\nu\ [-]$	Stiffness $D_{STIF}\ [N/m^3]$
Beam Elements (CL9BE)	1800	5.4×10^9	0.0	-
Line interface (L16IF)	0	-	-	$1.0 \times 10^{13}\ N/m^3$ ×

Table 3.3: Material parameters applied in Plane Strain Model.

× Discrete Crack model applied

On the line interface elements the Discrete Crack material model is applied. This material model seperates the evaluation of the tensile and the shear behaviour. For the tensile softening behaviour Hordijk softening is used. For the shear a brittle model is applied where zero shear stiffness is used after tensile cracking. The two seperate material models are depicted in Fig. 3.4. The details of the material model are given in Table 3.4.

Element	Tensile strength $f_t\ [N/m^2]$	Mode-I fracture energy $G_{ft}\ [J/m^2]$
Line interface (L16IF)	0.45×10^6	35

Table 3.4: Material parameters for Discrete Crack material model for line interface elements (L16IF).

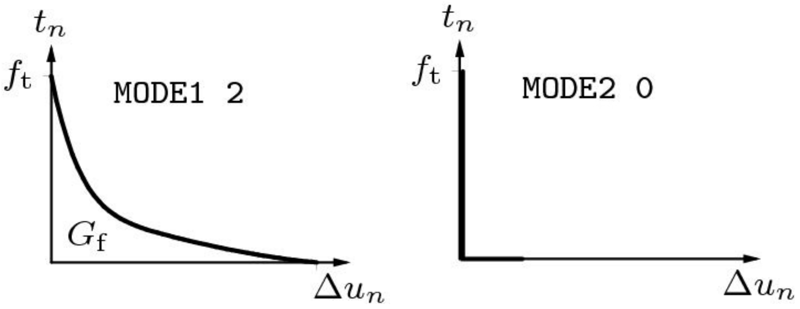

Figure 3.4: Discrete Crack material model, tensile and shear behaviour.

3.5 Loads

Self-weight, an overburden force and an imposed horizontal displacement are applied on this model. The overburden applied is equal to the 0.15 MPa overburden applied to Specimen 8. The details of the loads applied on the model are presented in Table 3.5 for the static analysis.

Order of application	Type of load	Point of application	Amount (steps)	Direction
1	Self-weight	-	9.81 m/s^2 (1)	-y
1	Displacement	Node 6	15.675 kN (1)	-y
2	Displacement	Node 2	1.0×10^{-5} m (500), 1.0×10^{-4} m (100)	x

Table 3.5: Applied loads on Discrete Crack Model during static analysis.

1.0E-5(500) 1.0E-4(100)

3.6 Convergence Criteria

For the static three convergence criteria have been specified. The incremental step is converged if all three criteria are simultaneously met. The iteration method continuous with the next step if the criteria are not met and the maximum number of iterations is reached. Only when the intermediate solution diverges the calculation is aborted.

Details on the convergence criteria are specified in Table 3.6.

Method	Convergence norm	Rel. convergence tolerance
Newton-Raphson	Displacement	$1.0 \cdot 10^{-3}$
"	Force	$1.0 \cdot 10^{-3}$

Table 3.6: Details on convergence criteria of Discrete Crack Model.

3.7 *Static Analysis*

Load-displacement The results of the static analysis and displayed in Fig. 3.6, where the load at mid-height is plotted against the deformation at mid-height. Also the results from the previous chapter are shown. The maximum capacity of the wall is accurately approximated. However, it is difficult to find the post-peak resistance with a linearized stiffness relation. Since the vertical part is essential to find the correct resistance the error made here can only be small. It is however also the hardest part to find convergence.

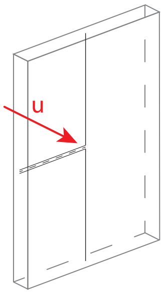

Figure 3.5: Loading direction for static analysis of Discrete Crack Model.

Convergence In Fig. 2.10 the convergence plot from the loading part of the analysis. No convergence is found at the point where the wall cracks. This can be explained with the moment-rotation diagram for this normal force given in Fig. 2.6 in which a big snap-back can be found. With a displacement based analysis it is not possible to find convergence in those steps. Luckily convergence is quickly found again.

Deformation From the deformed shape (Fig. 3.8) it can be concluded that the non-linear spring behaves as expected, first stiff while all the deformation in the wall is caused by bending of the beam elements and after cracking the beam elements relax and the rotation is transferred to the interface element. In the last point in can be found that all the deformation is caused by rotation of the interface.

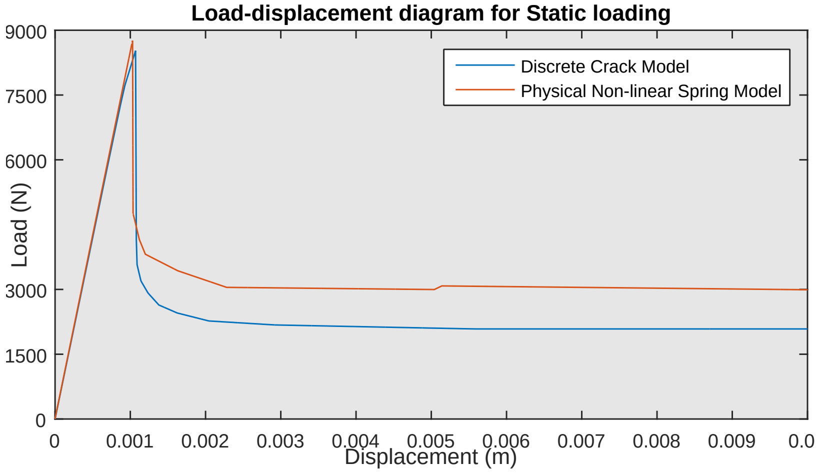

Figure 3.6: Load-displacement diagram from static analysis of Discrete Crack Model.

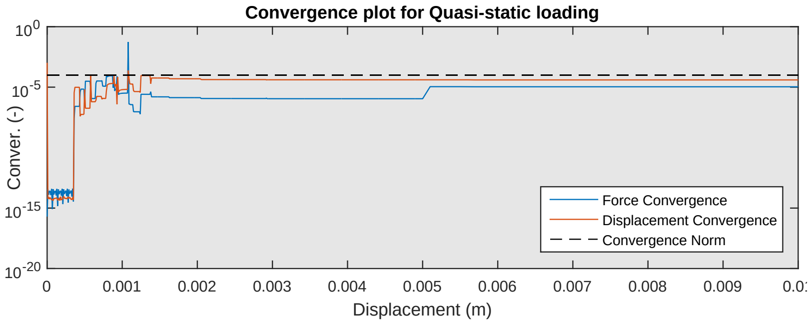

Figure 3.7: Convergence plots from static analysis of Discrete Crack Model.

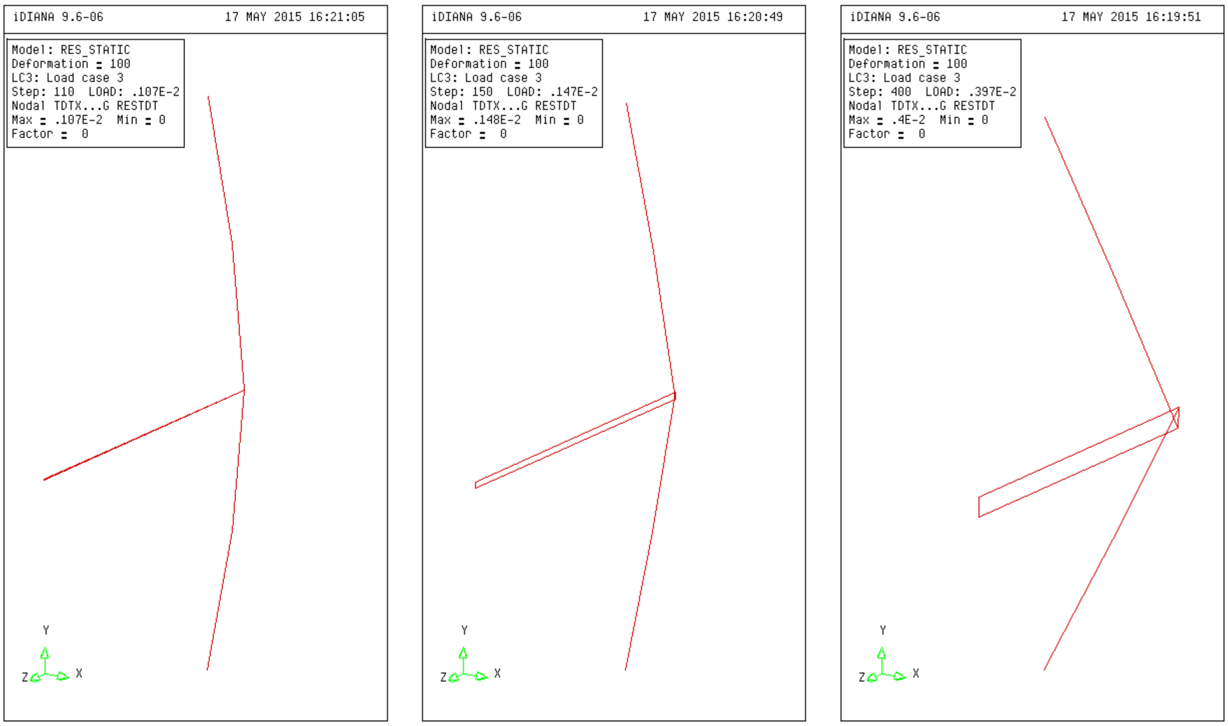

Figure 3.8: Deformation plots from static analysis of Discrete Crack Model

3.8 *Conclusion*

In this chapter the material model was applied using the Discrete Crack model from DIANA. The results are similar to the results of the Physical Non-linear Spring model. This confirms the correct interpretation of the formation of the crack during ouf-of-plane bending of masonry walls.

The line interface element shall be used in the Curved Shell Model where the geometric and physical non-linear behaviour is combined. The next chapter will focus only on the geometric non-linear effects.

4

Geometrical Non-linear Spring Model

To implement the geometric effects of the wall rocking on it's bricks the Geometric Non-linear Spring Model is developed. The main goal of this model is to investigate geometric non-linear effects during transient excitation. Since in the experiments of Doherty only cracked walls are considered for transient excitation tests this model does not have the cracking properties of the previous chapters.

Instead non-linear springs are used at mid-height and the two boundaries to restrict the wall from any behaviour except the rocking behaviour. At each tip a horizontal and a vertical spring is used which is very stiff when loaded in compression but has a low stiffness in tension. This allows the rocking motion but prevents divergence. The loads applied to this model are static forces as well as acceleration signals applied to the base of the model.

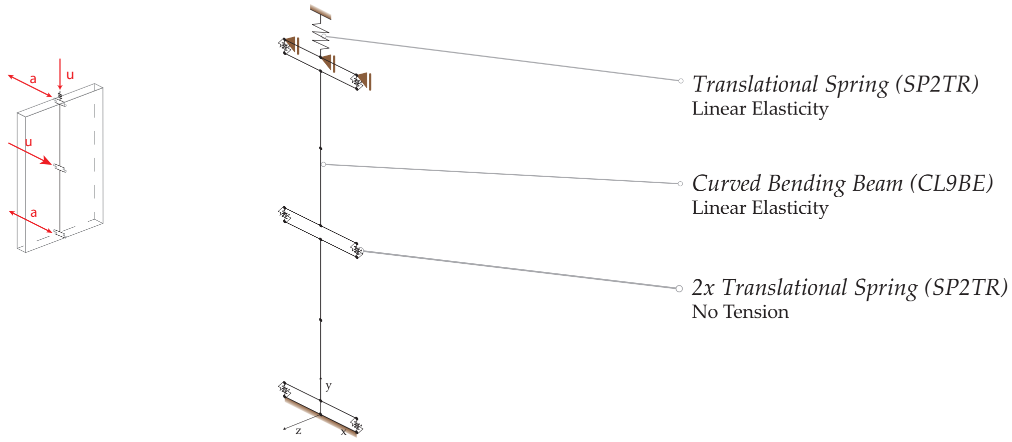

Figure 4.1: Schematized representation of the Non-Linear Spring Model.

4.1 *Discretization*

The wall is discretized using two rigid beam elements. The cracked cross-section and the top and bottom boundary cannot be modelled as a hinges since the thickness of the wall is important for the stabilising moment due to the overburden load and self-weight. Therefore a set of elements is assembled to obtain the preferred behaviour.

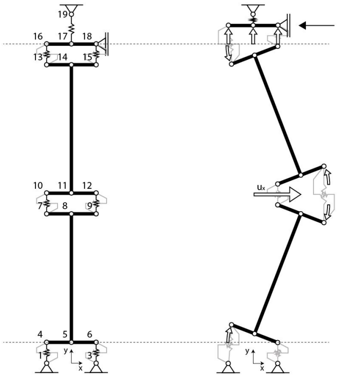

Figure 4.2: Discretization of URM wall to GNL spring model.

Elements representing cracked cross-section At the cracked cross-section the wall can rotate around the two edges of the wall. Two stiff elements are used to model the surfaces of the cracked interface over the thickness of the wall, see Fig. 4.3. We assume that the cross-section is totally cracked and no crushing will occur. Therefore the left and right edges are connected using to vertical compression-only springs. This makes it possible for the cross-section to transfer the overburden force and self-weight via one or two springs depending on the displacements. Since only rotations are allowed around the two edges the horizontal displacement of the edge nodes are restricted as well.

Uncracked cross-section This model can later be used in a physical and geometrical non-linear analysis by using the non-linear rotation spring which accounts for the elastic bending of the wall as well as the cracking and crushing. Since the displacements until cracking are small the geometrical non-linear effects of elastic deformation are small and the rigid element assumption is justified. The rotation spring can be attached to the mid-nodes of the cracked cross-section.

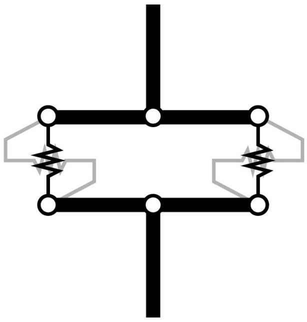

Figure 4.3: Set of elements representing a cracked cross-section.

4.2 *Geometry*

The typical dimensions are presented in Table 4.1.

Dimension			Beam Element (L6BEN)	Rotational Spring (SP2RO)
Length	l	$[m]$	0.75	0
Area	A	$[m^2]$	1.0	1.0

Table 4.1: Typical dimensions of the elements in Geometric Non-linear Spring Model.

4.3 *Boundary Conditions*

Bottom constraint The bottom constraint in Doherty's test setup a sliding constraint with a horizontal friction constraint. In this model this friction is assumed to be satisfying to constraint the wall and thus a hinged constraint is applied. Since the wall will rotate around its edges the cracked cross-section setup as explained above is also implemented for this constraint.

Top constraint For the top constraint the horizontal displacement is restricted by Doherty using angle cleats which allows the wall to rotate. A vertical overburden is applied using six springs connected to a horizontal plate. The wall can rotate around its edges over the plate as with the bottom constraint. The horizontal plate is constraint in the horizontal direction, the vertical displacement of its three nodes are tied together. The middle node is supported by a vertical spring with a stiffness equivalent to the six springs in Doherty's setup.

The overburden stress is applied by a prescribed displacement of the top node which induces a force in the top boundary constraint spring. This prescribed displacement is equal to,

$$u_y = \frac{N}{k} = \frac{16500N}{9.5 \cdot 10^5 N/m} = -0.017m$$

The boundary conditions are summarized Table 4.2.

Set	Node nr.	u_x	u_y	u_z	ϕ_x	ϕ_y	ϕ_z
Top node	4	✓	✓	✓	-	-	-
Bottom node	1	✓	-	✓	-	-	-

Table 4.2: Boundary conditions of the Geometric Non-linear Spring Model.

4.4 *Material properties*

Due to the rigid element assumption the Youngs's modulus applied is 1000 times larger and the Poisson ratio is set to zero.

Element	Mass density $[kg/m^3]$	Young's Modulus $[N/m^2]$	Poisson's Ratio $[-]$	Spring Stiffness $[N/m]$
Rigid Beams (L6BEN)	1800	$9.4 \cdot 10^9$	0.1	-
Rigid CS (CL9BE)	0	$9.4 \cdot 10^{12}$	0.1	-
Vert. CS Springs (SP2TR)	-	-	-	$9.4 \cdot 10^{12}$
Hor. CS Springs (SP2TR)	-	-	-	$9.4 \cdot 10^{12}$
Top BC Spring (SP2TR)	-	-	-	$9.6 \cdot 10^5$

Table 4.3: Material parameters applied in GNL Model with Springs.

Rayleigh damping is applied. The Rayleigh coefficient are derivated using the eigenfrequencies from the response of the cracked wall as reported by Doherty. The calculation of the coefficients is obtained from the Modal Analysis which is reported in Section 4.8

Damping ratio $[-]$	Mass coefficient $[1/s]$	Spring coefficient $[s]$
0.1	0.178	0.013

Table 4.4: Rayleigh Damping coefficients applied on GNL Model with Springs.

4.5 Loads

Self-weight, overburden stress, horizontal displacement and base acceleration are applied on this model in different analyses. The details of the loads applied on the model for the static analysis are combined in Table 4.5 and for the transient analysis in Table 4.6.

Order of application	Type of load	Point of application	Amount	Load steps	Direction
1	Self-weight	-	-	1	-y
1	Displacement	Node 19	-0.017 mm	1	y
2	Displacement	Node 11	0.5 mm	300	x

Table 4.5: Applied loads on GNL Test Model during static analysis.

Order of application	Type of load	Point of application	Amount	Load steps	Direction
1	Self-weight	-	-	1	-y
1	Base	Hor. supports	Load factors $\times g$	1241(0.01s)	x

Table 4.6: Applied loads on GNL Test Model during transient analysis.

Two load sets are used on specimen 12, the record of the Nahanni (NH) earthquake scaled from 100 to 400% and the El Centro (EL) earthquake scaled to 66%.

4.6 Convergence Criteria

The Newton-Raphson method is used to find equilibrium for each time step. A force norm convergence criteria is applied in this analysis. The details are given in Table 4.7.

Method	Convergence norm	Rel. convergence tolerance	Rel. divergence tolerance
Newton-Raphson	Force	$1.0 \cdot 10^{-5}$	$1.0 \cdot 10^{4}$
"	Displacement	$1.0 \cdot 10^{-5}$	$1.0 \cdot 10^{4}$

Table 4.7: Details on convergence criteria of GNL Test Model for static analysis.

Method	Convergence norm	Rel. convergence tolerance
Newton-Raphson	Force	$1.0 \cdot 10^{-3}$
"	Displacement	$1.0 \cdot 10^{-3}$

Table 4.8: Details on convergence criteria of GNL Test Model for transient analysis.

4.7 Time Integration Method

The Newmark method is used for time integration.

Method	Step size	Remark
Newmark	1.0×10^{-3} s	$\gamma = \frac{1}{2}, \beta = \frac{1}{4}$

Table 4.9: Details on time integration method for GNL Model with Springs.

4.8 Modal analysis

A modal analysis is performed to check the validity of the finite element model. The eigenfrequency reported by Doherty is derived using beam theory. This results in a first eigenfrequency of 51.7 Hz.

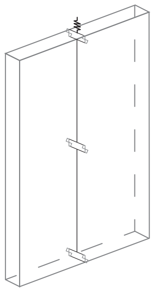

Figure 4.4: Modal analysis of Non-Linear Spring Model.

DIANA is only able to derive the eigenfrequencies from a linear stiffness matrix. Since non-linear material models are used to constrain non-rocking deformations these modes are not found. DIANA does have a function where the tangential stiffness matrix from a non-linear analysis is used, however, this function only uses the tangential stiffness matrix for one particular deformed state of the wall. Therefore the results still does not give accurate results for the eigenfrequencies and modes.

Eigenmodes and Eigenfrequencies The results of the linear modal analysis are given in Table 4.10 and Fig. 4.5a-d. As mentioned the eigenfrequencies are not accurate, the found results are too high frequencies. This is a result of the high compressive stiffness of the springs which is the initial state of the springs.

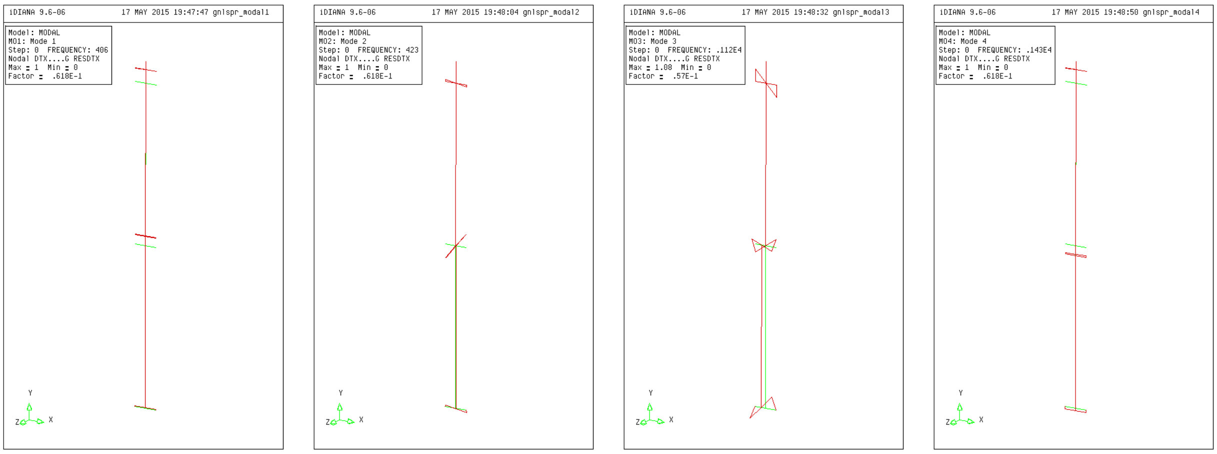

```
iDIANA 9.6-06            17 MAY 2015 19:47:47 gnlspr_modal1
Model: MODAL
M01: Mode 1
Step: 0  FREQUENCY: 406
Nodal DTX....G RESDTX
Max = 1  Min = 0
Factor =  .618E-1
```

```
iDIANA 9.6-06            17 MAY 2015 19:48:04 gnlspr_modal2
Model: MODAL
M02: Mode 2
Step: 0  FREQUENCY: 423
Nodal DTX....G RESDTX
Max = 1  Min = 0
Factor =  .618E-1
```

```
iDIANA 9.6-06            17 MAY 2015 19:48:32 gnlspr_modal3
Model: MODAL
M03: Mode 3
Step: 0  FREQUENCY: .112E4
Nodal DTX....G RESDTX
Max = 1.08  Min = 0
Factor =  .57E-1
```

```
iDIANA 9.6-06            17 MAY 2015 19:48:50 gnlspr_modal4
Model: MODAL
M04: Mode 4
Step: 0  FREQUENCY: .143E4
Nodal DTX....G RESDTX
Max = 1  Min = 0
Factor =  .618E-1
```

Figure 4.5: Eigenmodes of Non-Linear Spring Model

Eigenmode		1	2	3	4
Eigenfrequency	$[Hz]$	406	423	1125	1427

Table 4.10: Eigenfrequencies of Non-Linear Spring Model.

4.9 Static Analysis

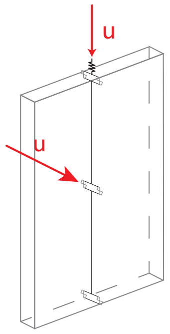

Figure 4.6: Loading direction for static analysis of Non-Linear Spring Model.

Load-displacement diagram The load-displacement diagram resulting from the geometric non-linear analysis is depicted in Fig. 4.7. In this figure the results of Doherty are depicted as well. The model can predict the initial resistance with a small error. This results from the undeformed situation and the initial overburden stress which is known. The behaviour for bigger displacements shows a bigger error. The experiment shows a higher resistance but it looks as if the ultimate displacement before failure will be smaller. This is probably the effect of crushing, which can be thought of as a shift of the point of rotation. This results in a smaller arm for the overburden force and thus an earlier collapse. The higher resistance can occur due to a greater vertical displacement during loading and thus a bigger overburden stress.

Overburden stress In Fig. 4.9 the development of the overburden force during the analysis is shown. As can be seen the overburden increases with almost 100%. Doherty also mentions this increase for 110 mm thick walls and states that an increase of more than 20% is not acceptable. Due to the big over shoot over the overburden stress it is arguable if this setup is a good representation of a real masonry wall, because the overburden rig is really stiff. In a building the floors can give some stiffness due to resisted deformation. Doherty does not validate the stiffness against real situations.

Convergence The analysis generally converges after 1 iteration. In load step 113 no convergence can be found after 30 iterations and the analysis is terminated. This is the point where the moment due to the vertical force becomes positive and thus the wall becomes unstable.

Deformation The deformation behaviour of the wall is as can be expected. The wall is tested with displacement in positive and negative direction, for which the resulting behaviour is similar. The cracked cross-sections behave as described in Section 4.1 and 4.A. See Fig. 4.10 for deformation plots.

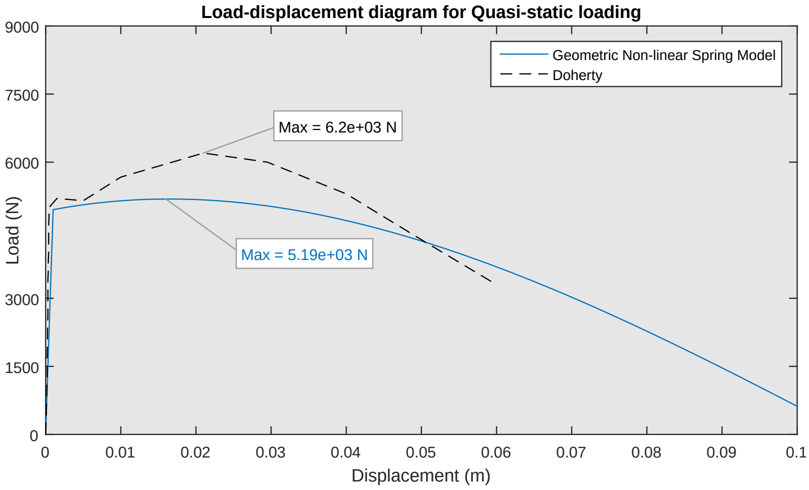

Figure 4.7: Load-displacement diagram from static analysis of Geometric Non-linear Spring Model.

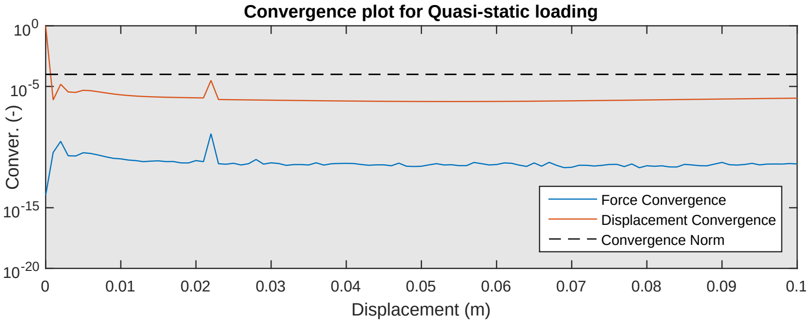

Figure 4.8: Convergence plots from static analysis of Geometric Non-linear Spring Model.

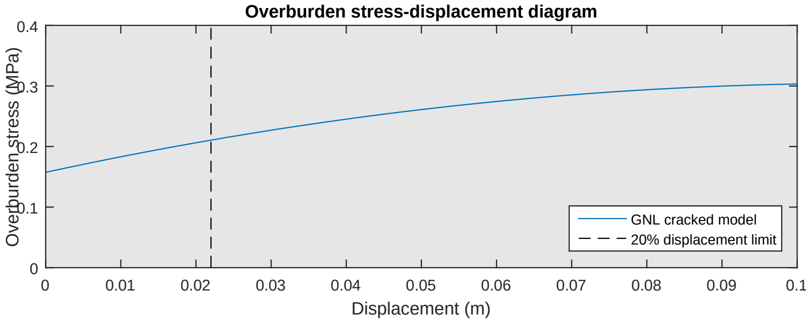

Figure 4.9: Overburden stress plotted increases due to rotating joints

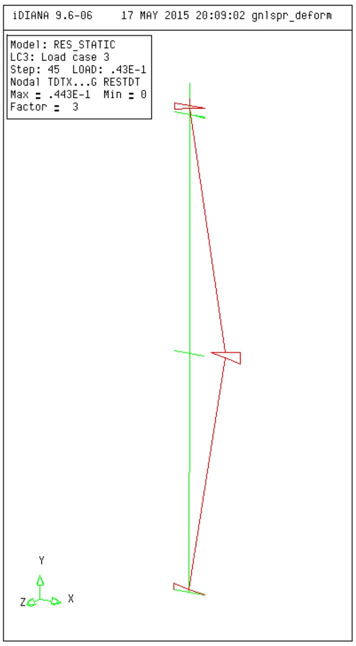

```
iDIANA 9.6-06     17 MAY 2015 20:09:02 gnlspr_deform
```

```
Model: RES_STATIC
LC3: Load case 3
Step: 45  LOAD: .43E-1
Nodal TDTX...G RESTDT
Max = .443E-1  Min = 0
Factor =  3
```

Figure 4.10: Deformations plot of Geometric Non-linear Spring Model.

4.10 *Transient Analysis*

A transient analysis is executed using recorded accelerations from seismic events. After optimizing the compressive stiffness and the thickness of the wall at mid-height the time-displacement diagram of Fig. 4.12 is obtained.

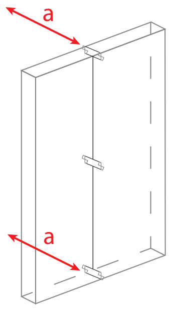

Figure 4.11: Loading direction for transient analysis of Non-Linear Spring Model.

Frequency In Fig. 4.13 the amplitude spectrum of the response is shown. This spectrum is the result of a Fast Fourier Transform and displays the absolute amplitude of the individual frequencies for a fourier series of the signal. The governing frequency is the frequency with the biggest amplitude and corresponds to the main rocking frequency. This governing frequency is very well approximated. However, the amplitude of the response is generally too big. This is also visible from the time-displacement diagram.

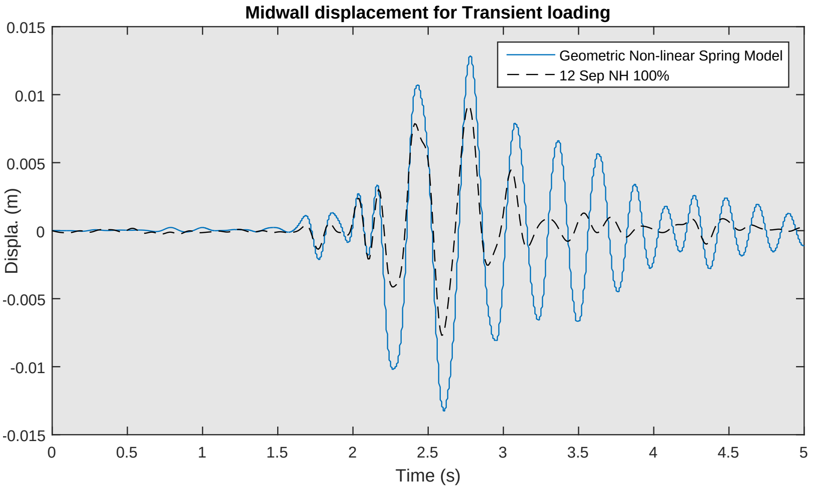

Figure 4.12: Load-displacement diagram from static analysis of Geometric Non-linear Spring Model.

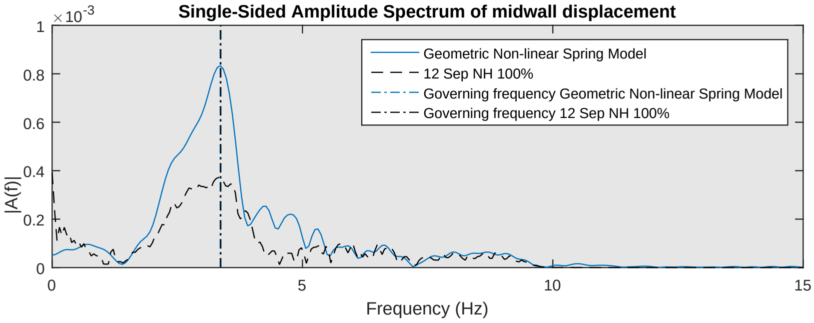

Figure 4.13: Frequency Amplitude Spectrum of Geometric Non-linear Spring Model with NH100% Specimen 12 acceleration input.

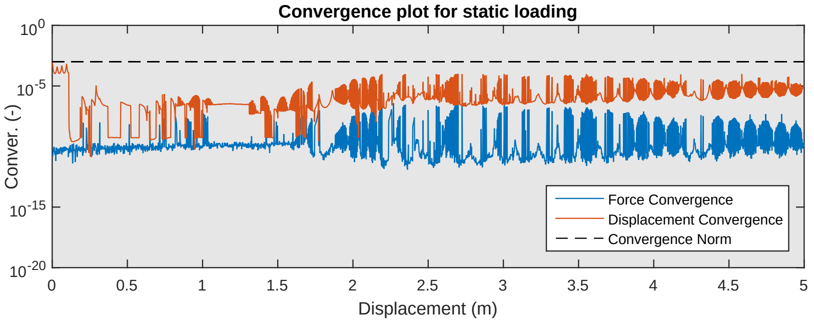

Figure 4.14: Convergence plots from static analysis of Geometric Non-linear Spring Model.

4.11 *Conclusion*

From the test model it can be concluded that the set of elements which make up the cracked cross-section do give a good representation of the geometric non-linear behaviour. It also gives an accurate result since the results found are almost exact the analytical derived values.

From the modal analysis of the full wall no good approximation is found for the first eigenmode and eigenfrequency. The found values are much higher than the analytical approximation reported by Doherty. This is due to the fact that DIANA can only calculate eigenmodes for tangential stiffness matrices of one particular deformed state. The first eigenmode shows the axial deformation of the wall which is not realistic as first eigenmode, although its high eigenfrequency is plausible.

From the GNL analysis of the full wall it can be concluded that a good approximation is obtained. The initial load is very well predicted. The peak resistance has an error of approximately 15%. The diagram shows the same increasing and decreasing behaviour which suggests that the model is good in the main properties.

4.A Test Model

The rocking behaviour is tested using a beam element of half the wall height and the cracked cross-section at the bottom support which only allows rocking behaviour, see Fig. 4.15. A vertical force is applied on top of the wall. All other material parameters, convergence criteria and boundary conditions are equal to the full model.

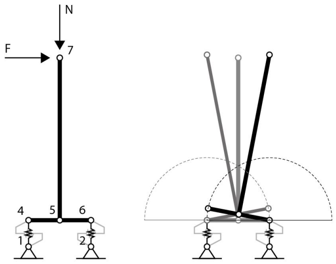

Figure 4.15: Test model of wall with cracked cross-section and allowable displacements.

Analytical derivation The horizontal force that can be applied is dependent on the arm of the vertical applied force, which is dependent on the horizontal displacement of the column via the rotation. The moment at which zero horizontal load can be applied is when the arm of the vertical force reduces to zero, thus at half of the thickness of the wall. Since the wall is rigid the relation should be linear. The maximum load resistance is equal to,

$$F = \frac{N \cdot t}{2 \cdot l} = \frac{200 \cdot 10^3 \cdot 110}{2 \cdot 750} = 14.667\ kN$$

Numerical load-displacement The results depicted in Fig. 4.18 show that the relation between the load and the displacement have the same value as the analytical derived values. It can thus be concluded that the cracked cross-section behaves as it should.

Full model It can be concluded that the cracked-cross section with non-linear springs does behave as expected. Since the total wall has two points of rotation a double ultimate displacement is expected as well as a double initial resistance due to a bigger arm.

Deformation The deformation behaviour of the wall is as can be aspected. The wall is tested with displacement in positive and negative direction, for which the resulting behaviour is similar. The cracked cross-sections behave as described in Section 4.1. See Fig. 4.16 and 4.17 for deformation plots.

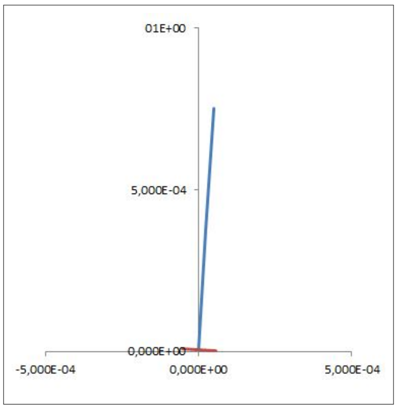

Figure 4.16: Total deformation.

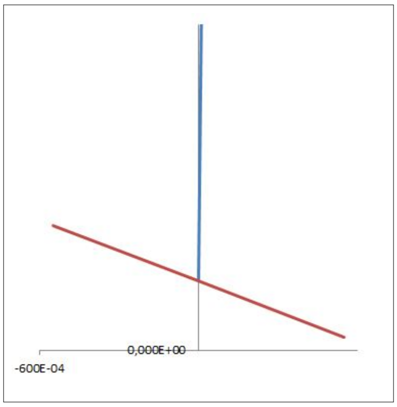

Figure 4.17: Deformation at bottom support (scale of horizontal and vertical different to show deformation)

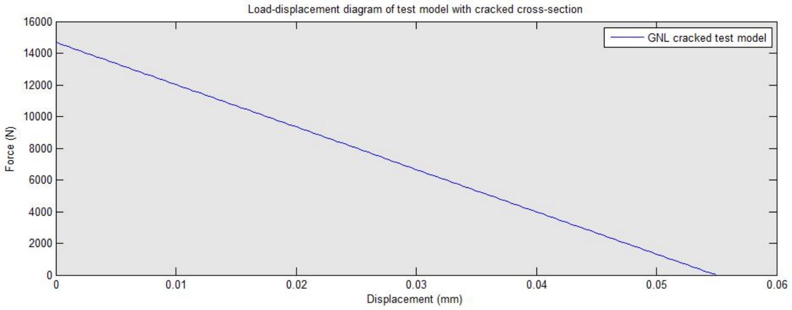

Figure 4.18: test

5

Physical and Geometrical Non-linear Interface Model

To combine the physical and the geometrical non-linear behaviour as a first step the Non-linear Interface Model, pictured in Fig 5.1, is developed. This model has two interface elements at mid-height of the wall in the thickness direction of the wall to which the discrete crack material model is applied. It thus combines the geometry of Chapter 4 with the material behaviour of Chapter 3.

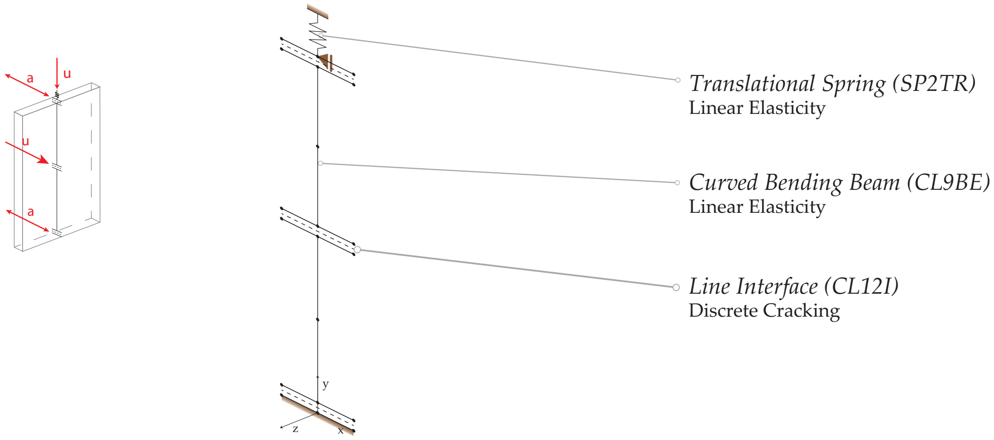

Translational Spring (SP2TR)
Linear Elasticity

Curved Bending Beam (CL9BE)
Linear Elasticity

Line Interface (CL12I)
Discrete Cracking

Figure 5.1: Schematized representation of the Non-Linear Interface Model.

5.1 Discretization

The model consists of two curved bending beam elements (CL9BE) and four line interface elements (CL12I), two at mid-height, one at the bottom and one at the top. The extra line interface at mid-height is used to have more integration points to model the cracking at mid-height more accurately. The overburden force is applied on the model using a translational spring (SP2TR).

The CL12I line interface element has 6 nodes with each 2 translational degrees of freedom. Six point Gauss integration has been applied along the length of the element to model the cracking of the wall accurately.

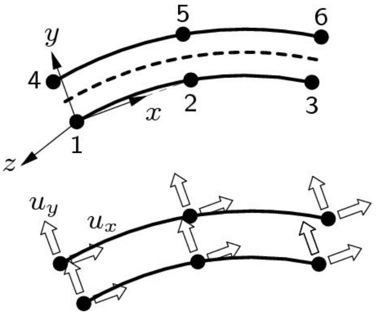

Figure 5.2: Line interface element (CL12I) (TNO DIANA BV, 2014)

All other elements have been discussed in previous chapters.

5.2 Geometry

The typical dimensions are presented in Table 5.1.

Dimension			Beam Element (CL9BE)	Line Interface (CL12I)	Translational Spring (SP2TR)
Thickness	t	$[m]$	-	0	-
Length	l	$[m]$	0.75	0.055	0.1
Width	b	$[m]$	-	0.95	-
Area	A	$[m^2]$	0.95×0.11	-	-

Table 5.1: Typical dimensions of the elements in Non-linear Interface Model.

5.3 Boundary Conditions

The wall is supported similar to the Non-linear Spring Model. At the bottom the wall has a 'rocking' support which is applied using a no-tension interface element. The bottom of the line interface is fully constraint.

The top of the wall is hinged in the experiment by two angle cleats which have some rotational freedom. The overburden rig however remains horizontal and thus rocks on the top of the wall. When both the top and the bottom of the interface element are horizontally supported the wall is overconstraint and gives a second resistance peak first observed in the model of Feenstra. This is explained in Sec. 5.A.

Set	Node nr.	u_x	u_y	ϕ_z
Bottom support	1-3	✓	✓	-
Top support	14	✓	-	-
Top node, overburden spring	19	✓	✓	-

Table 5.2: Boundary conditions of the Non-linear Interface Model.

5.4 *Material Properties*

Two material models are applied; Linear elasticity is applied to the bending beam elements and the discrete cracking material model is applied to the line interface elements. The general material properties per element type are presented in Table 5.3.

Element	Mass Density	Youngs Modulus	Poisson's Ratio	Stiffness
	$\rho\ [kg/m^3]$	$E\ [N/m^2]$	$\nu\ [-]$	$K\ /\ D_{STIF}$
Beam Elements (CL9BE)	1800	5.4×10^9	0.0	-
Line interface (CL12I)	-	-	-	$1.0 \times 10^{13}\ N/m^3$ ×
Overburden Spring (SP2TR)	-	-	-	$9.6 \times 10^5\ N/m$

Table 5.3: Material parameters applied in Non-Linear Interface Model.

× Discrete Crack model applied

On the mid-height line interface elements the Discrete Crack material model is applied. For the tensile softening behaviour Hordijk softening is applied, since this is most similar to exponential softening. For the shear a brittle model is applied where zero shear stiffness is used after tensile cracking. The two seperate material models are depicted in Fig. 3.4. The details of the material model are given in Table 3.4.

Element	Tensile strength	Mode-I fracture energy
	$f_t\ [N/m^2]$	$G_{ft}\ [J/m^2]$
Line interface (L16IF)	0.45×10^6	35

Table 5.4: Material parameters for Discrete Crack material model for line interface elements (CL12I).

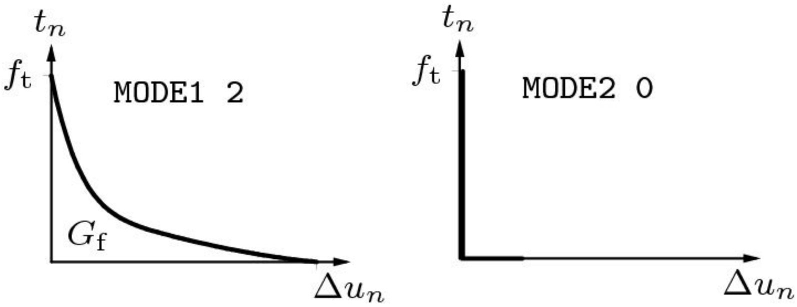

Figure 5.3: Discrete Crack material model, tensile and shear behaviour.

5.5 Loads

Self-weight, overburden stress, horizontal displacement and base acceleration are applied on this model in different analyses. The details of the loads applied on the model are presented in Table 5.5 for the static analysis and in Table 5.6 for the transient analysis.

Order of application	Type of load	Point of application	Amount (steps)	Direction
1	Self-weight	-	$9.81\ \mathrm{m/s^2}$ (1)	-y
2	Displacement	Node 19	-16.36×10^{-3} m (1)	y
3	Displacement	Node 11	1.0×10^{-5} m (95), 1.0×10^{-6} m (100), 1.0×10^{-3} m (100)	x

Table 5.5: Applied loads on Non-Linear Interface Model during static analysis.

Order of application	Type of load	Point of application	Amount (steps)	Direction
1	Self-weight	-	1	-y
2	Base	Hor. supports	Load factors $\times g$ (2500×0.002s)	x

Table 5.6: Applied loads on Non-Linear Interface Model during transient analysis.

Different sets of load factors are used, the record of the Nahanni (NH) earthquake scaled from 100 to 400% (Fig. 5.4) and the El Centro (EL) earthquake scaled to 66%.

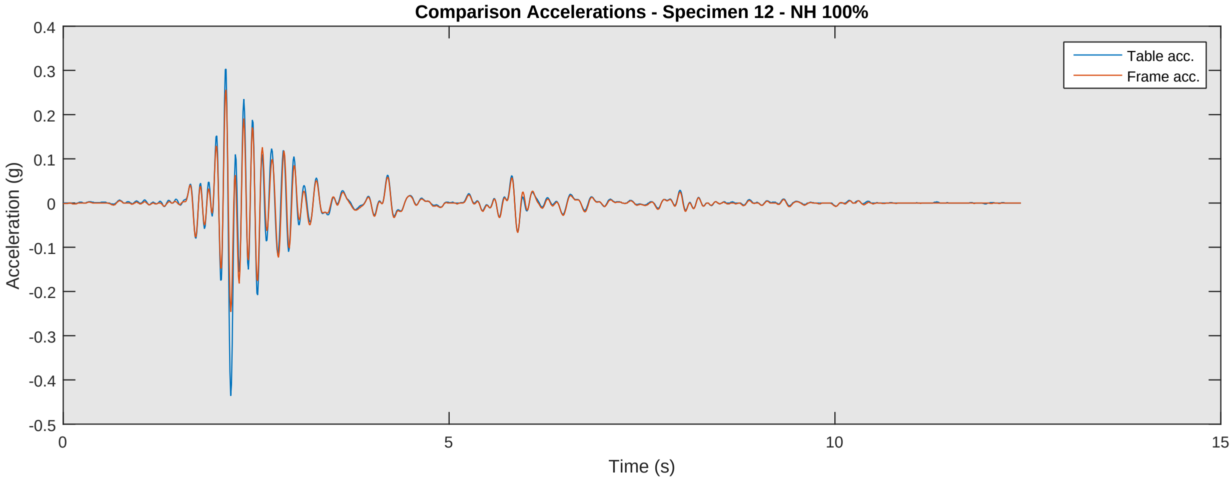

Figure 5.4: Nahanni earthquake acceleration signal (NH 100%).

5.6 *Convergence Criteria*

For the static and the transient analysis three convergence criteria have been specified. The incremental step is converged if all three criteria are simultaneously met. The iteration method continuous with the next step if the criteria are not met and the maximum number of iterations is reached. Only when the intermediate solution diverges the calculation is aborted.

Two iteration methods are used for the static analysis, full Newton-Raphson and the Secant iteration method. The Secant method is used for the second set of steps, 1.0×10^{-6} m (100). During these steps the wall cracks, when full Newton-Raphson is used divergence will occur. Although the convergence criteria are not met in this part of the analysis, see Fig. 5.9, the analysis can continue and after cracking the convergence criteria is met again. For the other sets of imposed displacement full Newton-Raphson gives convergence in the least amount of iterations.

Details on the convergence criteria are specified in Table 5.7 for the static analysis and Table 5.8 for the transient analysis.

Method	Convergence norm	Rel. convergence tolerance
Newton-Raphson / Secant ×	Displacement	$1.0 \cdot 10^{-4}$
"	Force	$1.0 \cdot 10^{-4}$
"	Energy	$1.0 \cdot 10^{-4}$

Table 5.7: Details on convergence criteria of Non-Linear Interface Model for static analysis.

× Secant method used for second set of imposed displacement on node 11.

Method	Convergence norm	Rel. convergence tolerance
Newton-Raphson	Displacement	$1.0 \cdot 10^{-3}$
"	Force	$1.0 \cdot 10^{-3}$
"	Energy	$1.0 \cdot 10^{-3}$

Table 5.8: Details on convergence criteria of Non-Linear Interface Model for transient analysis.

5.7 *Time Integration Method*

The Newmark method is used for time integration.

Method	Step size	Remark
Newmark	1.0×10^{-3} s	$\gamma = \frac{1}{2}, \beta = \frac{1}{4}$

Table 5.9: Details on time integration method for Non-Linear Interface Model with Springs.

(This page is left blank on purpose)

5.8 *Modal Analysis*

It was not possible to find the eigenfrequencies of the cracked wall. This is caused by the eigenfrequency analysis of DIANA. This uses the linear stiffness of the model to calculate the eigenvalues. Thus the cracks modelled by the interface elements with non-linear stiffness remain closed. The option to use a stiffness matrix from a non-linear analysis is not usefull since the time step which is chosen is arbitrary and gives no eigenfrequencies for and opened deformed state. Therefore the uncracked eigenfrequencies are presented below.

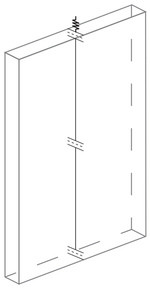

Figure 5.5: Modal analysis of Non-Linear Interface Model.

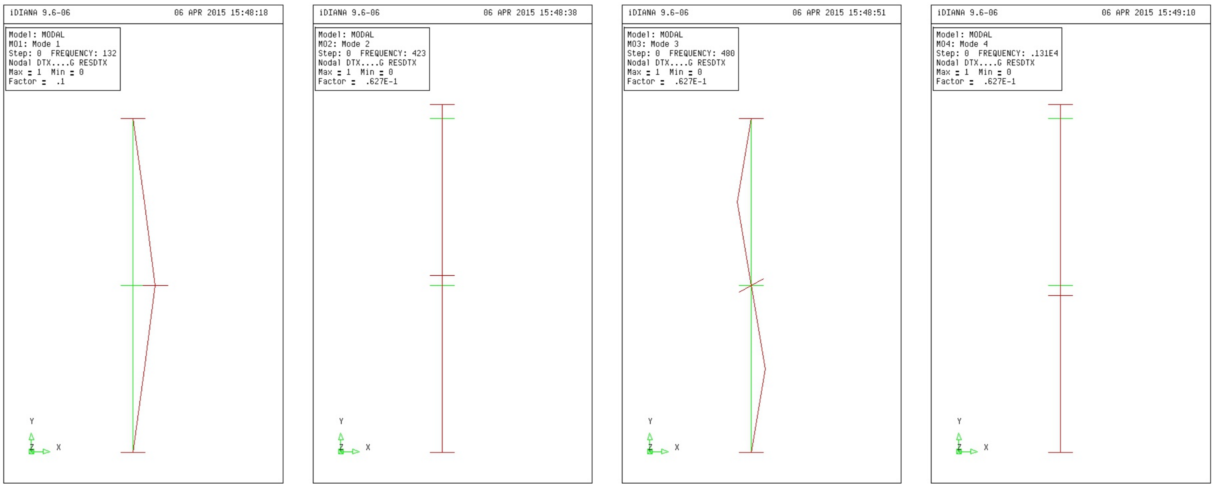

```
iDIANA 9.6-06                06 APR 2015 15:48:18
Model: MODAL
M01: Mode 1
Step: 0  FREQUENCY: 132
Nodal DTX....G RESDTX
Max = 1  Min = 0
Factor =  .1
```

```
iDIANA 9.6-06                06 APR 2015 15:48:38
Model: MODAL
M02: Mode 2
Step: 0  FREQUENCY: 423
Nodal DTX....G RESDTX
Max = 1  Min = 0
Factor =  .627E-1
```

```
iDIANA 9.6-06                06 APR 2015 15:48:51
Model: MODAL
M03: Mode 3
Step: 0  FREQUENCY: 480
Nodal DTX....G RESDTX
Max = 1  Min = 0
Factor =  .627E-1
```

```
iDIANA 9.6-06                06 APR 2015 15:49:10
Model: MODAL
M04: Mode 4
Step: 0  FREQUENCY: .131E4
Nodal DTX....G RESDTX
Max = 1  Min = 0
Factor =  .627E-1
```

Figure 5.6: First four eigenmodes of the uncracked Non-linear Interface Model.

Eigenmode		1	2	3	4
Eigenfrequency	$[Hz]$	131.6	422.8	479.7	1311

Table 5.10: Details on convergence criteria of Non-linear Interface Model.

Damping The Rayleigh damping coefficients are calculated from the first two eigenmodes with a damping percentage of 1%. The results are presented in Table 5.11.

Damping ratio	Mass coefficient	Spring coefficient
$[-]$	$[1/s]$	$[s]$
1%	0.150×10^{2}	0.221×10^{-5}

Table 5.11: Rayleigh damping coefficients applied on curved beam elements (CL9BE)

5.9 *Static Analysis*

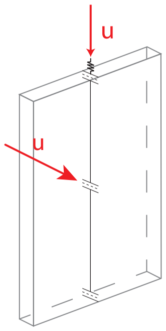

Figure 5.7: Loading direction in static analysis of Non-Linear Interface Model.

Load-displacement The results of the static analysis and displayed in Fig. 5.8, where the load at mid-height is plotted against the the deformation at mid-height. The initial peak overestimates the experimental value. The geometric initial resistance is equal to the found value. The post-peak behaviour is underestimated. This suggests that the stiffness of the overburden spring or the wall is underestimated.

Convergence In Fig. 5.9 the convergence plot from the loading part of the analysis is given. The convergence criteria is not met in two parts of the analysis. In the beginning the displacement criteria is not met due to small relative displacement norm when applying a step of zero displacement. Also after the peak both displacement and force criteria are not met. During the rest of the load steps both criteria are met and the number of iterations per step is low.

Deformation In the pre-cracking deformation plot (Fig. 5.10) both top and bottom interface element are opened, while the mid-height interface elements remain closed. The deformation of the beam is obtained by pure bending.

In the post-cracking deformation plot the mid-height interface elements are opened as well and thus fully cracked. The beam elements are not curved any more and thus all deformation is obtained from rotation around the mid-height crack.

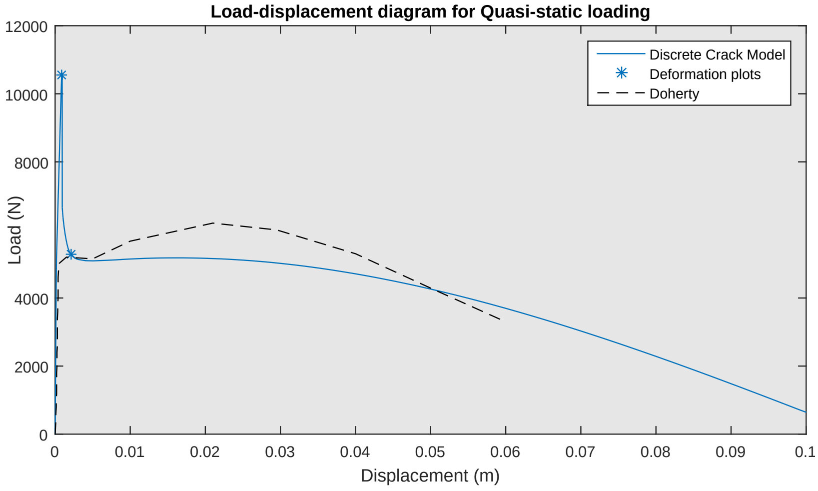

Figure 5.8: Load-displacement diagram from static analysis of Non-linear Interface Model.

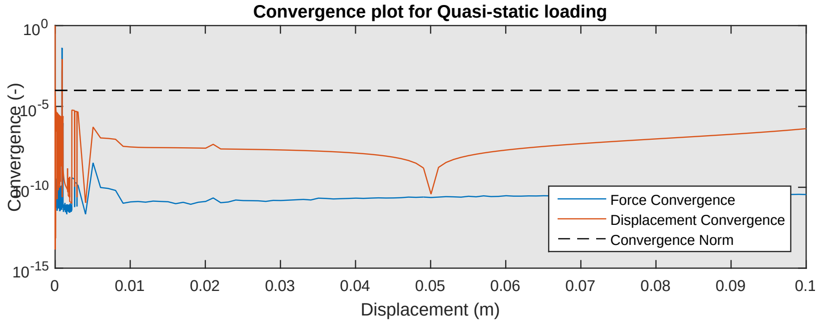

Figure 5.9: Convergence plots from static analysis of Non-linear Interface Model.

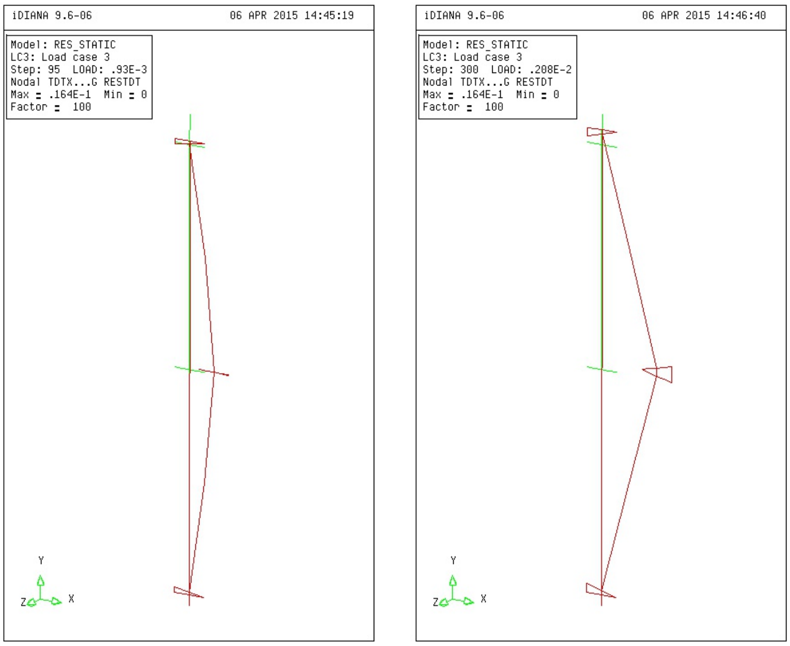

Figure 5.10: Deformation plots for precracked and postcracked state.

5.10 Transient Analysis

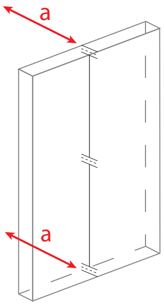

Figure 5.11: Loading direction in transient analysis of Non-Linear Interface Model.

Time-displacement The response of the Non-linear Interface Model to the Nahanni earthquake is given in Fig. 5.12. The amplitude of the response is about the same as the amplitude of the experiment. The governing frequency is somewhat lower than the governing frequency during the experiment.

A sensitivity analysis has been performed into several parameters of the model. The model is most sensitive to changes in interface stiffness, thickness and damping.

Convergence The convergence plots for the three convergence criteria applied is given in Fig. 5.14. The convergence norm is met for all steps.

Deformation The deformation plots (Fig. 5.15) for the transient analysis show that the line interface elements do not open, but deform in compression due to the low interface stiffness. The right figure shows the deformation for a bigger deformation and shows some opening of the crack. This interface behaviour is wrong but it results in global deformations of the right amplitude. This is equal to the observations made in Chapter 4.

5.11 Conclusion

The Non-linear Interface Model combines the physical and geometrical non-linear behaviour. It is however not able to find correct transient response with the same material properties for the static and transient analysis. The interface stiffness should be reduced to find the correct transient behaviour.

In the next Chapter the beam elements will be replaced by plane strain elements which will make it possible to more realistically model the behaviour of the wall over the thickness. With these elements the damage due to compression can be modelled.

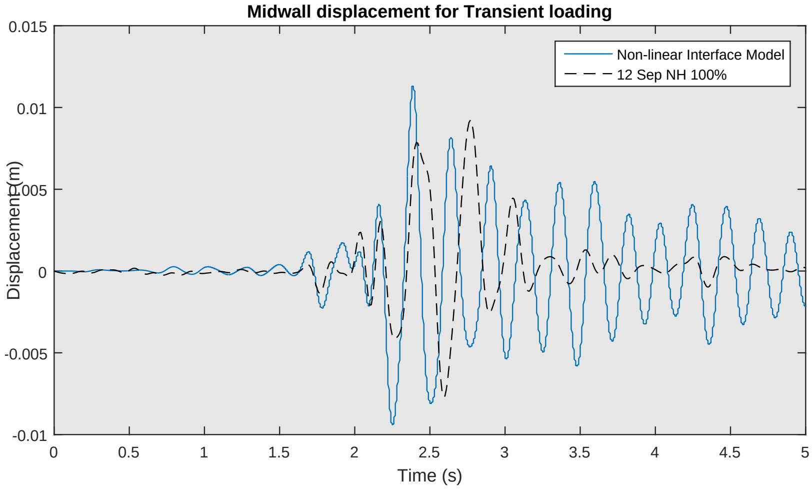

Figure 5.12: Time-displacement diagram from transient analysis of Non-linear Interface Model.

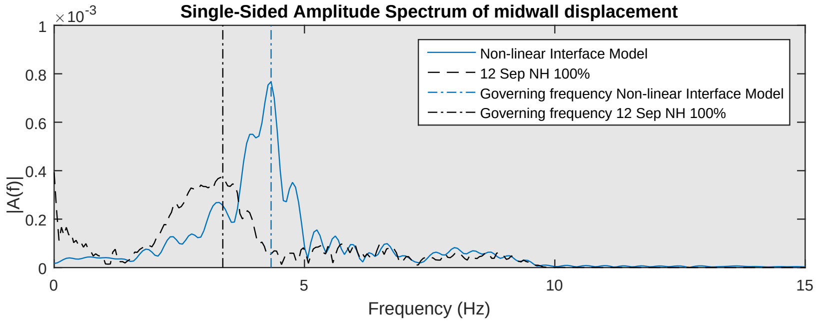

Figure 5.13: Frequency Amplitude Spectrum of Non-linear Interface Model with NH100% Specimen 12 acceleration input.

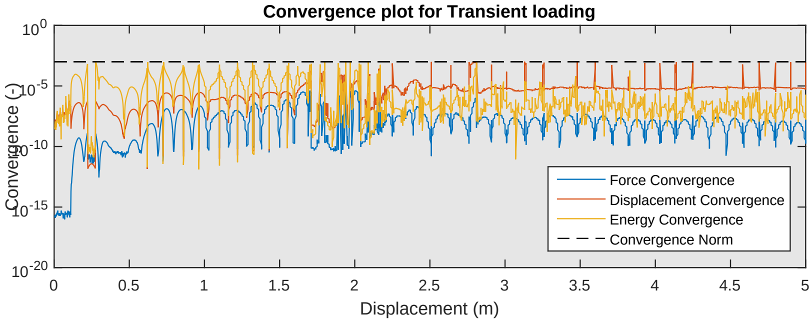

Figure 5.14: Convergence plots from transient analysis of Non-linear Interface Model.

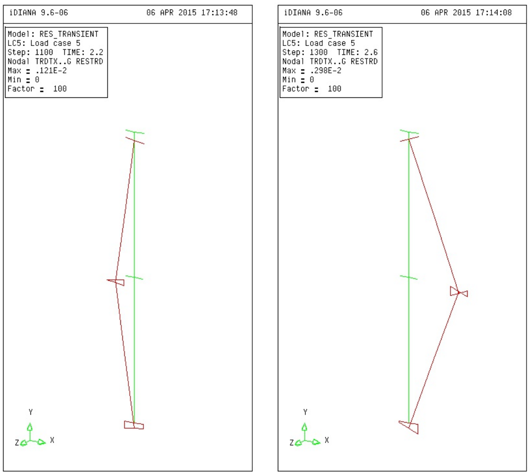

```
Model: RES_TRANSIENT
LC5: Load case 5
Step: 1100  TIME: 2.2
Nodal TRDTX..G RESTRD
Max = .121E-2
Min = 0
Factor =  100
```

```
Model: RES_TRANSIENT
LC5: Load case 5
Step: 1300  TIME: 2.6
Nodal TRDTX..G RESTRD
Max = .298E-2
Min = 0
Factor =  100
```

Figure 5.15: Deformation plots during transient analysis.

5.A Feenstra's Peak

Second peak In the Non-linear Interface Model, the Curved Shell Model, Feenstra's Hybrid model (Fig. 5.16), where 3D brick elements are used to apply the correct boundary conditions as explained in Sec. 5.3, and Feenstra's 3D Model a second resistance peak is observed at some greater displacements, see Fig. 5.19. This peak is clearly not a realistic effect, but is a results of confinement of the dummy members at the top support.

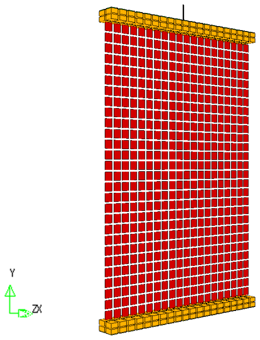

Figure 5.16: Shrink plot of Feenstra's Hybrid Model

In Fig. 5.17 the origin of the problem is schematically shown. The top of the wall is displayed with two stiff dummy members and an interface element in between. The bottom dummy member is rigidly connected to the beam element which resembles the wall. The top dummy member is supported in horizontal direction to prevent rotation of the element which resembles the overburden rig that also cannot rotate. The middle node of the bottom dummy member is constraint in the horizontal direction since the wall is supported here with two angle cleats.

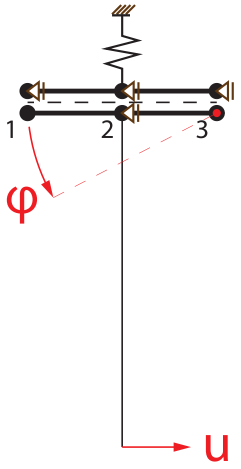

Figure 5.17: Shrink plot of Feenstra's Hybrid Model

When the wall deforms the bottom dummy member starts to rotate around node 3 since the interface element has a compressive stress here which causes the shear stiffness to be high. The rotation causes a vertical and small horizontal displacement of nodes 1 and 2. However the horizontal displacement of node 2 is constraint. This causes the dummy member 2-3 to be elongated, see Fig. 5.18, which creates an extra resistance against rotation and thus bigger capacity.

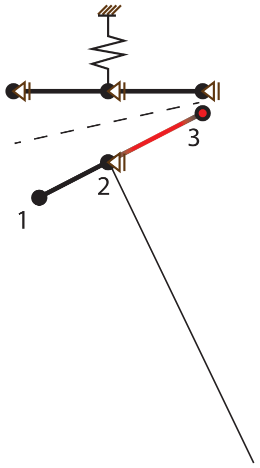

Figure 5.18: Shrink plot of Feenstra's Hybrid Model

The solution is to remove the horizontal constraint of the top side of the interface element. This results in a load-displacement diagram similar to experimental research, see Fig. 5.8.

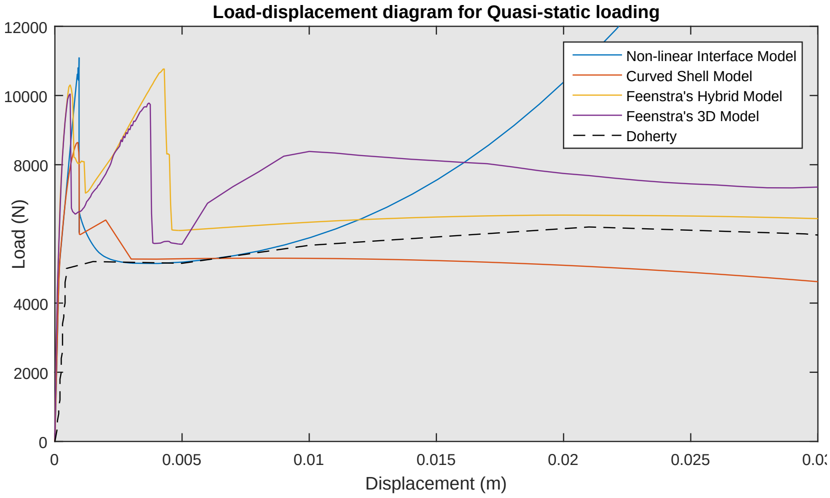

Figure 5.19: Load-displacement diagram of four models all showing some kind of Feenstra's Peak

6
Plane Strain Model

To study the importance of the thickness direction of the wall in more detail a plane strain model is used. This model uses plane strain elements over the thickness of the wall. Since no strain is allowed in the longitudinal direction of the wall it is effectively an infinite wall. This model is used as an alternative to the use of 3D brick elements.

The plane strain elements should be able to model the damage done to the wall during static loading. For this purpose a phased analysis was performed.

Furthermore the cracking load needed to initially crack the wall is investigated with an increasing number of elements. With this the minimum number of integration points over the thickness for the Curved Shell Model can be determined.

Finally, the deformation of the wall during rocking is investigated. This can have an effect on the validity of the Curved Shell Model since the shell elements are based on Euler-Bernoulli's hypothesis.

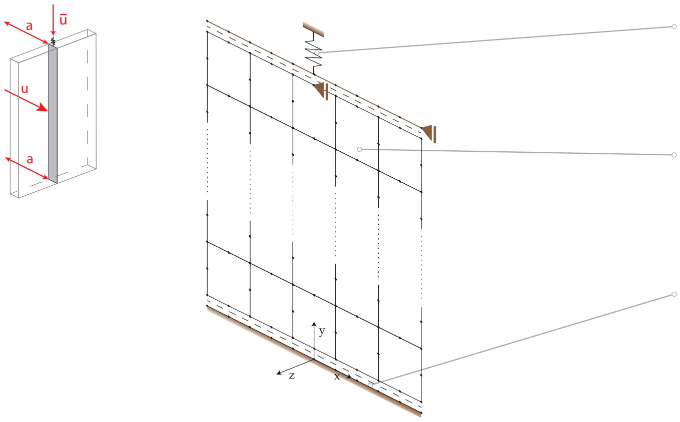

Translational spring (SP2TR)
Linear elasticity

Plane Strain quadrilateral (CQ16E)
Total strain rotating crack

Line interface (CL12I)
No-tension

Figure 6.1: Schematized representation of the Plane Strain Model.

6.1 Discretization

The model consists of plane strain elements (CQ16E) and line interface elements (CL12I). The overburden force is applied on the model using a translational spring (SP2TR).

To model the wall as a true one-way bending wall plane strain elements are used. These have no strain in the direction normal to their plane, thus as if an infinite wall was modelled. The element has eight nodes and quadratic interpolation is applied. Per node it has two translational degrees of freedom in-plane, u_x and u_y.

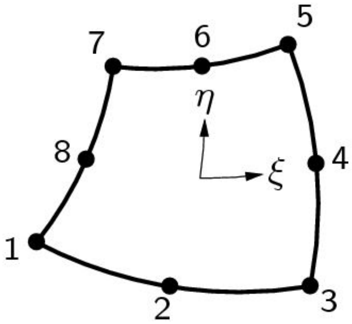

Figure 6.2: Plane strain element (CQ16E) (TNO DIANA BV, 2014)

The wall is subdivided in 5 × 16 plane strain elements. At mid-height one element row is split in two to make the addition of a line interface possible, which is done for the transient analysis. At the top and the bottom a line interface is implemented for the rocking behaviour.

6.2 Geometry

From the discretization the typical dimensions of the elements are presented in Table 6.1.

Dimension			Plane Strain (CQ16E)	Overburden Spring (SP2TR)	Line interface (CL12I)
Thickness	t	$[m]$	0.95	-	0.95
Width / Length	b/l	$[m]$	0.022	0.1	0.022
Height	l	$[m]$	0.02	-	0

Table 6.1: Typical dimensions of the elements in Plane Strain Model.

6.3 Boundary Conditions

The wall is supported at top and bottom, see Table 6.2 and Fig. 6.1.

At the bottom the interface nodes that are not connected to the plane strain elements are constraint in x- and y-direction.

At the top the non-connected line interface nodes are tied in the vertical direction, this means that vertical displacement of one of the nodes has a direction effect on the overburden spring. The middle section of the wall is supported in the horizontal direction. In the experimental setup the wall the supported by two angle cleats, these also allow some unknown quantity of rotation but prevent horizontal displacement.

Set	Node nr.	u_x	u_y	ϕ_z
Top node	1152	✓	✓	-
Bottom node	1 201 401 ... 2001	✓	-	-

Table 6.2: Boundary conditions of the Plane Strain Model.

6.4 *Material Properties*

Two material models are applied; the Total Strain Rotating Crack model is applied to the plane strain elements and the no-tension material model is applied to the line interface elements. The general material properties per element type are presented in Table 6.3.

Element	Mass Density ρ $[kg/m^3]$	Youngs Modulus E $[N/m^2]$	Poisson's Ratio ν $[-]$	Stiffness K / D_{STIF} $[-]$
Plane strain element (CQ16E)	1800	5.4×10^9 * 11.6×10^9 **	0.0	-
Overburden spring (SP2TR)	0	-	-	1.01×10^5 N/m
Line interface (CL12I)	0	-	-	1.0×10^{13} N/m^3 $^{*\,\times}$ 1.0×10^8 N/m^3 $^{**\,\times}$

Table 6.3: Material parameters applied in Plane Strain Model.

* For specimen 8
** For specimen 12
$^{\times}$ Non-linear material model applied, see Fig. **??**

On the plane strain elements the Total Strain Rotating Crack material model is applied. For the tensile softening an exponential decay is enforced and in compression parabolic hardening followed by exponential softening. The details of the material model are given in Table 6.4.

Element	Tensile strength f_t $[N/m^2]$	Mode-I fracture energy G_{ft} $[J/m^2]$	Compressive strength f_c $[N/m^2]$	Compressive fracture energy G_c $[J/m^2]$	Shear retension factor β $[-]$
Plane strain element (CQ16E)	0.3×10^6 * 0.45×10^6 **	35	4.41×10^6	5000	0.01

Table 6.4: Material parameters for Total Crack Rotating Strain material model for plane strain elements (CQ16E).

* For specimen 8
** For specimen 12

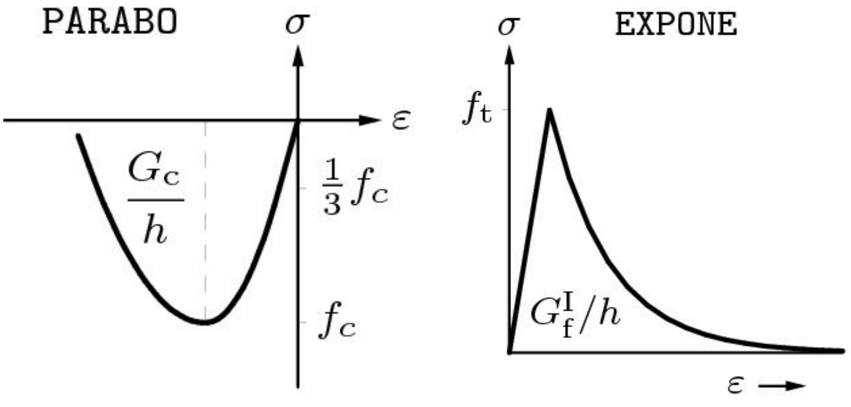

Figure 6.3: Stress-strain relations in compression and tension of the Total Strain Rotating Crack material model applied on the Plane Strain Model.

6.5 Loads

Self-weight, overburden stress, imposed horizontal displacement and base acceleration are applied on this model in different analyses. The details of the loads applied on the model are presented in Table 6.5 for the static analysis and in Table 6.6 for the transient analysis.

Order of application	Type of load	Point of application	Amount (steps)	Direction
1	Self-weight	-	1	-y
2	Displacement	Node 1154	-16.36×10^{-3} m (1)	y
3	Displacement	Node 78	0.5×10^{-6} m (300), 0.2×10^{-4} m (267)	x

Table 6.5: Applied loads on Plane Strain Model during static analysis.

Order of application	Type of load	Point of application	Amount (steps)	Direction
1	Self-weight	-	1	-y
2	Base	Hor. supports	Load factors $\times g$ (2500×0.002s)	x

Table 6.6: Applied loads on Plane Strain Model during transient analysis.

Different sets of load factors are used, the record of the Nahanni (NH) earthquake scaled from 100 to 400% (Fig. 5.4) and the El Centro (EL) earthquake scaled to 66%. The results presented in this chapter are response to the NH100% Specimen 12 signal (Fig. 5.4). The average acceleration of table and frame is used as input for the model.

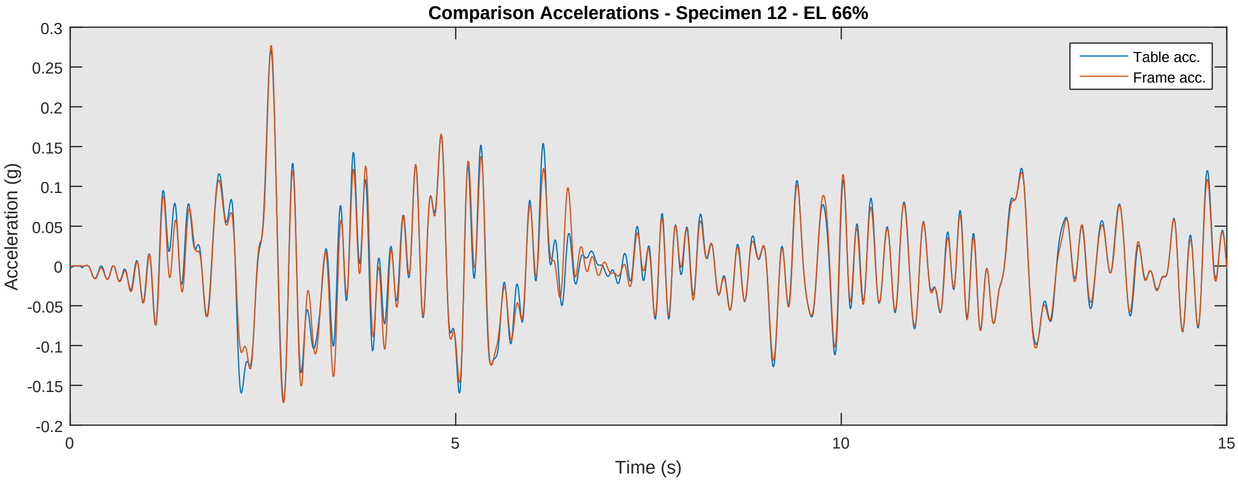

Figure 6.4: El Centro earthquake acceleration signal (EL 66%).

6.6 *Convergence Criteria*

For the static and the transient analyses three convergence criteria have been specified. The incremental step is converged if all three criteria are simultaneously met. However, the analysis will continue with the next step if the criteria are not met and the maximum number of iterations is reached. Only when the intermediate iteration diverges will the calculation be aborted.

Details on the convergence criteria are specified in Table 6.7 for the static analysis and Table 6.8 for the transient analysis.

Method	Convergence norm	Rel. convergence tolerance
Newton-Raphson	Displacement	$1.0 \cdot 10^{-4}$
"	Force	$1.0 \cdot 10^{-4}$
"	Energy	$1.0 \cdot 10^{-4}$

Table 6.7: Details on convergence criteria of Plane Strain Model for static analysis.

Method	Convergence norm	Rel. convergence tolerance
Newton-Raphson	Displacement	$1.0 \cdot 10^{-4}$
"	Force	$1.0 \cdot 10^{-4}$
"	Energy	$1.0 \cdot 10^{-4}$

Table 6.8: Details on convergence criteria of Plane Strain Model for transient analysis.

In Sections 6.9 and 6.10 convergence plots are shown. In these plots for each step the convergence of the three criteria of the last iteration is given. Also the norm is presented to show if the norm is met.

6.7 *Time Integration Method*

The Backward Euler integration scheme is used for time integration. This method is explained in the literature review. The stability of the solution during time integration is dependent on the step size and the method used.

Method	Step size	Remark
Backward Euler	2.0×10^{-3} s	-

Table 6.9: Details on time integration method for Plane Strain Model.

(This page is left blank on purpose)

6.8 *Modal Analysis*

It was not possible to find the eigenfrequencies of the cracked wall. This is caused by the eigenfrequency analysis of DIANA. This uses the linear stiffness of the model to calculate the eigenvalues. Thus the cracks modelled by the interface elements with non-linear stiffness remain closed. The option to use a stiffness matrix from a non-linear analysis is not usefull since the time step which is chosen is arbitrary and gives no eigenfrequencies for and opened deformed state. Therefore the uncracked eigenfrequencies are presented below.

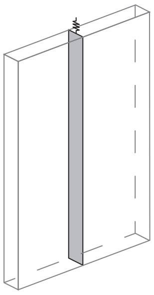

Figure 6.5: Modal analysis of Plane Strain Model.

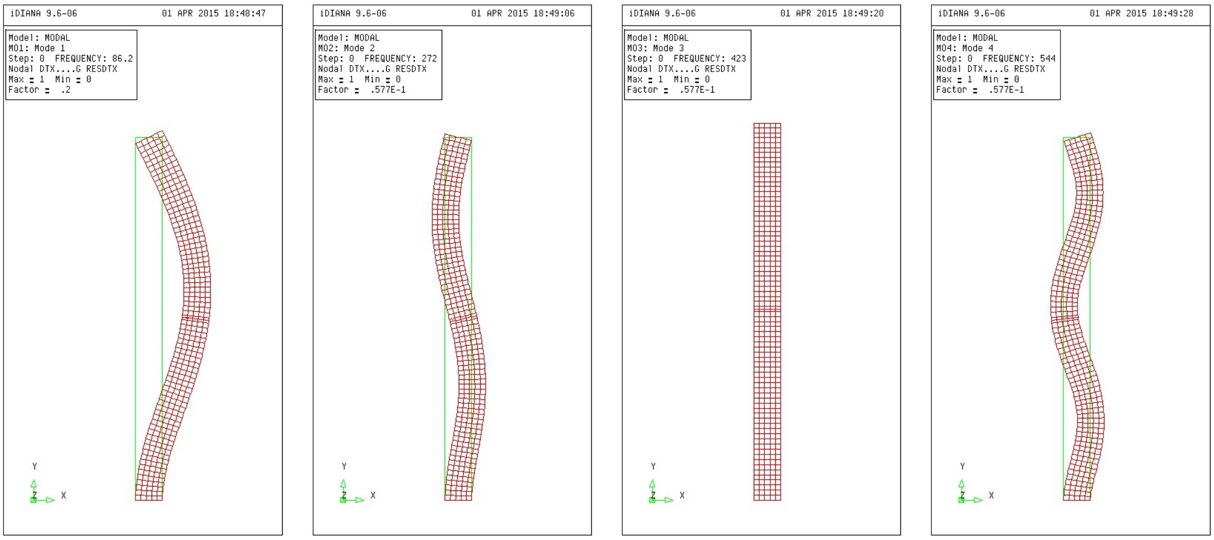

Figure 6.6: First four eigenmodes of the uncracked Plane Strain Model.

Eigenmode		1	2	3	4
Eigenfrequency	$[Hz]$	86.2	272	423	544

Table 6.10: Details on convergence criteria of Plane Strain Model.

Damping The Rayleigh damping coefficients are calculated from the first two eigenmodes with a damping percentage of 1%. The results are presented in Table 6.11.

Damping ratio	Mass coefficient	Spring coefficient
$[-]$	$[1/s]$	$[s]$
1%	0.671	0.142×10^{-4}

Table 6.11: Rayleigh damping coefficients applied on plane strain elements (CQ16E)

6.9 *Static Analysis*

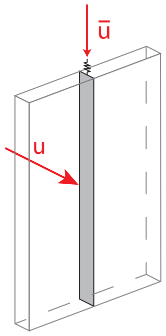

Figure 6.7: Loading direction in static analysis of Plane Strain Model.

For the static push test the plane strain model is used with smeared cracking. In the thesis report also result of static analysis are discussed for a plane strain model with an intermediate interface element and discrete cracking. For this model only the results are presented here.

Load-displacement For the static analysis the load displacement-diagram can be found in Fig. 6.8. The initial peak overestimates the results of Doherty slightly, the post-peak behaviour is underestimated. The increased results of Doherty are a result of the increase in the overburden force. This could be an effect of hardening of the overburden spring rig on which only the a static linear stiffness was given. The maximum capacity of the wall was found to be equal with respect to the results of ARUP.

Deformations From the deformation plot in Fig. 6.11 it can be observed that the mid-height elements all open and cracks are formed there. The Poisson ratio is set to zero to prevent splitting of the wall due to compressive forces in the toe and the top of the wall. From the crack planes given in the same figure it can be found that still crushing planes are formed in the compressive area's.

Cracks In Fig. 6.10 the total number of cracks is shown. If compared with the convergence plot it is clear that were no convergence was found this was caused by a big increase in the number of cracks. In the crack plots 6.11 it is clear that the cracks are widely distributed over the height of the wall. However, after enough deformation the cracks seem to centrtalise at mid-height which is visible form the last figure where the strain is plotted over the height of the wall.

Convergence The convergence plot in Fig. 6.9 shows the convergence of the last iteration per load step. It is clear that no convergence is obtained for every step although the maximum number of iterations was increased and the step size was reduced. However when compared with results form the Curved Shell Model as well as with model with interface elements and discrete cracking (see Fig. 7.7) it can be concluded that the error as a result of the non-convergence is negligible. Since the relative change of the force/displacement between iterations is small due to the small step size, the error is small if the convergence rate does not become too big.

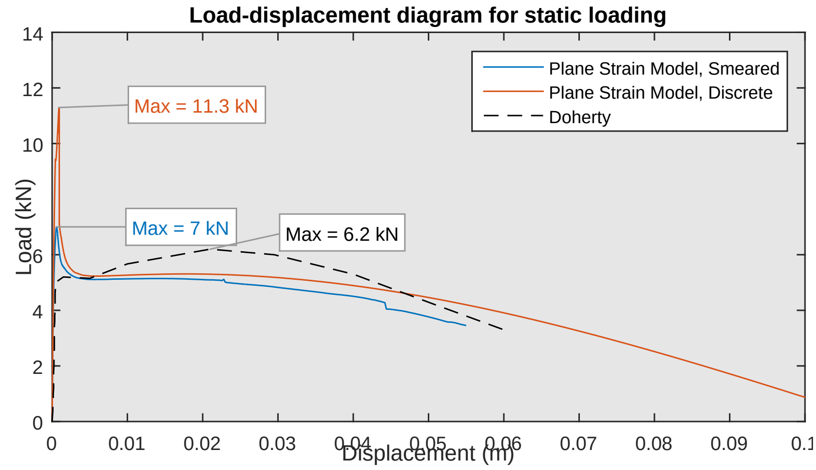

Figure 6.8: Load-displacement diagram from static analysis of Plane Strain Model.

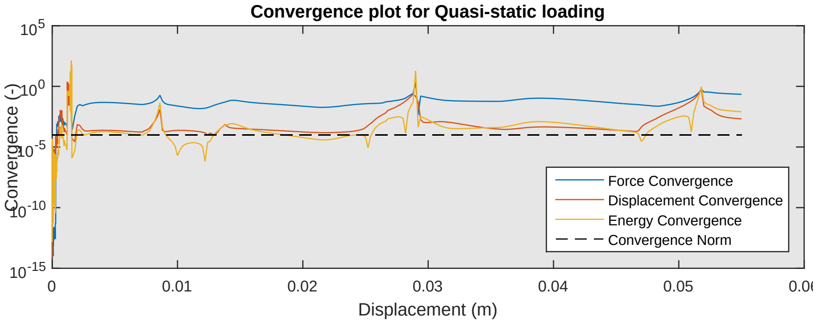

Figure 6.9: Convergence criteria for last iteration of load step during static analysis of Plane Strain Model.

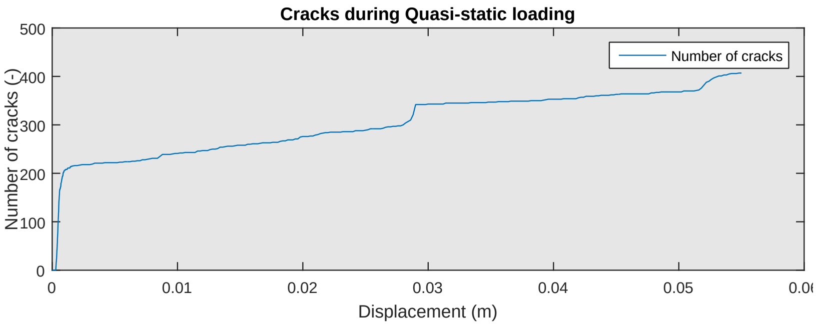

Figure 6.10: Number of cracks during static analysis of Plane Strain Model.

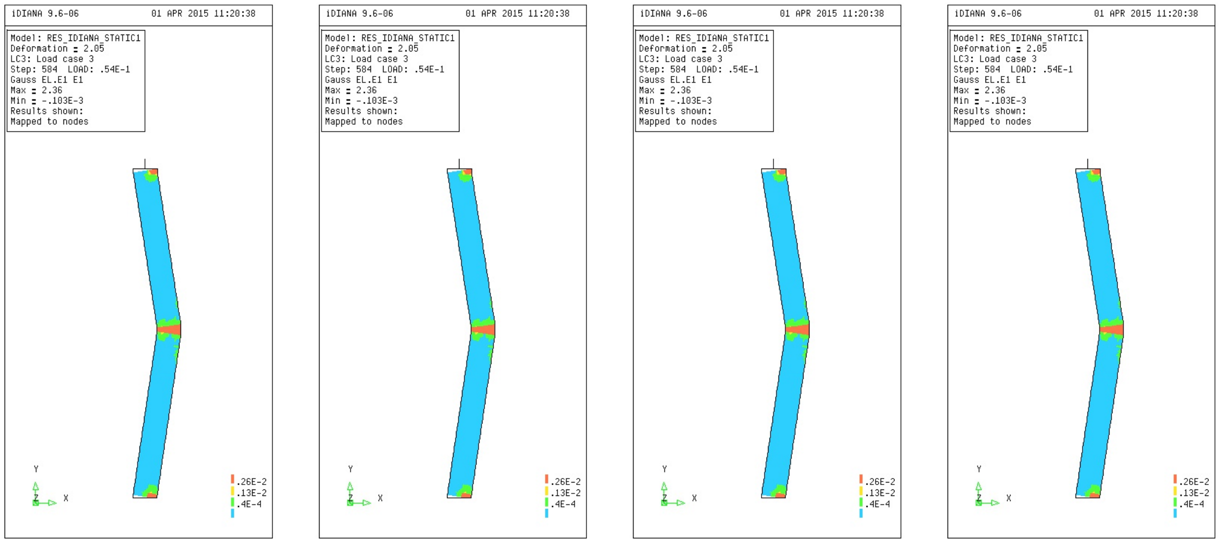

Figure 6.11: (a) & (b) Stress plots in deformed state for pre- and post-cracking. (c) & (d) Crack planes in deformed state for different applied displacements.

6.10 Transient Analysis

Time-displacement The transient analysis is performed on the Plane Strain Model. After a sensitivity analysis was performed for the thickness of the wall (Sec. 6.11). The final time-displacement diagram is given in Fig. 6.13. Here, the mid-height displacement is plotted over time. The displacement of the model gives a reasonable approximation for the experimentally found values. Especially the main frequency is fairly good, but also the damping of the displacement is similar to the experiment. The amplitude has a bigger margin of error but is still in the same order of magnitude.

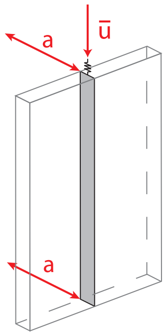

Figure 6.12: Loading direction in transient analysis of Plane Strain Model.

The most important difference between the experiment and the model is the starting point of the initial rocking. This point is independent of the interface stiffness, damping and even thickness of the wall at mid-height and bottom. This probably has to do with the fact that the wall is modelled as a continuous element with uniform stiffness. Since the mortar is less stiff and strong than the bricks rounding and grinding over the splices can cause these excitations.

Frequency In Fig. 6.14 the output from a Fast Fourier Transform is depicted. The signal is transformed to the frequency domain which gives the amplitude of the individual components of the fourier series of the signal, which corresponds to the frequencies displayed on the x-axis. The governing frequency which has the maximum amplitude is indicated for both the experimental and numerical results. The frequency of the analysis is somewhat lower, this can be observed from the longer period in Fig. 6.13. The amplitudes of the spectrum of the analysis is generally bigger since the amplitudes in of the response displacement are bigger as well.

Convergence Fig. 6.15 shows the convergence plots for the transient analysis. As indicated the norm is not always met for all three criteria. In the beginning of the analysis the absolute displacement and energy convergence norms are very small making it hard to reach convergence, so this can be ignored. Around 0.5 s this is again the case for the energy convergence criterium. During the rocking of the wall good convergence is obtained, since no cracking has to be modelled.

Deformation Fig. 6.16 shows deformation plots at different moments in time. When the wall start rocking the deformation of the compressive part of the cross-section is of importance for the behaviour. In the middle figure the crack surface is clearly bended near the compressive zone. And thus the deformation over the thickness of the cross-section is non-linear. In Chapter 7 this will be discussed since this behaviour is impossible for shell elements.

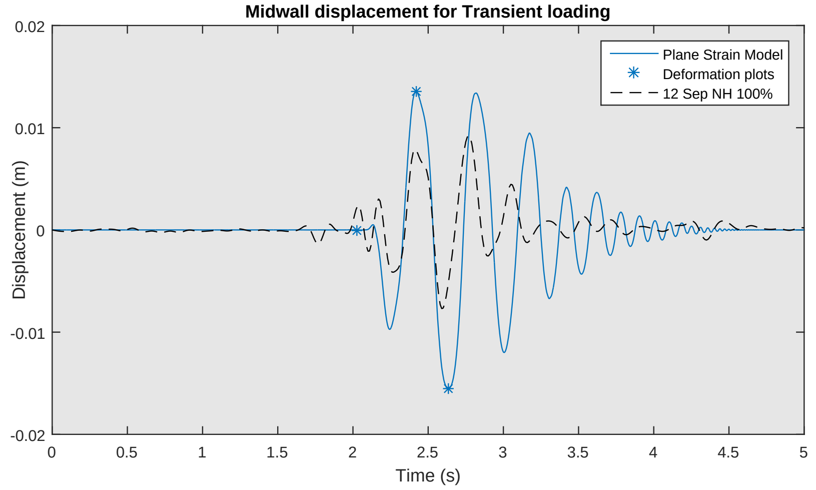

Figure 6.13: Time-displacement diagram of Plane Strain Model with NH100% Specimen 12 acceleration input.

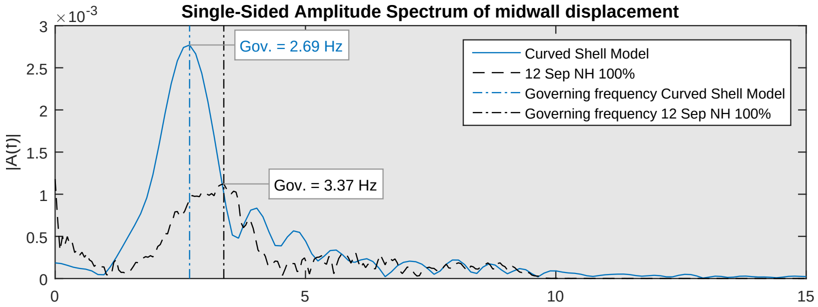

Figure 6.14: Frequency Amplitude Spectrum of Plane Strain Model with NH100% Specimen 12 acceleration input.

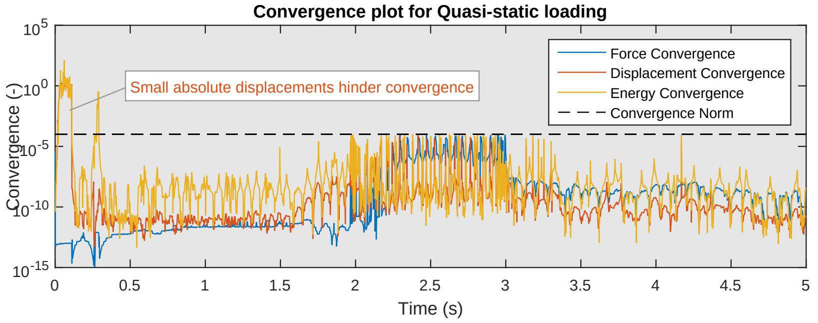

Figure 6.15: Convergence during transient analysis of Plane Strain Model with NH100% Specimen 12 acceleration input.

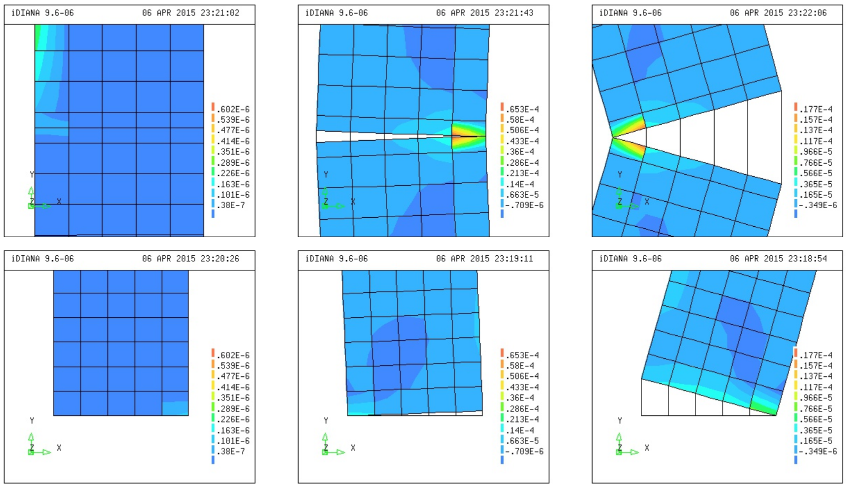

Figure 6.16: Deformation plots during transient analysis of Plane Strain Model with NH100% Specimen 12 acceleration input.

6.11 Sensitivity Study

A sensitivity study was performed to find the influence of the following parameters: the thickness of the wall at mid-height, the stiffness of the line interface elements and the Rayleigh coefficients for mass and stiffness damping.

Thickness The thickness of the wall at mid-height is reduced to simulate the degree of damage and geometric irregularities due to bad craftsmanship. When a wall is damaged mortar can drop out of the joints. This reduces the effective width on which the wall rocks while leaving the weight approximately equal. Doherty does not give an accurate description of the damage of the wall before the shake table experiment. The thickness reduction is obtained by narrowing the mid-height nodes.

From Fig. 6.17 and 6.18 it can be concluded that the hypothesis made in the previous paragraph was correct. For smaller thicknesses the amplitude and the governing period of the response increases. A base value of 90 mm is chosen for the thickness of the wall.

Interface stiffness The interface stiffness is of importance since it influences the compressive stiffness of the top and bottom supports as well as the mid-height interface during rocking. According to general rule of thumb the stiffness should be significantly bigger than the effective stiffness of the surrounding elements (100 to 100 times as big). This causes the compressive deformation to be in the plane strain elements and the tensile deformations in the interface elements.

In Fig. 6.21 and 6.22 the interface stiffness can be found. Both the amplitude and the governing frequency seem to be converging towards the experimental results for higher stiffnesses. Therefore a stiffness of $10^{-13} \frac{N}{mm^3}$ or 0.0054 mm eq. URM is chosen as a base value.

Rayleigh damping coefficients The Rayleigh damping coefficients are not determined by Doherty. Since it was not possible to find the correct eigenmodes with DIANA they are determined via this sensitivity study.

The mass damping coefficient has a great effect on the maximum amplitude as well as on the decay of the amplitude (Fig. 6.21). From Fig. 6.22 it can be concluded that the mass coefficient should be 4 s^{-1}. However, from the Fig. 6.21 it can be observed that for this mass coefficient the rate of decay of the amplitude is too big. Thereforce the smaller mass coefficient of $1s^{-1}$ is chosen.

The stiffness damping coefficient only has an effect on the decay of the amplitude. Since this in not visualised in Fig. 6.24 the base value is chosen from Fig. 6.23 to be $1.4 \times 10^{-5}s$.

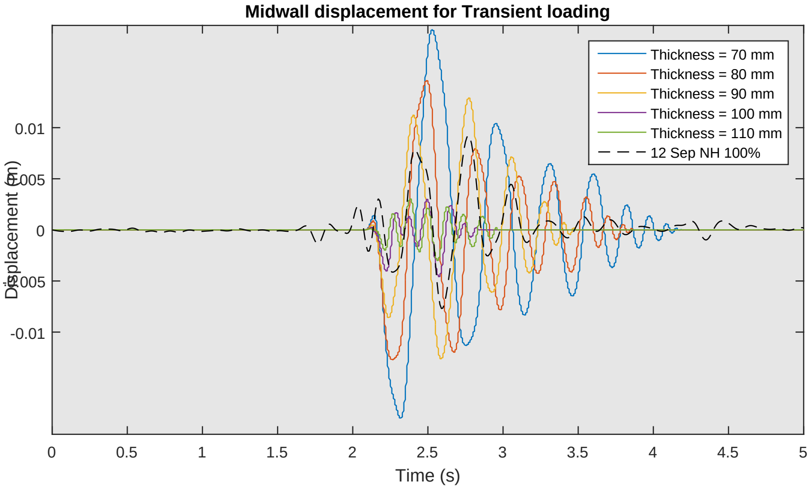

Figure 6.17: Time-displacement diagram for different mid-height and bottom thickness of Plane Strain Model.

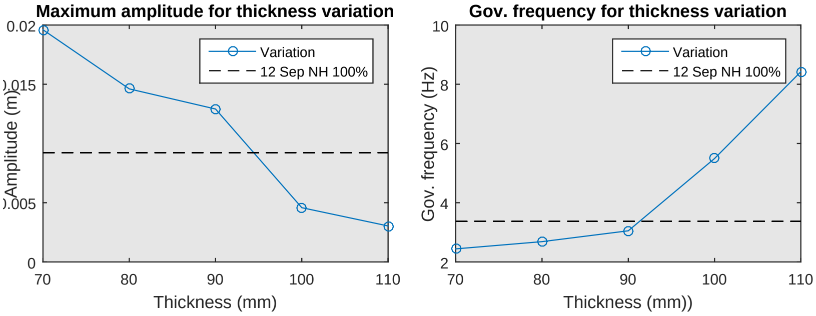

Figure 6.18: Maximum amplitude and mean frequency for different mid-height and bottom thickness of Plane Strain Model.

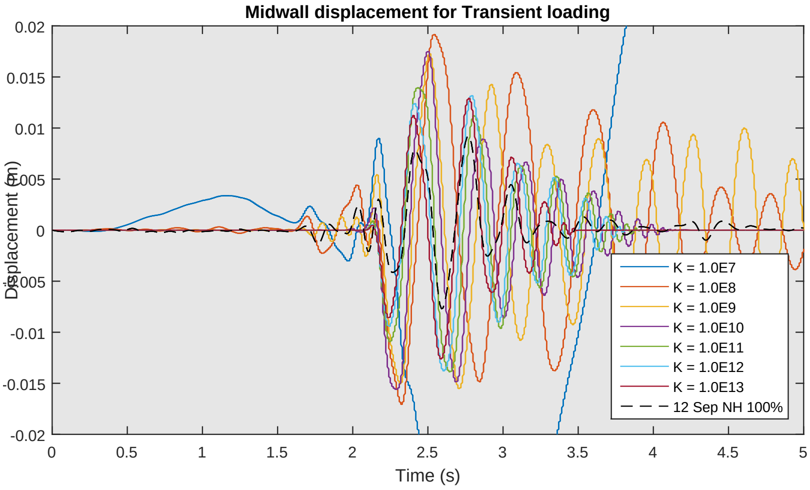

Figure 6.19: Time-displacement diagram for different interface stiffness of Plane Strain Model.

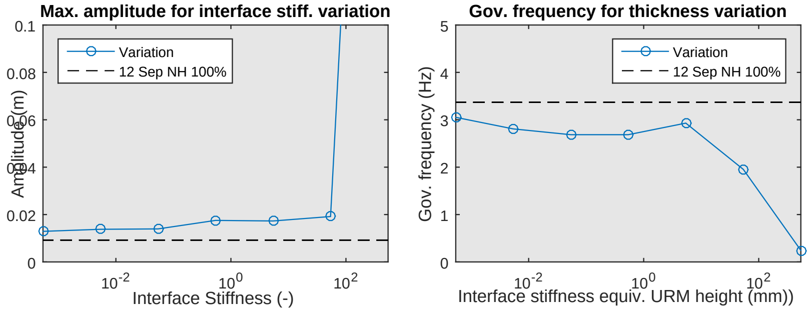

Figure 6.20: Maximum amplitude and mean frequency different interface stiffness of Plane Strain Model.

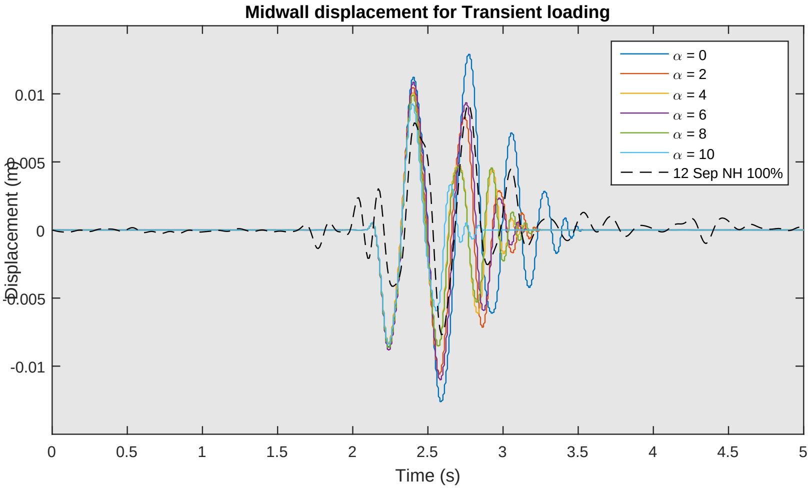

Figure 6.21: Time-displacement diagram for different Rayleigh coefficients for mass damping of Plane Strain Model.

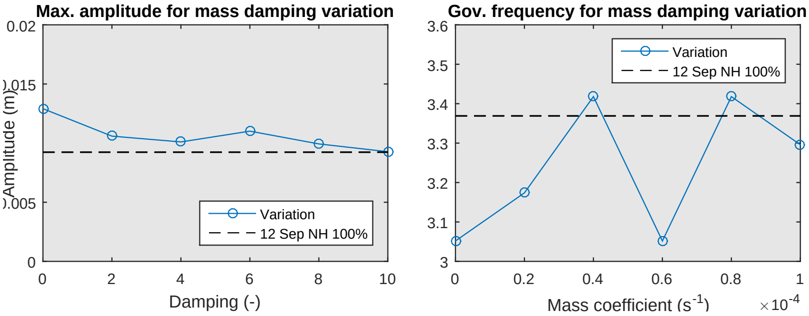

Figure 6.22: Maximum amplitude and mean frequency for different Rayleigh coefficients for mass damping of Plane Strain Model.

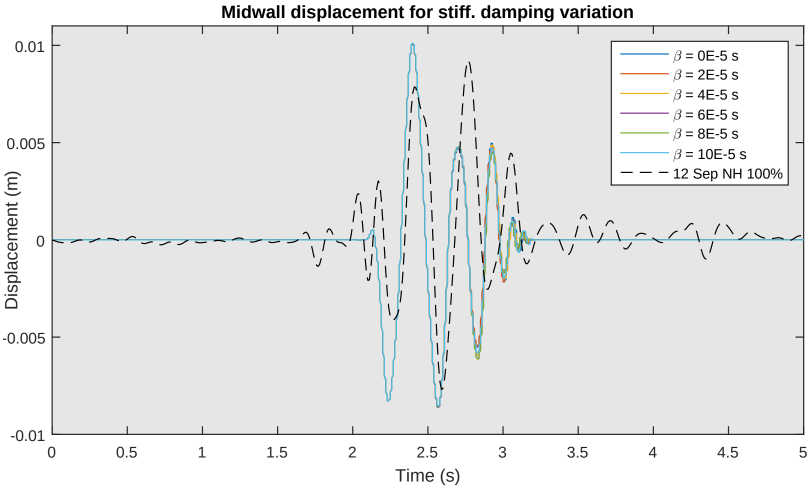

Figure 6.23: Time-displacement diagram for different Rayleigh coefficients for stiffness damping of Plane Strain Model.

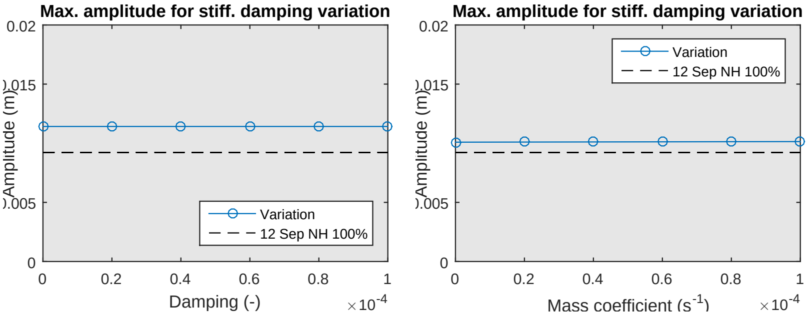

Figure 6.24: Maximum amplitude and mean frequency for different Rayleigh coefficients for stiffness damping of Plane Strain Model.

6.12 Conclusion

The Plane Strain Model mimics the behaviour of an infinite wall. It is used in this study as an alternative to 3D modelling.

The model is able to approximate the static resistance according to the results of ARUP, both with discrete cracking as well as with smeared cracking. Although it was not possible to find full convergence, the results are comparable with the results from the Curved Shell Model. The post-peak resistance is underestimated when compared with the results from the experiment.

Results from transient analysis are very good for the Nahanni 100% accelerations. The main influence on the amplitude and frequency of the response are the thickness of the wall at mid-height/bottom support and the damping. These parameters are unknown since damage was inaccurately reported by Doherty and the damping was not measured.

From transient deformation plots it was observed that the wall does not deform linearly over the thickness during transient analysis. This can have an influence on the response of the shell elements used in the final model.

6.A Phased Analysis

Due to the order of experiments followed by Doherty as explained in Sec. 1.5 the transient tests are all from cracked and damaged specimen. This causes an uncertainty in the validation of the material model, since the damage can not be modelled a priori. A phased analysis is proposed where the wall is first cracked with an imposed displacement using a static analysis and then excited using a transient analysis.

Cyclic loading Since the wall must be cracked over the whole cross-section a cyclic loading is applied. In Fig. 6.25 a total cycle is displayed. The area between the loading and unloading curve is the dissipated energy. The peak in the second loading direction is smaller than the first peak. This is due to the damage already done in the first half cycle. Less energy is needed to crack the last bit of the wall and thus the resistance is lower.

Transient excitation After cracking the wall is excited by a base acceleration. The accelerations signal Nahanni 100% specimen 12 is used. Divergence occurs at loadstep 6. This is caused by the cracked cross-section which is not able to transfer any loads after being cracked.

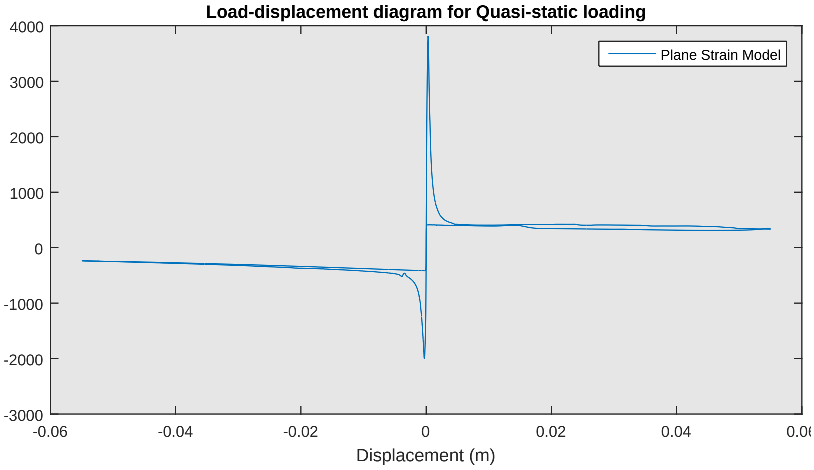

Figure 6.25: Load-displacement diagram for static part of phased analysis.

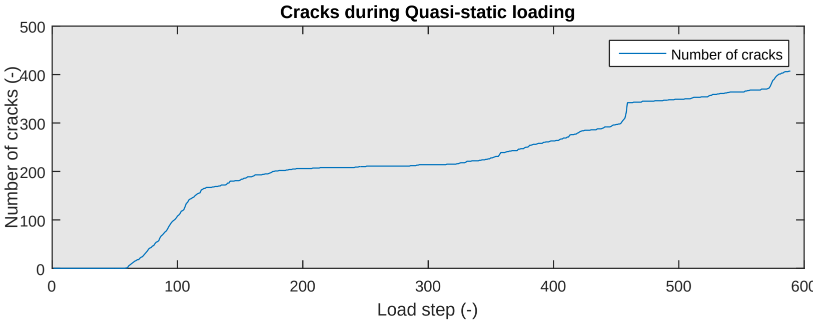

Figure 6.26: Crack development during cyclic static part of phased analysis.

6.B Integration Points over Thickness

In shell elements implemented in DIANA it is possible to use a certain number of integration points over the thickness direction of the element. The maximum number of integration points is eleven. To see if this amount is sufficient The Plane Strain Model with elements in the thickness direction of the wall is used. In this model the number of elements over the thickness is scaled from 1 to 5 with 2 or 3 integration points per element. Material properties, geometry and loads are as explained before. Since the development of the crack over the thickness is important for the maximum load resistance the number of integration points is of importance.

From analyses with increasing number of integration points it can be concluded that 10 integration points is sufficient for initial and post-peak behaviour. To find a good approximation of the peak resistance 8 is already sufficient, see Fig. 6.27

To check if this conclusion also holds for the Curved Shell Model, the analysis was redone with increasing numbers of integration points. From this test it can be concluded that eight integration points over the thickness is sufficient to model the cracking of the wall correctly, see Fig. 6.28

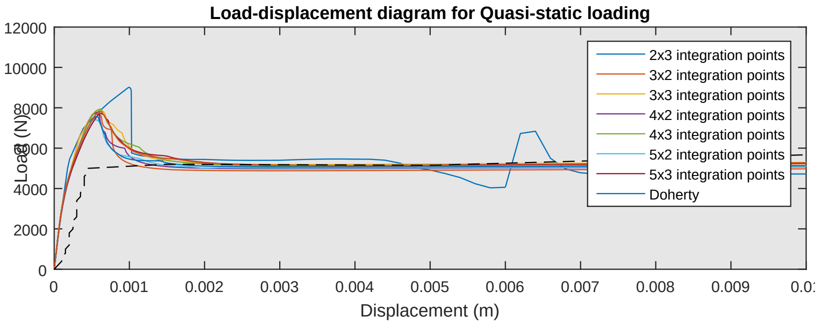

Figure 6.27: Load-displacement diagram for Plane Strain Model with increasing number of integration points over the thickness.

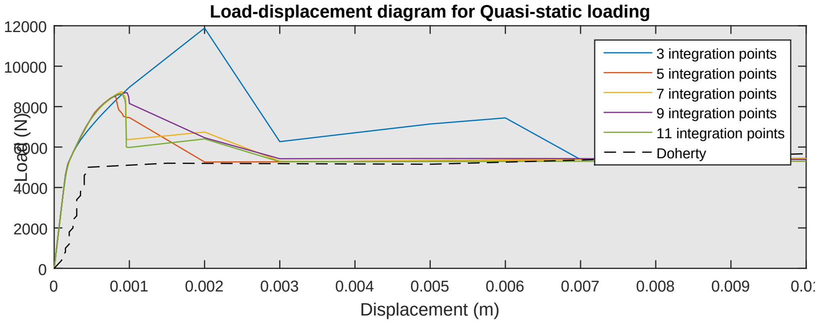

Figure 6.28: Load-displacement diagram for Curved Shell Model with increasing number of integration points over the thickness.

6.C Variation of number of elements over thickness

During transient loading the deformation over the cross-section is non-linear. Since reduction of the interface stiffness for the Curved Shell Model effectively decreased the minimum crack size to be lower than the full width, see Sec. 7.11 the idea is that increasing the number of elements over the thickness will have the same effect for the Plane Strain Model. This should then allow the development of smaller cracks to open and thus show earlier excitations.

Transient analyses was performed with elements over the thickness varying from 5 to 10. The results are displayed in Fig. 6.29. It can be seen that the initial significant excitation is equal for all variations and thus the hypothesis is wrong.

It should also be noted that the decay of the response increases with increasing numbers of elements over the thickness. In Fig. 6.12 the final transient response after optimization is shown. This response seem to have a too long echoing response. Increasing the number of elements over the thickness could thus be beneficial.

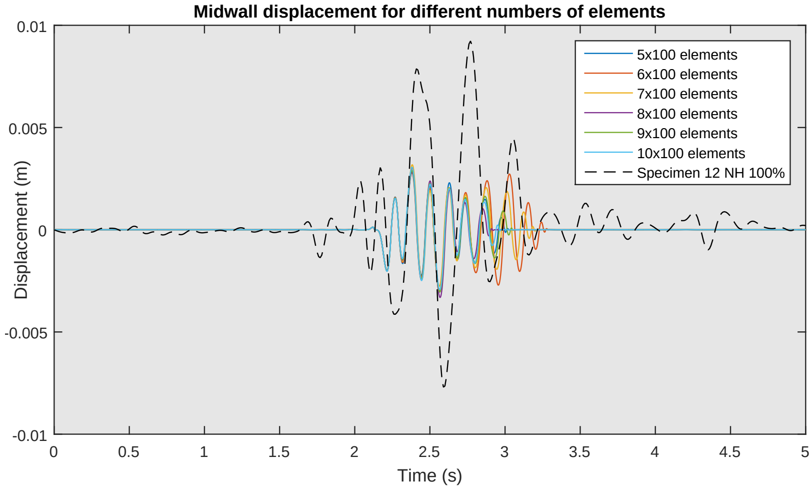

Figure 6.29: Variation of number of elements over the thickness.

7

Curved Shell Model

A very efficient way to model a wall is with curved shell elements; elements in which the third dimension is compressed into one plain. Still it is possible to account for stress differences over the thickness by applying multiple integration points over the thickness. In this way it should be possible to model both in-plane and out-of-plane failure modes realistically.

In this chapter shell elements are used to validate the experiment of Doherty. Since during the experiment of Doherty the wall is already cracked before it was tested on a shake table the model is first cracked with a static analysis as applied by Doherty. Also a fully split model is used where the crack is already modelled with an interface element.

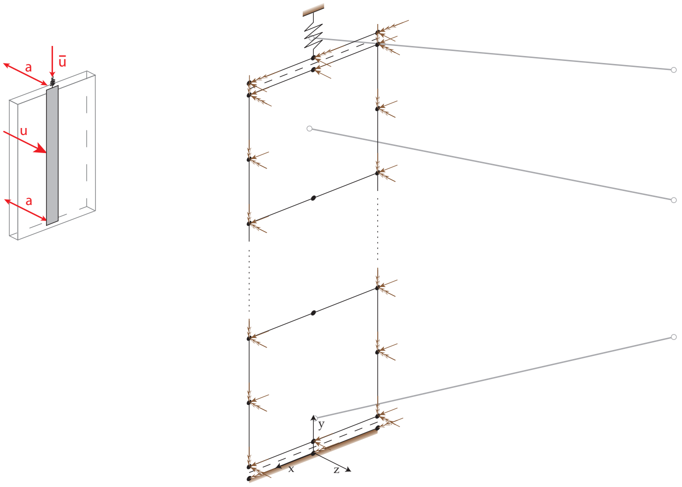

Translational spring (SP2TR)
Linear elasticity

Curved shell quadrilateral (CQ48S)
Total strain rotating crack
11 integration points z-dir

Line interface (L16IF)
No-tension
11 integration points z-dir

Figure 7.1: Schematized representation of the Curved Shell Model.

7.1 Discretization

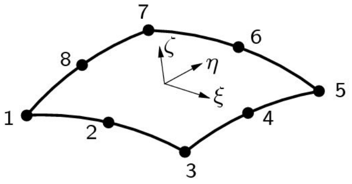

Figure 7.2: Curved shell element (CQ48S) (TNO DIANA BV, 2014)

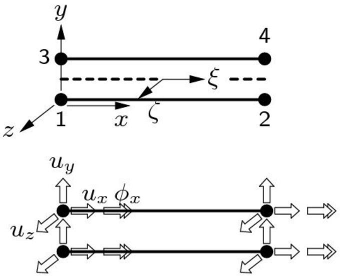

Figure 7.3: Line interface element (L16IF)(TNO DIANA BV, 2014)

Curved shell elements For the Two-Dimensional Curved Shell Model, schematised in Fig. 7.1, CQ48S elements have been used, see Fig. 7.2. It is an eight noded quadrilateral and has six degrees of freedom per node. This element was chosen after analyses with elements with less degrees of freedom diverged. The reason for the divergence was the occurance of spurious modes, see Section 7.A. These modes are suppressed by constraining the extra degrees of freedom.

Line interfaces For the bottom support, the top support and the cracked midsection, a line interface element is used, the element L16IF, see Fig. 7.3. Since this line interface has also a rotational degree of freedom and can have integration points over the thickness similar rocking behaviour a within the shell element is possible. The difference is that the interface element the deformation is not a smeared crack but a difference in displacement between the top and the bottom nodes. This approach was chosen after a comparison with a model with dummy elements representing the cracked cross-section. In Section 5.A it is shown that both approaches are equivalent, but the second is more complex.

Top spring At the top of the wall a spring is attached to apply an overburden force as is done in the experiment.

Rocking behaviour Important for the geometric non-linear behaviour is the ability of the wall to rock, as is described in Chapter 4. Since the thickness of the shell elements is applied as an parameter the geometric non-linear effect must be enforced by the integration points over the thickness of the element. The out-of-plane rotation of the shell elements changes the effective stress over the thickness of the shell element and thus in the integration points were the stress-strain relationship is evaluated. Due to the low tensile and the high compressive strength the integration points at the outer side of the wall will first fail. This results in a smeared crack of the element in that layer. Since in the compressive side of the wall only small elastic deformations are present the rotation point will shift towards the compressive side. Rocking behaviour should thus be possible.

7.2 *Geometry*

The typical dimensions of the elements are presented in Table 7.1.

Dimension			Shell Element (CQ40S)	Dummy Element (CL9BE)	Top Spring (SP2TR)	Line Interface (L16IF)
Thickness	t	$[m]$	0.11	-	-	0.11
Width / Length	b/l	$[m]$	0.1	0.1	0.1	0.05
Height	h	$[m]$	0.1	-	-	-
Area	A	$[m^2]$	-	1.0	-	-

Table 7.1: Typical dimensions of the elements in Curved Shell Model.

Integration Points For realistic cracking to occur a minimum number of integration points over the thickness is needed. In Section 6.B the minimum number of integration points over the thickness is determined to be eight.

Direction	Shell Element (CQ40S)	Dummy Element (CL9BE)	Top Spring (SP2TR)	Line Interface (L16IF)
η	2	2	1	1
ξ	2	1	1	2
ζ	11	1	1	11

Table 7.2: Integration points per elements in Curved Shell Model.

7.3 *Boundary conditions*

The elements are constraint as indicated in Fig. 7.1 and Table 7.3. At the bottom and top the nodes of the line interface that are not connected with a shell element are supported in translational directions (at the top y-direction is free) as well as rotations around the x-axis. This allows for a relative rotation difference to develop over the line interface.

To restrain spurious modes the sides of the elements are constraint as a line of symmetry, it therefore mimics an endless wall. This is done by restraining the rotation around the y- and z-axis and translation in x-direction.

Set	Node nr.	u_x	u_y	u_z	ϕ_x	ϕ_y	ϕ_z
Top node spring	436	✓	✓	✓	-	-	-
Top interface; top nodes	436	-	-	✓	✓	-	-
Top interface; bottom nodes	436	-	-	✓	✓	-	-
Bottom interface; top nodes	436	-	-	-	-	-	-
Bottom interface; bottom nodes	436	✓	✓	✓	✓	-	-
Shell elements; left nodes	436	-	-	-	-	✓	✓
Shell elements; right nodes	436	✓	-	-	-	✓	✓

Table 7.3: Boundary conditions of the Curved Shell Model.

7.4 *Material Properties*

Two material models are applied; the Total Strain Rotating Crack model is applied to the shell elements and the No-tension material model is applied to the line interface elements. The general material properties per element type are presented in Table 7.4.

Element	Mass Density $\rho\ [kg/m^3]$	Youngs Modulus $E\ [N/m^2]$	Poisson's Ratio $\nu\ [-]$	Stiffness $K\ /\ D_{STIF}\ [-]$
Shell Element (CQ40S)	1800	5.4×10^9 * ◇ 11.6×10^9 ** ◇	0.0	-
Overburden spring (SP2TR)	-	-	-	$1.01 \times 10^5\ N/m$
Line interface (L16IF)	-	-	-	$1.0 \times 10^{13}\ N/m^3$ * × $1.0 \times 10^8\ N/m^3$ ** ×
Dummy Element (CL9BE)	-	-	-	$1.0 \times 10^{13}\ N/m^3$

Table 7.4: Material parameters applied in Curved Shell Model.

* For specimen 8
** For specimen 12
◇ Total Strain Rotating Crack material model applied.
× No-tension material model applied

Total Strain Crack model In this material model the crack is smeared out over the element as if it were a plastic strain. This has as an advantage that cracks can appear anywhere in the structure but and the geometry remains unchanged.

The influence of rotating or fixed cracking is crucial for the resistance of the wall in out-of-plane behaviour during cyclic loading. This is explained in Section 7.B.

Element	Tensile strength $f_t\ [N/m^2]$	Mode-I fracture energy $G_{ft}\ [J/m^2]$	Compressive strength $f_c\ [N/m^2]$	Compressive fracture energy $G_c\ [J/m^2]$	Shear retension factor $\beta\ [-]$
Curved shell element (CQ48S)	0.3×10^6 * 0.45×10^6 **	35	4.41×10^6	5000	0.01

Table 7.5: Material parameters for Total Crack Rotating Strain material model for curved shell elements (CQ48S).

* For specimen 8
** For specimen 12

No-tension model In the interfaces a no-tension material model is applied. This is a material model which reduces the stiffness if the relative displacement between the nodes in the interface is positive. The difference between the compressive and tensile stiffness is in the order of 10^9. This causes only the tensile displacements to be significant.

If the general rule of thumb is used to determine the stiffness of the interface element, an extreme stiff interface element is found that does not lead to realistic results. The stiffness used in this model is obtained from a sensitivity analysis described in Section 7.11.

7.5 Loads

Self-weight, overburden stress, imposed horizontal displacement and base acceleration are applied on this model in different analyses. The details of the loads applied on the model are presented in Table 7.6 for the static analysis and in Table 7.7 for the transient analysis.

Order of application	Type of load	Point of application	Amount	Load steps	Direction
1	Self-weight	-	-	1	-y
2	Displacement	Node 436	-16.36×10^{-3} m	1	y
3	Displacement	Node 116	0.5×10^{-3} m	300	x

Table 7.6: Applied loads on Curved Shell Model during static analysis.

Order of application	Type of load	Point of application	Amount	Load steps	Direction
1	Self-weight	-	-	1	-y
2	Base	Hor. supports	Load factors $\times g$	1241(0.01s)	x

Table 7.7: Applied loads on Curved Shell Model during transient analysis.

Different sets of load factors are used, the record of the Nahanni (NH) earthquake scaled from 100 to 400% (Fig. 5.4) and the El Centro (EL) earthquake scaled to 66%. In the results presented in this chapter the Nahanni 100% acceleration signal for specimen 12 was used.

7.6 *Convergence Criteria*

For the static and the transient analysis three convergence criteria have been specified. The incremental step is converged if all three criteria are simultaneously met. The iteration method continuous with the next step if the criteria are not met and the maximum number of iterations is reached. Only when the intermediate solution diverges the calculation is aborted.

Details on the convergence criteria are specified in Table 7.8 for the static analysis and Table 7.9 for the transient analysis.

Method	Convergence norm	Rel. convergence tolerance
Newton-Raphson	Displacement	$1.0 \cdot 10^{-3}$
"	Force	$1.0 \cdot 10^{-3}$
"	Energy	$1.0 \cdot 10^{-3}$

Table 7.8: Details on convergence criteria of Curved Shell Model for static analysis.

Method	Convergence norm	Rel. convergence tolerance
Newton-Raphson	Displacement	$1.0 \cdot 10^{-3}$
"	Force	$1.0 \cdot 10^{-3}$
"	Energy	$1.0 \cdot 10^{-3}$

Table 7.9: Details on convergence criteria of Curved Shell Model for transient analysis.

In the following sections the convergence of the analyses is also presented. For each step the convergence of all these criteria at the end of the iteration is given. Also the norm is presented to show if the norm is met.

7.7 *Time Integration Method*

The Backward Euler integration scheme is used for time integration. This method is explained in the literature review. The stability of the solution during time integration is dependent on the step size and the method used.

Stability During the development of this model divergence occured due to spurious modes, see Section 7.A. After decreasing the step size no divergence was observed any more.

Method	Step size	Remark
Backward Euler	2.0×10^{-3} s	-

Table 7.10: Details on time integration method for Curved Shell Model.

7.8 Modal Analysis

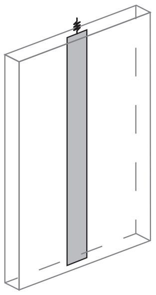

Figure 7.4: Modal analysis of Curved Shell Model.

A modal analysis was performed to find the eigenfrequencies of the model as well as the Rayleigh Damping coefficients for transient analysis. For this analysis the cracked model with the line interface element at mid-height was used since during transient analysis this will be cracked as well.

The eigenfrequencies are presented in Table 7.11 and the eigenmodes are displayed in Fig. 7.5. Eigenmode 1 is the governing mode during transient analysis, rocking of the bodies in out-of-plane direction. Eigenmode 2 is bending of the wall itself in the second natural frequency. The second and the third are eigenmodes where the interface element and the topspring are deformed, these are neglected for calculation of the Rayleigh coefficients since they do not play a big role in the out-of-plane deformation of the wall.

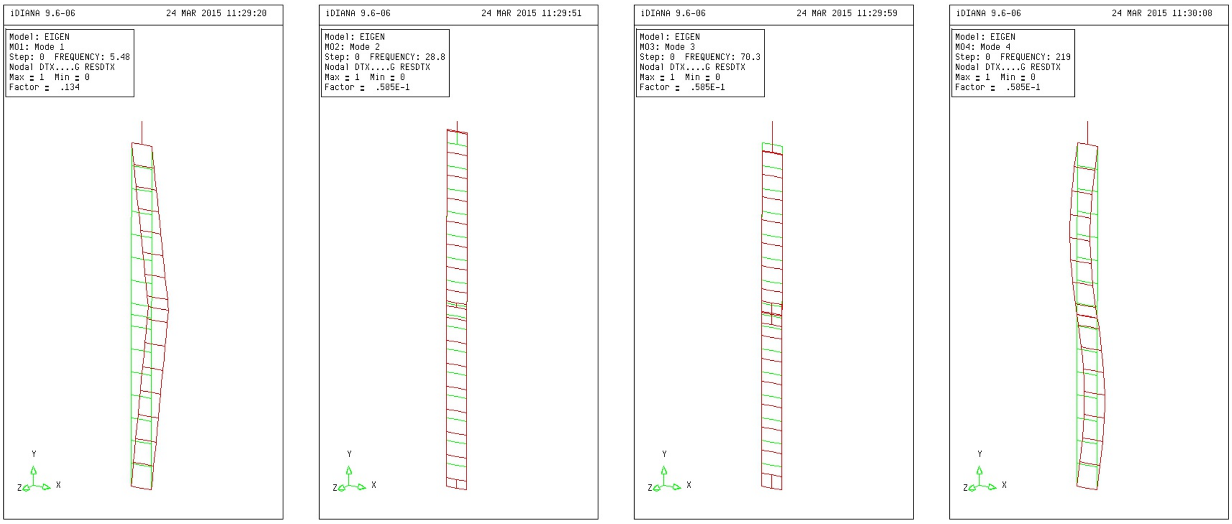

```
iDIANA 9.6-06                    24 MAR 2015 11:29:20
Model: EIGEN
M01: Mode 1
Step: 0  FREQUENCY: 5.48
Nodal DTX....G RESDTX
Max = 1  Min = 0
Factor =  .134
```

```
iDIANA 9.6-06                    24 MAR 2015 11:29:51
Model: EIGEN
M02: Mode 2
Step: 0  FREQUENCY: 28.8
Nodal DTX....G RESDTX
Max = 1  Min = 0
Factor =  .585E-1
```

```
iDIANA 9.6-06                    24 MAR 2015 11:29:59
Model: EIGEN
M03: Mode 3
Step: 0  FREQUENCY: 70.3
Nodal DTX....G RESDTX
Max = 1  Min = 0
Factor =  .585E-1
```

```
iDIANA 9.6-06                    24 MAR 2015 11:30:08
Model: EIGEN
M04: Mode 4
Step: 0  FREQUENCY: 219
Nodal DTX....G RESDTX
Max = 1  Min = 0
Factor =  .585E-1
```

Figure 7.5: First four eigenmodes of the Curved Shell Model with a line interface element at mid-height.

Eigenmode		1	2	3	4
Eigenfrequency	$[Hz]$	5.48	28.76	70.31	218.96

Table 7.11: Details on convergence criteria of Curved Shell Model.

Damping The Rayleigh damping coefficients are displayed in Table 7.12.

Damping ratio	Mass coefficient	Spring coefficient
$[-]$	$[1/s]$	$[s]$
0.05	3.357	0.709×10^{-4}

Table 7.12: Rayleigh Damping coefficients applied on Curved Shell Model

7.9 *Static Analysis*

A static analysis is performed to find the load-displacement behaviour before and after cracking. For this purpose there is no line interface element at mid-height and thus the physical properties of the wall are enforced by the shell elements. In the Thesis Report also a Curved Shell Model with a line interface at mid-height and discrete cracking is considered. Here only the results are presented in Fig. 7.7.

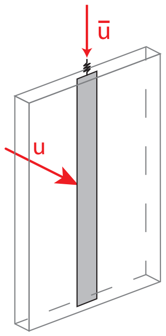

Figure 7.6: Loading direction in static analysis of Curved Shell Model.

Load-displacement Since the material is very brittle a sudden drop in the load-displacement diagram, Fig. 7.7 is visible after the maximum load is reached. This is the point where the wall cracks. Dependent on the normal force applied and the fracture energy the resistance can increase after the initial cracking (explained in Section 2.A). In this case the resistance decreases and a snap-back curve is expected. With a displacement controlled procedure it is not possible to fully follow this snap-back curve. Instead the displacement is increased, for a few steps no convergence is found, but then the curve is found again and the analysis can continue. In Section 7.C an estimate is made for this snap-back curve.

The post-peak behaviour is underestimated in comparison with Doherty's experimental results. Compared with the Plane Strain Model this model gives similar results. This enforces the idea that the increase in resistance found by Doherty is an effect of non-linear behaviour of the overburden spring or a bigger Youngs Modulus.

Convergence From Fig. 7.8 it can be concluded that only just after the peak resistance the convergence norm for all criteria is not met. After the peak the energy and displacement convergence criteria are met and the solution can again be thought of as reliable. After 0.07 m displacement there is some load steps in which convergence is not met, however the model does not diverge as well. Since no irregularities are found in the load-displacement diagram it is assumed that this is no problem and the error remains small.

Cracks In Fig. 7.9 the development of the number of cracks is given. As can be seen most cracks develop during the initial cracking of the wall. From Fig. 7.10.a & d it can be concluded that most cracks are found in the tensile zone at mid-height, the crack continues over the thickness of the beam at mid-height between load steps 100 and 200 and in the tensile zone at top and bottom also cracks form. For this axial load no crushing occurs.

Stress From the stress plots of the outer surface of the wall the tensile zones at mid-height can be observed. The maximum stress of the elements are presented. It can be observed that the in mid-height region the tensile strength is reached and the cracks develop.

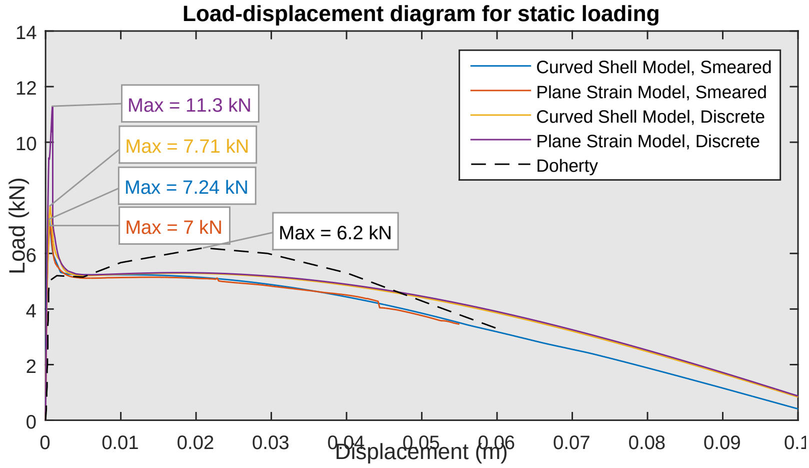

Figure 7.7: Load Displacement diagram for Curved Shell Model.

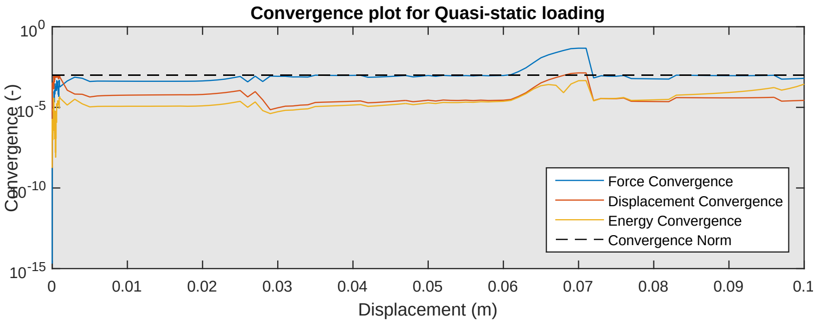

Figure 7.8: Convergence criteria for last iteration of load step during static analysis of Curved Shell Model.

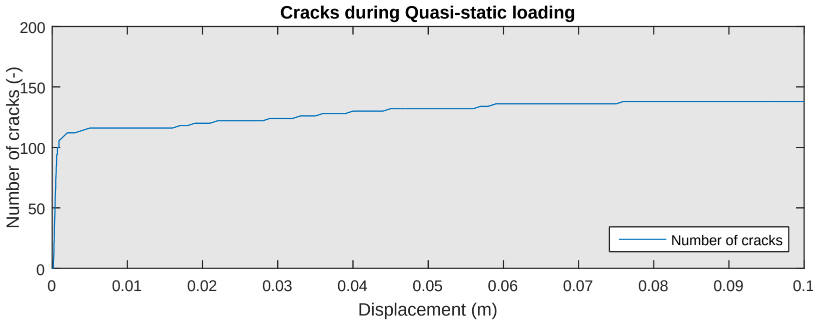

Figure 7.9: Number of cracks during static analysis of Curved Shell Model.

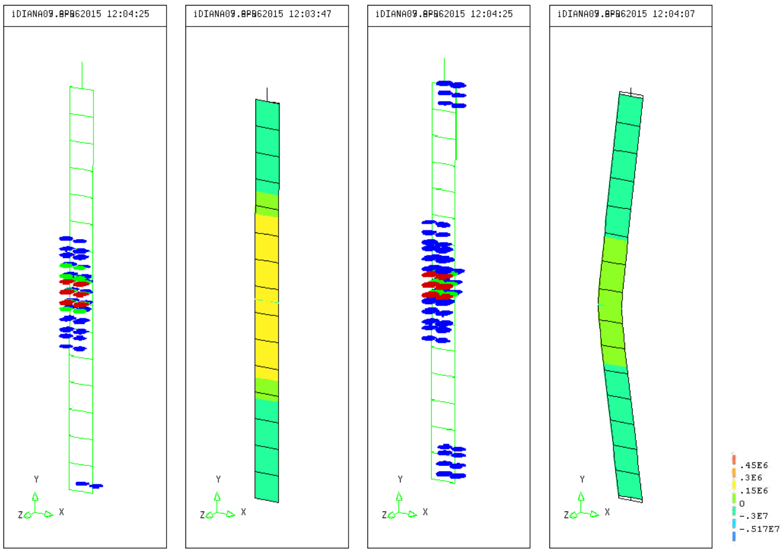

Figure 7.10: (a,b) Cracks in wall and stress at outer surface of wall at loadstep 100 (c,d) Cracks in wall and stress at outer surface of wall at loadstep 200.

7.10 Transient Analysis

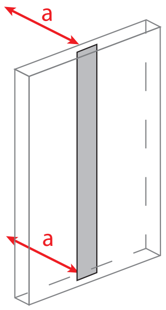

Figure 7.11: Loading direction in transient analysis of Curved Shell Model.

Time-displacement The response of the Curved Shell Model has been fitted to the experimental results by changing the interface stiffness, damping and mid-height thickness (Fig. 7.12). The initial excitation, amplitude, frequency (Fig. 7.13) and damping are very accurate with the experimental results. As discussed in Sec. 7.4 a reduced stiffness is used for the line interface elements. This is a consequence of the shell elements that can only deform linearly over the thickness.

Frequency In Fig. 7.13 the amplitude spectrum of the response is shown. The governing frequency is the frequency with the biggest amplitude and corresponds to the main rocking frequency. As can be observed the spectra line up very accurately and the governing frequency is approximately similar.

Convergence The model has no problem to converge with the Backward Euler time integration method and sufficiently small time steps. During the rocking behaviour more iterations are required to obtain convergence.

Deformations In Fig. 7.15 the resultant traction and deformation vectors of the line interface elements are plotted. It can be seen that in the start of the analysis the deformation is still linear and fully in compression, but at bigger excitations the compressive area is smaller and the deformation is non-linear.

Sensitivity The model is very sensitive for changes in the interface stiffness, damping and thickness of the wall. A sensitivity study has been performed into these parameters and is presented in Section 7.11. The main conclusion from this study is that the interface elements do not allow non-linear deformation over the thickness of the elements and therefore the stiffness should be reduced.

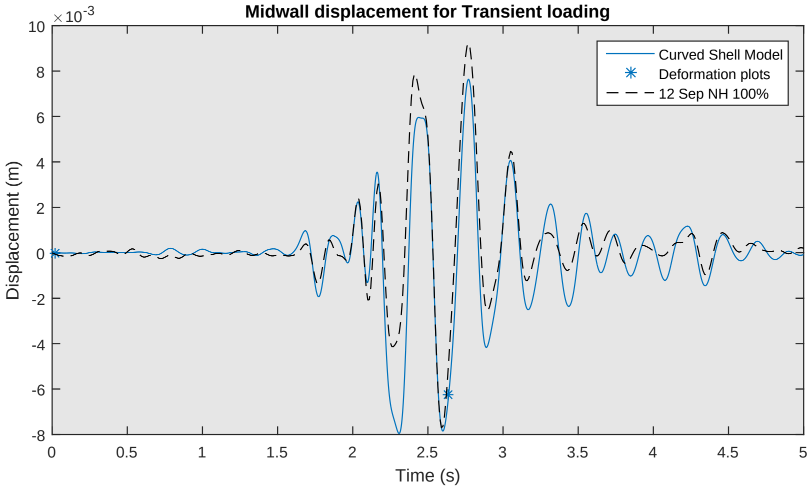

Figure 7.12: Time-displacement diagram of the Curved Shell Model.

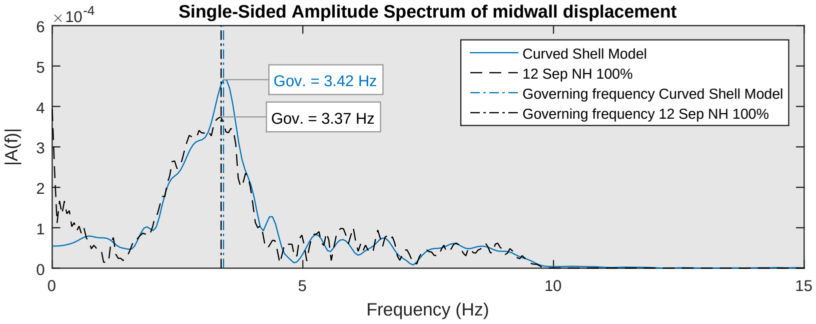

Figure 7.13: Frequency Amplitude Spectrum of Curved Shell Model with NH100% Specimen 12 acceleration input.

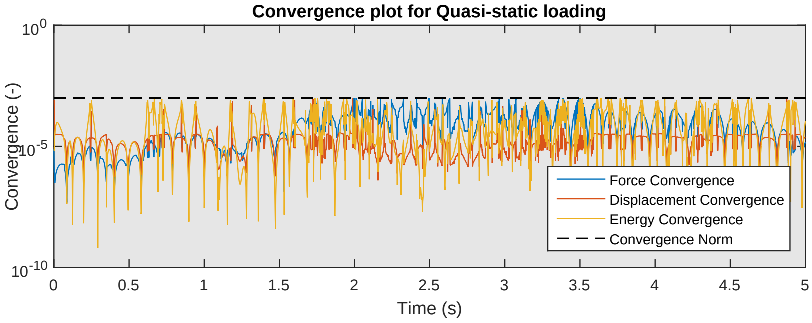

Figure 7.14: Convergence criteria for last iteration of load step during transient analysis of Curved Shell Model.

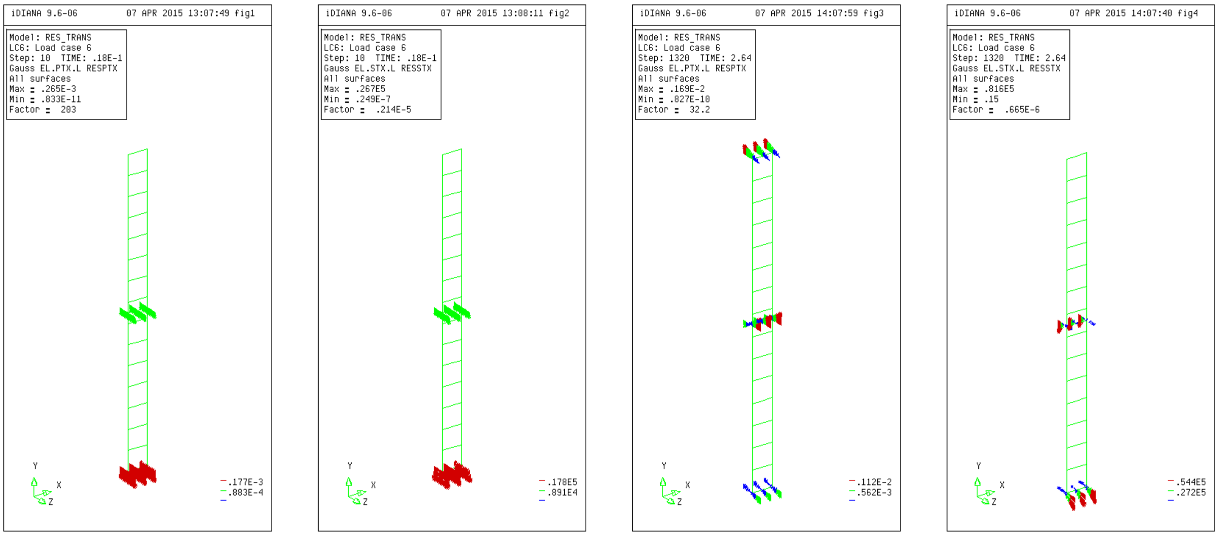

Figure 7.15: (a-b) Traction and deformation plots in deformed state for small excitation. (c-d) Traction and deformation plots in deformed state for big excitation.

7.11 Sensitivity Analysis

During testing of this model a sensitivity analysis was carried out. The model is very sensitive to dummy stiffness, thickness of the wall and damping. When modelling a URM wall these parameters are not always known a priori and it is good too obtain some kind of sense for the sensitivity of these properties. The reason for the variation of these properties is thoroughly discussed in Sec. 6.11.

Thickness Fig. 7.16 shows some the time-displacement diagram of the mid-height wall response for varying thickness. This figure shows that the response decays faster for thicker walls. Fig. 7.17 gives the maximum amplitude and the governing frequency as a function of the thickness. From this graph it could be concluded that the governing frequency is best approximated with a wall of 100 mm thick. However, the wall decays too fast too reach the second oscillation. Therefore a wall thickness of 90 mm is chosen.

Interface Stiffness From Fig. 7.18 is can be seen that low interface stiffness results in big excitations and high stiffness in low excitations. In Fig. 7.19 the stiffness is expressed as an equivalent height of URM column. The left figure confirms the statement made from Fig. 7.18, the right figure shows that for higher interface stiffness the frequency also increases.

As explained in Sec. 6.11 the stiffness should be significantly bigger than the effective stiffness of the surrounding elements. However for the Curved Shell Model with interfaces this does not seem to be the case. When a high dummy stiffness is used the point of rotation shift totally to the outer fibre and only the last integration point is loaded in compression. For lower stiffnesses more integration points are loaded in compression. This mimics the real behaviour of a masonry wall where there is also a compressive toe area over which the compressive force is spread. The interface stiffness should thus be adjusted to this phenomenon.

Rayleigh damping coefficients The mass damping coefficient has a great effect on the maximum amplitude as well as on the decay of the amplitude (Fig. 7.20). From Fig. 7.21 it can be concluded that the mass coefficient should be 4 s^{-1}. However, from the Fig. 7.20 it can be observed that for this mass coefficient the rate of decay of the amplitude is too big. Thereforce the smaller mass coefficient of $1s^{-1}$ is chosen as base value.

The stiffness damping coefficient only has an effect on the decay of the amplitude. Since this in not visualised in Fig. 7.23 the base value is chosen from Fig. 7.22 to be $6 \times 10^{-3}s$.

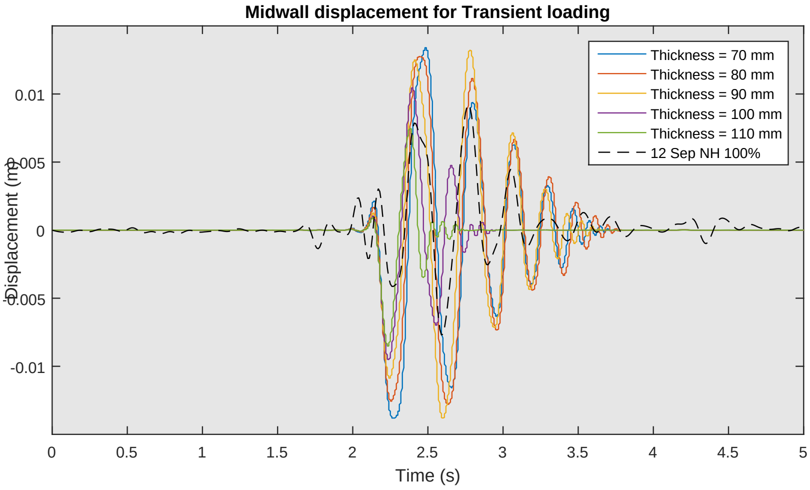

Figure 7.16: Time-displacement diagram for different mid-height and bottom thickness of Curved Shell Model.

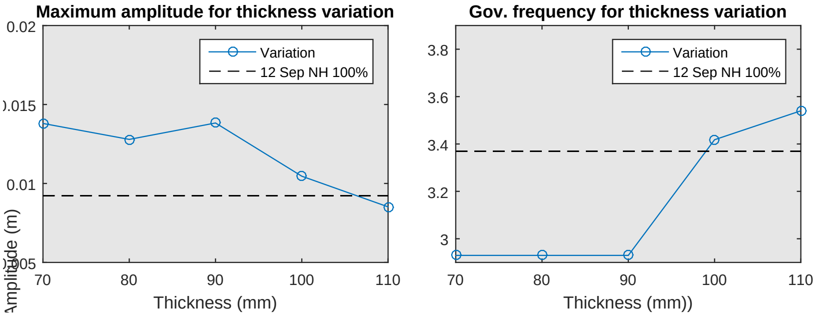

Figure 7.17: Maximum amplitude and mean frequency for different mid-height and bottom thickness of Curved Shell Model.

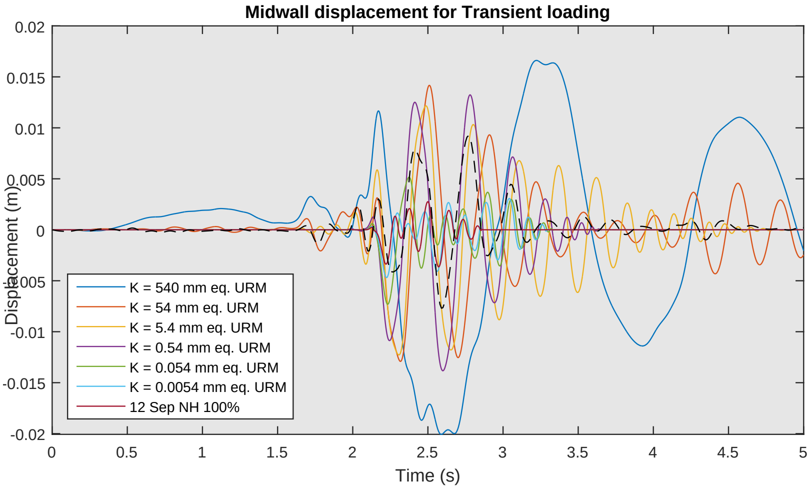

Figure 7.18: Time-displacement diagram for different interface stiffness of Curved Shell Model.

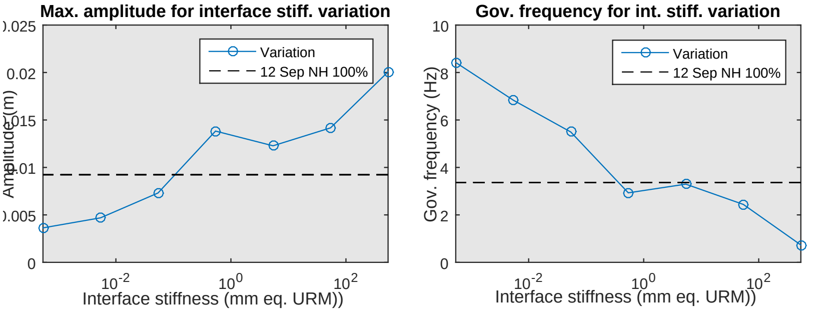

Figure 7.19: Maximum amplitude and mean frequency different interface stiffness of Curved Shell Model.

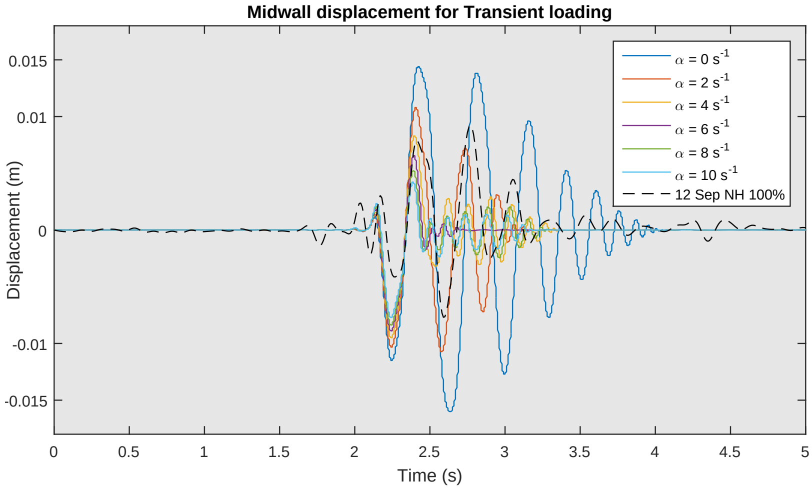

Figure 7.20: Time-displacement diagram for different Rayleigh coefficients for mass damping of Curved Shell Model.

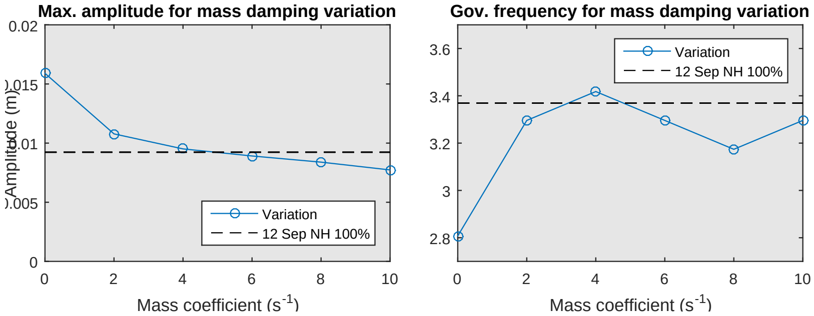

Figure 7.21: Maximum amplitude and mean frequency for different Rayleigh coefficients for mass damping of Curved Shell Model.

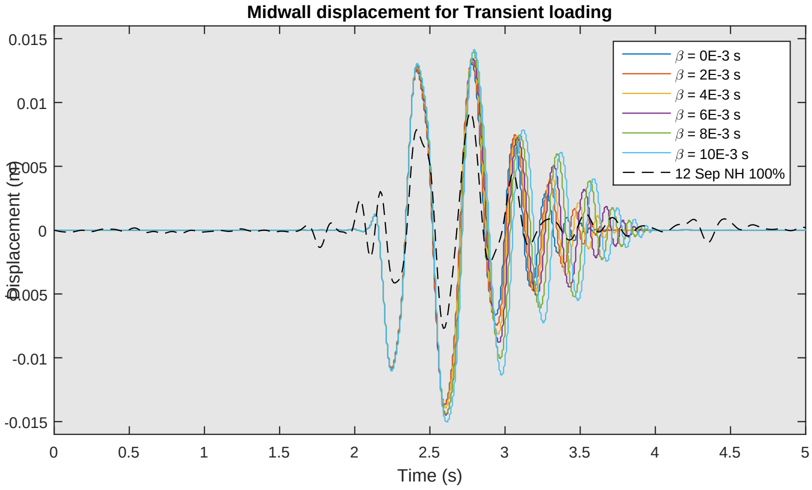

Figure 7.22: Time-displacement diagram for different Rayleigh coefficients for stiffness damping of Curved Shell Model.

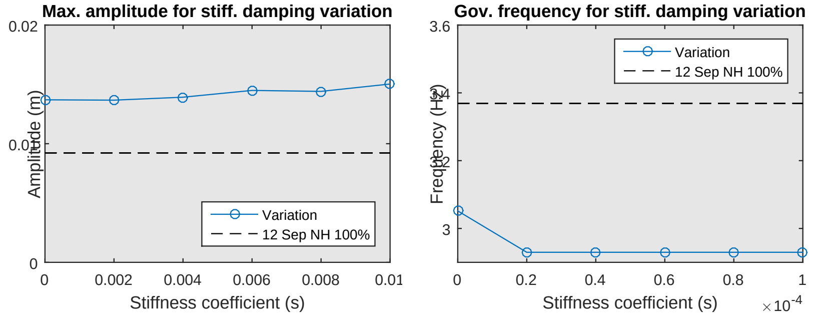

Figure 7.23: Maximum amplitude and mean frequency for different Rayleigh coefficients for stiffness damping of Curved Shell Model.

7.12 Conclusion

The Curved Shell Model is numerically the most efficient since is has a discretization with the least amount of nodes. However, from static an dynamic validation it was not found to accurate in all situations.

The Curved Shell Model is not able to approximate the dynamic behaviour with a smeared cracking approach. After cracking of the wall it diverges, no rocking behaviour is found. This is probably due to a reduction of the shear resistance after cracking.

When a line interface is applied at mid-height of the wall a very good approximation is possible for both static as well as dynamic analysis if the line interface stiffness is reduced. The reduced stiffness is needed to account for the inability of the shell and line interface elements to model non-linear deformations over the thickness of the elements. This is due to Euler-Bernoulli's hypothesis plane sections remain plane.

With the help of a sensitivity study it was possible to find good values for the interface stiffness and obtain a good approximation of the response of the wall.

7.A Spurious Modes

During development of the Curved Shell Model for transient excitations divergence occured at random moments in time. When the deformed shapes were observed some strange deformations were found. A few deformation plots are shown in Fig. 7.24. Different types of divergence occur, from left to right; the bottom interface is lost in shear out-of-plane, one of the shell elements expands in vertical direction, the thinner element at mid-height folds double, the whole wall buckles in in-plane direction.

These spurious modes are an effect of numerical instability during time integration. When the time step is too large it is possible that no solution is found and the problem diverges. This can be solved by either changing the time integration method to a method which adds some numerical damping like Wilson time integration or reduce the incremental time step. The second option is used for the transient analysis described in Section 7.10, the time step is reduced to 2.0^{-3} s.

Too reduce the possibility of spurious modes, the unrealistic deformations are restraint as much as possible. The wall is a segment of an infinite long wall, which is loaded over the whole length in out-of-plane direction. The deformation should thus be equal over the length and rotations around the y-axis and z-axis are impossible. Therefore these degrees of freedom are constraint, see Sec. 7.3.

Together these measures result in a stable time integration.

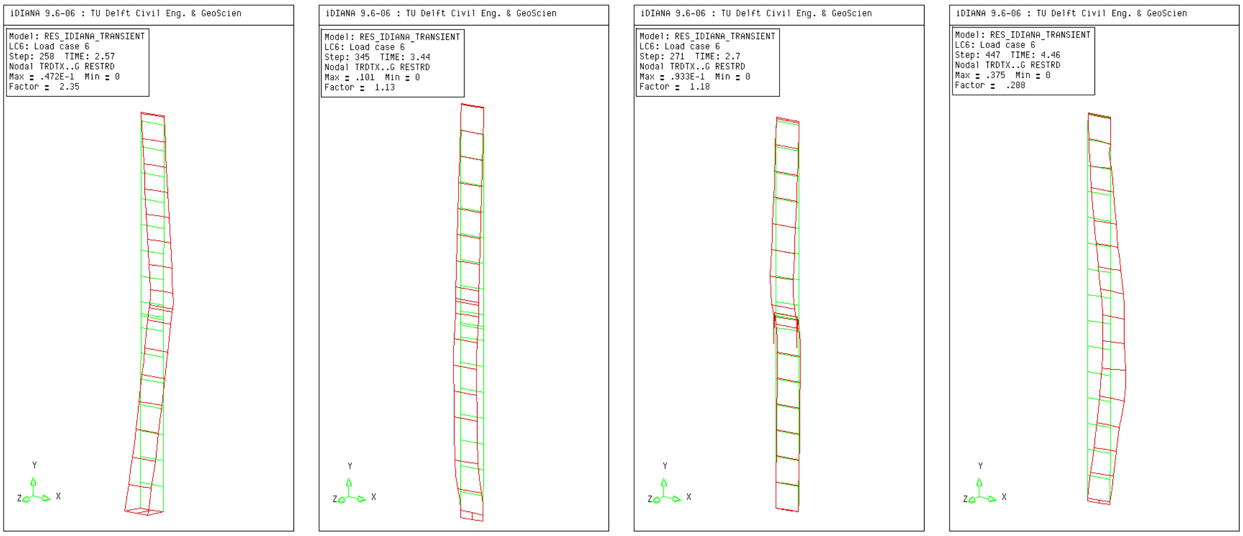

Figure 7.24: Divergence due to spurious modes.

7.B Fixed and Rotating Smeared Cracking

In the total strain cracking concept two approaches are possible, one where the strain orientation is fixed upon cracking and one where the strain automatically orientates in the direction of the principle strain.

Both methods are available in DIANA and are implemented in a similar manner. The material parameters are evaluated by updating the stress tensor with a stress increment which is dependent on the strain increment. This increment is evaluated along certain axes. For the rotating approach these axes are the principle directions of the strain tensor, for the fixed approach the principle directions of the strain tensor upon cracking. To find the strain increment in this direction the strain increment in the global coordinates is transformed using a transformation matrix which is found using the Jacobi method, which calculates the eigenvectors of the strain tensor.

The fixed total strain concept fixes the transformation matrix from the cracking moment on. This is a logical approach for tensile cracks since the material splits and thus the crack can no longer change it's orientation. However, in compression the orientation of the crushing plane can change during increased loading. Also, when cyclic loading is applied, the orientation of a crushing plane does not necessarily need to have the same orientation as a tensile crack which was formed earlier on the same spot. These effects are missed by the fixed total strain cracking concept.

This effect of the different orientation of crushing and cracking is clearly visible for an out-of-plane wall which is cyclic loaded. Shell elements are used to model the wall, with the fixed total strain crack concept. Over the thickness direction 11 integration points are used. The wall is loaded with an overburden load and a prescribed displacement at mid-height of the wall.

First tensile cracks appear in the integration points of outer layer of the elements. These cracks have a horizontal orientation, which is fixed for the rest of the analysis. When the deformation continues crushing occurs at the inner layer (Fig. 7.26.a). These crushing planes are orientated diagonally and are from that moment on also fixed for the rest of the analysis. When the wall is unloaded and then reloaded in the other direction no horizontal tensile cracks can develop since the diagonal crushing planes are fixed (Fig. 7.26.b). This results in a stiff behaviour visible in the load-displacement diagram. When the rotating total strain crack concept is used the orientation of the crushing planes is not fixed and the wall has similar load-displacement behaviour in both directions.

For a wall loaded purely out-of-plane the direction of the tensile cracks and crushing planes should in principle be horizontal. Due to the discretization of the finite elements the direction of the principal compressive stresses is orientated in a diagonal direction, although in a continuing wall these should also be horizontal. When other situations are examined, for instance a building with walls loaded in-plane as well as out-of-plane, the orientation of the cracks in cyclic loading will also change for tension and compression. A possible alternative could be a mixed concept where the crack orientation is only fixed when a tensile crack has developed and is released when the crack is closed. If the same crack is reloaded the original orientation of the crack is recovered.

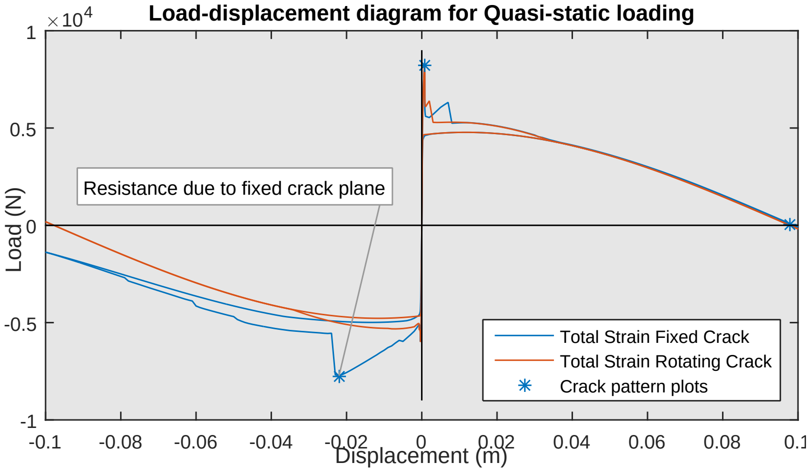

Figure 7.25: Load-displacement diagram for Curved Shell Model with Total Strain Fixed Crack material model.

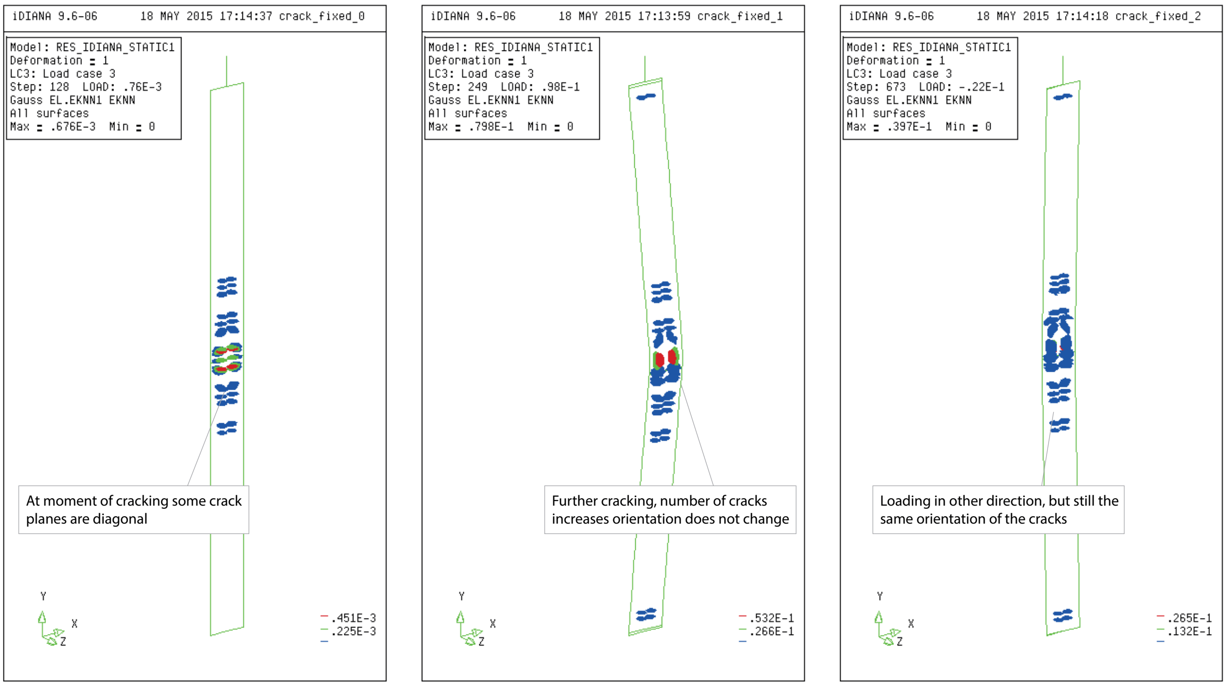

```
iDIANA 9.6-06       18 MAY 2015 17:14:37 crack_fixed_0
Model: RES_IDIANA_STATIC1
Deformation = 1
LC3: Load case 3
Step: 128  LOAD: .76E-3
Gauss EL.EKNN1 EKNN
All surfaces
Max = .676E-3  Min = 0
```

At moment of cracking some crack planes are diagonal

```
iDIANA 9.6-06       18 MAY 2015 17:13:59 crack_fixed_1
Model: RES_IDIANA_STATIC1
Deformation = 1
LC3: Load case 3
Step: 249  LOAD: .98E-1
Gauss EL.EKNN1 EKNN
All surfaces
Max = .798E-1  Min = 0
```

Further cracking, number of cracks increases orientation does not change

```
iDIANA 9.6-06       18 MAY 2015 17:14:18 crack_fixed_2
Model: RES_IDIANA_STATIC1
Deformation = 1
LC3: Load case 3
Step: 673  LOAD: -.22E-1
Gauss EL.EKNN1 EKNN
All surfaces
Max = .397E-1  Min = 0
```

Loading in other direction, but still the same orientation of the cracks

Figure 7.26: Cracks for Fixed Total Strain Cracking at load steps 128, 249 and 673

7.C Snap-Back Estimation

The load-displacement diagram of the static analysis has a steep decline after the initial peak, see Fig. 7.8. Due to the cracking nature of the material a snap-back could be in the load-displacement diagram. At a snap-back the equilibrium path first decays for both the force and displacement before the displacement increases again.

As explained in the literature review, the area underneath the load-displacement diagram equals the work performed. With this relation it is possible to make an estimate of the 'real' load-displacement curve since the energy required to crack the cross-section is equal to the fracture energy times the cross-section area.

To give an estimate for the snap back behaviour two models are compared. One with shell elements over the full height of the wall to which the Total Strain Rotating Crack material model is applied and one with an interface element half way to which the no-tension material model is applied as being an already cracked cross-section. The difference in the load-displacement diagram will thus only be the cracking of the cross-section. In Fig. 7.27 both diagrams are shown. The difference must thus be the work done during cracking. The difference during greater displacements is caused by the stiff line interface behaviour and is not taken into account.

The difference between the curves is approximated using the trapezoid rule for numerical integration,

$$W = \Sigma(f(u) - g(u)) \cdot \Delta u = 3.7096\ Nm$$

The work performed during cracking should be equal to,

$$W = G_f \cdot l \cdot t = 3.6575\ Nm$$

Since the work performed during cracking is bigger than the theoretical work done during cracking there is a sign of a snap-back. However, this snap-back is only very small. The important variation of the interface stiffness does effect the peak load, which effects the approximation of the performed work. Still it is proven that there is some kind of snap-back.

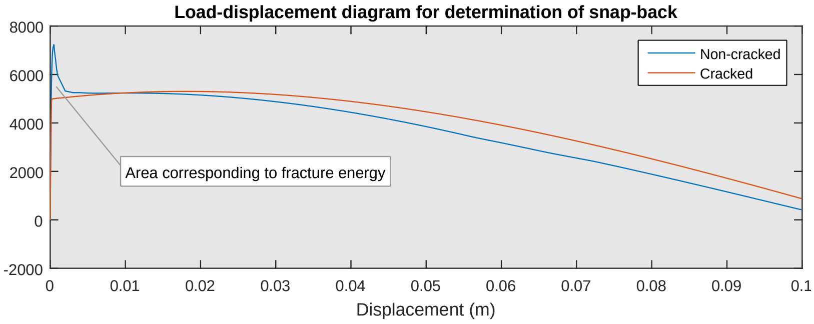

Figure 7.27: Load Displacement diagram for cracked and non-cracked Curved Shell Model.

7.D Element Choice Boundary Conditions

In the 2D model with curved shell elements over the length of the wall, the geometric non-linear effect of the thickness, the rocking of the wall, should be incorporated. At mid-height this is not a problem since the stresses are distributed over the thickness of the wall. The rotation point then automatically shifts towards the extreme fibres.

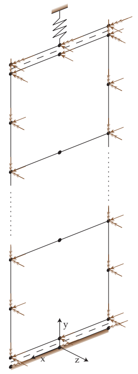

Figure 7.28: Modelling rocking behaviour with line interface elements.

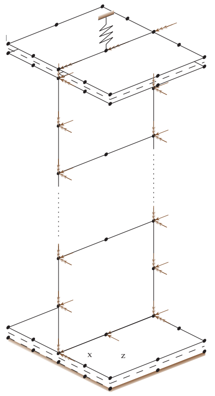

Figure 7.29: Modelling rocking behaviour with plane interface elements and dummy members.

The boundary conditions are however more tricky. The connection should be represented in a realistic manner. With a brick standing loose on the floor or a floor being laid upon a wall without a rotational constraint a clamped boundary constraint would not represent the rocking behaviour observed in experiments. Two different modelling methods are explored: using a line interface element with a rotational degree of freedom around its axis and using dummy interface elements to model the cross-section itself.

Line interface The first method a phenomenological approach is chosen. The interface is constraint at the bottom in all three translational and in the rotational degree of freedom around its axis. The interface element has 11 integration points over its thickness, like the shell elements have. When the wall is displaced in the middle the bottom and top constraints are rotated. Since the bottom line is constraint in this direction of rotation the rotation has to be generated from strain differences over the thickness of the interface element in the normal direction. Since a no-tension material model is applied the strain in the tensile fibres will increase much more rapid than in the compressive fibres. This causes the point of rotation to shift towards the extreme compressive fibre. The visible result will be that the line interface will open at nodes of the interface. The rocking behaviour is thus accurately modelled.

Plane interface In the second method a more realistic modelling approach. Here the interface is modelled with dummy elements representing the area of the brick which is opened by the cracks. This first side of the crack is connected to the second side, which is also made of dummy elements and is constrained with the help of a plane interface element. This plane has a no-tension material model which makes the connection act as a rocking wall. Since in this way of modelling the rocking is made visible by dummy members it is more intuitive. It is however less robust since the dummy members have a high stiffness which could make the numerical model unstable.

Excluding the possibility of overconstraining described in the Section 5.A as Feenstra's Peak, both models give similar results. The results are presented in Fig. 7.30. When comparing this to the model where both top and bottom supports were clamped (20150226b), it can be easily seen that the peak resistance of the clamped wall is higher than that of the rocking supported walls. This justifies the idealisation of the rocking support for wall connections that are not rotationally constraint. Modelling this as clamped could over predict the capacity of the wall and thus lead to unsafe situations.

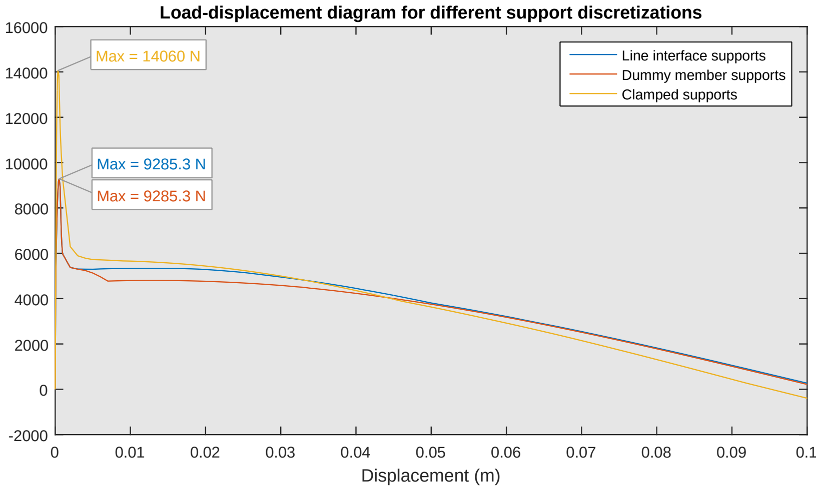

Figure 7.30: Load-displacement diagram of Curved Shell Element for different methods to apply the boundary conditions.

Bibliography

Doherty, K. T. (2000). *An investigation of the weak links in the seismic load path of unreinforced masonary buildings*. Phd, University of Adelaide A.

TNO DIANA BV (2014). *DIANA-9.6 User's Manual - Element Library*.

van Dam, J. (2015). *Validation of efficient numerical models for out-of-plane bending of unreinforced masonry walls*. Msc thesis, Delft University of Technology.